University of Alberta

CARDIAC VIDEO ANALYSIS USING HODGE HELMHOLTZ FIELD DECOMPOSITION

By

Qinghong Guo

A thesis submitted to the faculty of graduate studies and research in partial fulfillment of the requirement of the degree of **Master of Science**.

Department of Electrical and Computer Engineering

Edmonton, Canada

Spring, 2004

Library and Archives Canada

Published Heritage Branch

395 Wellington Street
Ottawa ON K1A 0N4
Canada

Bibliothèque et Archives Canada

Direction du Patrimoine de l'édition

395, rue Wellington
Ottawa ON K1A 0N4
Canada

Your file Votre référence
ISBN: 0-612-96478-7
Our file Notre référence
ISBN: 0-612-96478-7

The author has granted a non-exclusive license allowing the Library and Archives Canada to reproduce, loan, distribute or sell copies of this thesis in microform, paper or electronic formats.

L'auteur a accordé une licence non exclusive permettant à la Bibliothèque et Archives Canada de reproduire, prêter, distribuer ou vendre des copies de cette thèse sous la forme de microfiche/film, de reproduction sur papier ou sur format électronique.

The author retains ownership of the copyright in this thesis. Neither the thesis nor substantial extracts from it may be printed or otherwise reproduced without the author's permission.

L'auteur conserve la propriété du droit d'auteur qui protège cette thèse. Ni la thèse ni des extraits substantiels de celle-ci ne doivent être imprimés ou aturement reproduits sans son autorisation.

In compliance with the Canadian Privacy Act some supporting forms may have been removed from this thesis.

Conformément à la loi canadienne sur la protection de la vie privée, quelques formulaires secondaires ont été enlevés de cette thèse.

While these forms may be included in the document page count, their removal does not represent any loss of content from the thesis.

Bien que ces formulaires aient inclus dans la pagination, il n'y aura aucun contenu manquant.

Canada

Abstract

Ventricular fibrillation (VF) is an extremely rapid, highly irregular heart arrhythmia originating in the ventricles. When the VF occurs, the heart loses its capability of pumping blood, and the patients die within minutes unless the VF is immediately stopped. The mechanisms of the VF are still not completely understood. Several hypotheses suggest that it is important to extract the pure expanding component and the pure rotational component from the cardiac electrical patterns.

In this thesis, we first implement the 2-D discrete Hodge-Helmholtz field decomposition (DHHFD) based on regular triangular grids such that it can be directly used for video analysis. We then analyze the optical flow of the cardiac electrical patterns using the 2-D DHHFD. The pure expanding and the pure rotational motion components of the cardiac electrical signals are extracted. Analyses of the decomposed motion components have shown that the VF might be caused by the strong rotational components of the dynamical cardiac electrical patterns. Techniques have also been developed to detect the dominant critical points such as sources, sinks, and rotational centers in the cardiac electrical patterns. The critical points provide important clues for describing and understanding the abnormal propagation of the cardiac electrical signals. The proposed framework also provides a general tool for analysis of the fluid dynamics.

Acknowledgements

This thesis is accomplished with guidance and help from multitude of individuals. Here, I would like to express my sincere appreciation for all of them.

First of all, I would like to thank my supervisor, Dr. Mrinal K. Mandal, for his invaluable guidance and constant encouragement. He chose such an interesting topic for me. Without him, my graduate studies would not have been so enjoyable and intellectually rewarding. I would also like to thank him for his infinite patience and trust. It is not easy to tolerate such an eccentric student.

I would like to express my gratitude from the bottom of my heart to Dr. Micheal Y. Li. He derived most of the theory in this thesis on the whiteboard in his office, and explained to me the details of the Finite Element Method and fundamentals of vector calculus. He also suggested verifying the proposed algorithm using synthetic vector fields. His passion, kindness, and acute insights deeply inspired me. I do not know how to truly convey my appreciation for him.

Hearty thanks are given to Dr. Gang Liu and Mr. Jason Iden. They explained to me the fundamentals of cardiology, did several clinical experiments to validate my results, and continually encouraged me on my progress.

I would also like to thank the members of my thesis defence committee, Dr. Katherine M. Kavanagh, Dr. Zoltan Koles, and Dr. Horacio Marquez, for their thorough scrutiny of my work. Special thanks are due to Dr. Kavanagh for her invaluable advice and help on my research.

Dr. Konrad Polthier, an excellent German mathematician, answered several of my questions through email. He provided me with the original algorithm of the DHHFD, and explained to me some important concepts in his work. Here, let me express my appreciation for this excellent scientist.

At last, I would like to present my sincere gratitude to my lovely wife, Jin. Although she was very busy with her studies, she was burdened with most of the housework. Without her love and support, I would not have been able to concentrate on my research.

Table of contents

Chapter 1 Introduction 1

1.1 Existing therapies of ventricular fibrillation 1

1.2 The cardiac optical mapping method 2

1.3 Problem definition and the research contributions 4

1.4 Organization of the thesis 6

Chapter 2 Review of Background Work 7

2.1 Fundamentals of cardiac electro-physiology 7

2.1.1 The cardiac transmembrane action potential 7

2.1.2 The pathway of the electrical impulses in a healthy heart 9

2.1.3 The abnormal excitation in a fibrillated heart 10

2.1.4 The ECG and the multi-electrode mapping 11

2.2 Mechanisms of ventricular fibrillation 12

2.2.1 The multiple random wavelet hypothesis 12

2.2.2 The spiral breakup hypothesis 13

2.2.3 The single high-frequency source hypothesis 14

2.3 The critical points in the cardiac electrical patterns 15

2.4 Algorithms for image smoothing 16

2.5 Motion estimation algorithms 20

2.5.1 The OFCE-based algorithm 20

2.5.2 The block matching algorithm 23

2.5.3 The spatio-temporal auto-regression motion model 24

2.5.4 The phase correlation based algorihtm 24

2.6 Motion field decomposition 25

2.5.1 Local translational decomposition and singular value decomposition 25

2.5.2 The discrete Hodge-Helmholtz field decomposition 26

2.7 Detection of critical points from an image sequence 27
2.8 Summary 31
Chapter 3 Efficient Hodge-Helmholtz Decomposition of Motion Fields 32
3.1 The Proposed 2-D DHHFD-RTG 33
3.1.1 Setup of RTG and notations 33
3.1.2 Computing the curl-free component 37
3.1.3 Computing the divergence-free component 38
3.1.4 Computing the harmonic remainder 41
3.2 Properties of the 2-D DHHFD 41
3.3 Details of the proposed algorithm 47
3.3.1 Automatic generation of RTG 47
3.3.2 Calculation of $\nabla\phi_i$ 50
3.3.3 Construction of the element matrices S_1 and S_2 51
3.3.4 Construction of the vectors B and C 53
3.3.5 Computation of E, ∇E, W, and $(\nabla W)^{\perp}$ 56
3.4 Computational complexity of 2-D DHHFD 58
3.4.1 Computational Complexity of the 2-D DHHFD-RTG 58
3.4.2 Computational Complexity of the 2-D DHHFD-ITG 62
3.4.3 Comparison of CC of the two implementations 65
3.5 Performance evaluation 66
3.6 Summary 70
Chapter 4 Cardiac Video Analysis 71
4.1 The flowchart of the overall framework 71
4.2 Image smoothing 73
4.3 Motion estimation 75
4.4 Motion decomposition 82

4.5 Motion analysis 86

4.6 Critical point detection 88

4.6.1 Criteria for detection of critical points 90

4.6.2 Coarse detection of the critical points 92

4.6.3 Fine detection of the critical points 95

4.6.4 Performance of the fine detection 99

4.6 Summary 106

Chapter 5 Conclusions and Future Work 107

Bibligraphy 111

Appendix A Derivation from Eq. (3-10) to Eq. (3-11) 120

Appendix B Expansion of Eq. (3-14) 121

Appendix C Derivation from Eq. (3-17) to Eq. (3-18) 128

Appendix D Expansion of Eq. (3-21) 130

Appendix E Selected Matlab programs 132

List of Figures

Figure 1-1	The schematic diagram of a typical cardiac optical mapping system.	3
Figure 1-2	Two typical cardiac electrical patterns	4
Figure 2-1	Various phases of the cardiac action potential	8
Figure 2-2	The normal pathway of a healthy heart	10
Figure 2-3	Abnormal excitations in the ventricles	11
Figure 2-4	Definition of the average motion vector	21
Figure 2-5	Illustration of the 2-D DHHFD	26
Figure 2-6	The phase portraits of six fundamental fluid motions	28
Figure 2-7	Window-clipped isoclines	28
Figure 2-8	Index of a Jordan curve	29
Figure 3-1	Triangulation of the image domain Ω	33
Figure 3-2	Definition of the piecewise-linear basis function	35
Figure 3-3	The simplest vector field with only 3 vectors	43
Figure 3-4	The DOF of the potential function built on a triangle	45
Figure 3-5	The DOF of the potential function built on two triangles	46
Figure 3-6	The flowchart of the 2-D DHHFD-RTG	47
Figure 3-7	The relationship between nodes and holes of the regular rectangular grids	48
Figure 3-8	Two newly generated triangles and their vertices	48
Figure 3-9	The relationship between the Grid Table and the Node Table	49
Figure 3-10	The two-level structure of the basis gradient table	50
Figure 3-11	The neighborhood of the 5^{th} node in a vector field with 3×3 vectors	52
Figure 3-12	The mapping of the Average Vector Table	54

Figure 3-13	Decomposition of a vector field with 3×3 vectors based on RTG	59
Figure 3-14	Decomposition of a small vector field with 9 vectors using ITG	63
Figure 3-15	Generation of a synthetic complex field	67
Figure 3-16	Decomposition of a synthetic complex field	69
Figure 4-1	Image frames sampled from 4 cardiac videos	72
Figure 4-2	Flowchart of the overall framework	73
Figure 4-3	Smoothed image frames obtained using the anisotropic diffusion equation	74
Figure 4-4	Smoothed image frames obtained using three cascaded Gaussian lowpass filters	75
Figure 4-5	The global smoothness constraint	78
Figure 4-6	Motion fields obtained using the OFCE-based algorithm	80
Figure 4-7	Motion fields obtained using the BMA for the four image pairs shown in Fig. 4-1	81
Figure 4-8	The local motion field of a pacing signal in Video-4	82
Figure 4-9	Decomposition of the motion field shown in Fig. 4-6a	83
Figure 4-10	Decomposition of the motion field shown in Fig. 4-6b	84
Figure 4-11	Decomposition of the motion field shown in Fig. 4-6c	85
Figure 4-12	Decomposition of the motion field shown as Fig. 4-6d	86
Figure 4-13	Illustration of a source, a sink, and a rotational center	90
Figure 4-14	Illustration of the criteria for detection of the sources/sinks	91
Figure 4-15	Illustration of the criteria for detection of rotational centers	92
Figure 4-16	A central node and its eight neighboring nodes	93
Figure 4-17	Coarse detection of the critical points	94
Figure 4-18	The discrepancy between a detected source and its corresponding visual center	96
Figure 4-19	Smoothed potential surfaces using the anisotropic diffusion equation	97

Figure 4-20	Illustration of the hierarchical searching scheme	98
Figure 4-21	Three typical neighborhood configurations for bicubical interpolation	99
Figure 4-22	Detected critical points in Experiment-1	100
Figure 4-23	Detected critical points in Experiment-2	102
Figure 4-24	Detected critical points in Experiment-3	104
Figure 4-25	Detected critical points in Experiment-4	105
Figure B-1	Triangulation of a simple vector field with 3×3 vectors	121

List of Tables

Table 2-1	Eigenvalues of the matrix A and the corresponding phase portraits	30
Table 3-1	The symbols and their meanings	34
Table 3-2a	The first level of the Basis Gradient Table	51
Table 3-2b	The second level of the Basis Gradient Table	51
Table 3-3	The algorithm for constructing the element matrix S_1	53
Table 3-4	The algorithm for constructing the vector B	55
Table 3-5	The algorithm for constructing the vector C	55
Table 3-6	CC_{S_1+RTG} for decomposing a vector field with 3×3 vectors	60
Table 3-7	CC_{B+RTG} or CC_{C+RTG} for decomposing a vector field with 3×3 vectors	61
Table 3-8	CC_{S_1+RTG} for decomposing a vector field with $M\times N$ vectors	61
Table 3-9	CC_{B+RTG} or CC_{C+RTG} for decomposing a vector field with $M\times N$ vectors	62
Table 3-10	CC_{RTG} for decomposing a vector field with $M\times N$ vectors	62
Table 3-11	CC_{S_1+ITG} for decomposing a vector field with $M\times N$ vectors	63
Table 3-12	CC_{B+ITG} or CC_{C+ITM} for decomposing a vector field with $M\times N$ vectors	64
Table 3-13	CC_{ITM} for decomposing a vector field with $M\times N$ vectors	65
Table 3-14	CC'_{ITG} for decomposing a vector field with $M\times N$ vectors	65

Table 3-15	Comparison of the CC of the two implementations	65
Table 4-1	Brief description of the four videos	72
Table 4-2	The parameters of the discretized anisotropic diffusion equation	74
Table 4-3	CCC between the four image pairs shown in Fig. 4-3	77
Table 4-4	E_K^{cf}, E_K^{df}, and r_E corresponding to the four experiments	87

List of Acronyms

AF	Atrial Fibrillation
AV	Atrio-Ventricular
BMA	Block Matching Algorithm
CAP	Cardiac Action Potential
CC	Computational Complexity
CCC	Cross-Correlation Coefficient
DHHFD	Discrete Hodge-Helmholtz Field Decomposition
DHHFD-ITG	Discrete Hodge-Helmholtz Field Decomposition using Irregular Triangular Grids
DHHFD-RTG	Discrete Hodge-Helmholtz Field Decomposition using Regular Triangular Grids
DOF	Degree of Freedom
ECG	Electrocardiogram or electrocardiograph
FEM	Finite Element Method
FT	Fourier Transform
ICD	Implantable Cardiac Defibrillator
IFT	Inverse Fourier Transform
ITG	Irregular Triangular Grids
LTD	Local Translational Decomposition
NOT	Number of Terms
OFCE	Optical Flow Constraint Equation
RF	Radiofrequency
RTG	Regular Triangular Grids
SA	Sino-Atrial
STAR	Spatio-Temporal Auto-Regression
SVD	Singular Value Decomposition
TMM	Term-Mapping Matrix
VF	Ventricular Fibrillation
VT	Ventricular Tachycardia

Chapter 1

Introduction

The ventricular fibrillation (VF) is an extremely rapid, highly irregular heart arrhythmia originating in the ventricles, the bottom chambers of the heart. For a healthy human heart, the heart rate at rest is generally in the range 60 to 100 beats per minute (bpm) [1]. However, in ventricular fibrillation, the heart rate can exceed 350 bpm [1]. Such a high heart rate is extremely life-threatening. It has been reported that the VF is the main cause of sudden cardiac death in the industrialized world [2, 3]. When it occurs, the heart quivers dramatically and loses its capability of pumping blood, and the patients die within minutes due to hypoxia unless the VF is immediately stopped.

1.1 Existing therapies of ventricular fibrillation

In the past several decades, the only effective therapy for the VF has been the electrical defibrillation [4]. There are two types of electrical defibrillators: the external defibrillator and implantable defibrillator. The external defibrillator is a device that applies strong electrical shocks onto the patient's chest to restore the normal cardiac rhythm. In practice, the energy of the shock usually ranges from 200 to 400 Joules. A lower shock threshold is desired. However, a low-energy shock often fails to halt the VF [5, 6]. Another limitation of this therapy is that the external defibrillator is too big to be carried by the patient. It has been studied that at most 15% of the patients suffering from the VF can reach hospital in time [7].

The implantable cardiac defibrillator (ICD), on the other hand, is a small electronic device installed inside the patient's chest to prevent sudden cardiac death from the VF. Here, one or more leads are inserted in the heart. The device is in continuous monitoring mode. If the ICD detects a fast arrhythmia, it delivers an electrical shock (or multiple shocks with low magnitude) to the heart to terminate the abnormal rhythm and return the heart rhythm to normality. The

disadvantage of ICD is that it needs open surgery for implantation. Some patients are not comfortable with ICDs. When the battery power is depleted, the implanted ICD needs to be changed.

Recent studies have shown that the administration of certain drugs, such as Ca^{2+}-channel blockers, can also reduce the damage caused by the VF, and even terminate the VF [4, 8-10]. Unfortunately, in many cases, these drugs have severe side effects. Moreover, it is a difficult to determine an appropriate dose for a particular patient. Although this drug-based therapy is still in its infancy, it looks promising.

The mechanisms of VF are not completely understood, and hence extensive future research is needed to develop more effective and safer therapy approaches.

1.2 The cardiac optical mapping method

To understand the mechanisms of VF, the electrical activity of the heart must be critically studied. In modern cardiology research, the cardiac optical mapping method is often used to directly observe the cardiac electrical activity with high spatio-temporal resolution.

The optical mapping method uses a voltage-sensitive dye (such as di-4-ANEPPS, RH-421, RH-237, or WW781), which is injected to the studied heart, such that the electrical activity of the heart can be quickly and linearly converted into optical signals. A simplified schematic of the optical mapping system is illustrated in Fig. 1-1. The system consists of five parts: the heart under study, light sources, a long-wavelength passing filter, a high-speed video camera, and a computer sub-system. The light sources provide illumination with a special wavelength (e.g., 500±40nm). The long-wavelength passing filter is used to filter out the reflected light components and the retention of the fluorescent components [16, 17]. The high-speed video camera captures the fluorescent signals caused by the cardiac electrical signals with high spatio-temporal resolution. The computer sub-system installed an A/D converter and a frame grabber board is used to digitize and store the sampled optical signals. A cardiac optical mapping system also includes some other auxiliary instruments, such as a xenon arc light source,

a UV blocking filter, an IR blocking filter, the blood-perfusion equipment, and an ECG-recording apparatus [16, 18].

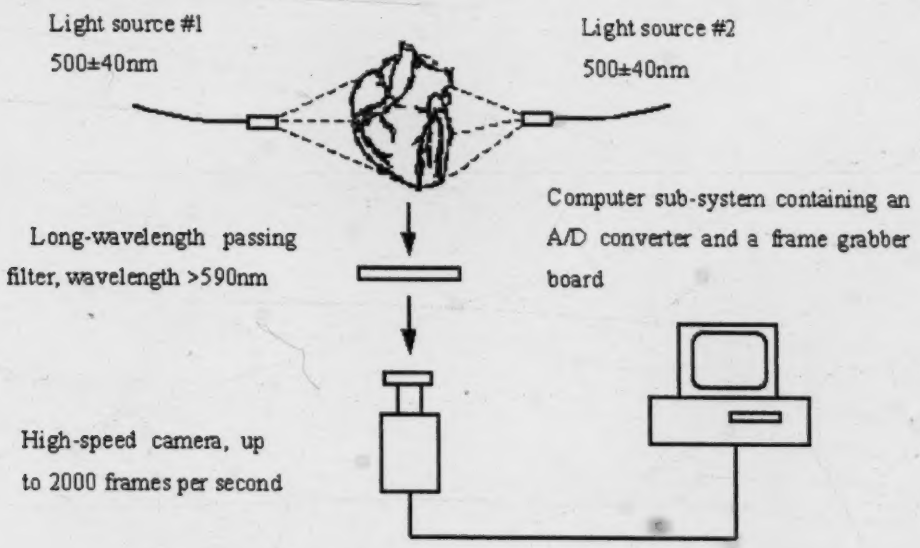
Light source #1
500±40nm
Light source #2
500±40nm
Computer sub-system containing an A/D converter and a frame grabber board
Long-wavelength passing filter, wavelength >590nm
High-speed camera, up to 2000 frames per second

Figure 1-1. The schematic diagram of a typical cardiac optical mapping system.

The optical mapping method has several advantages. First, it permits simultaneous recording of electrical signals of thousands of myocardial sites. An image with a spatial resolution of 80×80 pixels is analogous to 6400 electrodes sensing the heart electrical signals. Secondly, the temporal resolution of the cardiac optical mapping method can reach more than 2000 frames per second. Third, the spatial resolution and the temporal resolution can be altered easily. Finally, this method is free from the random interference caused by the electrodes used in the multi-electrode mapping method. The major drawbacks of this approach mainly result from the complexity of the experimental preparations and the need for open surgery.

Using the cardiac optical mapping method, a large number of videos of cardiac electrical events have been acquired. Fig. 1-2 presents two typical cardiac electrical patterns. The bright and the dark pixels represent the depolarized cells and the resting cells, respectively. It can be easily observed that the cardiac electrical patterns are extremely noisy.

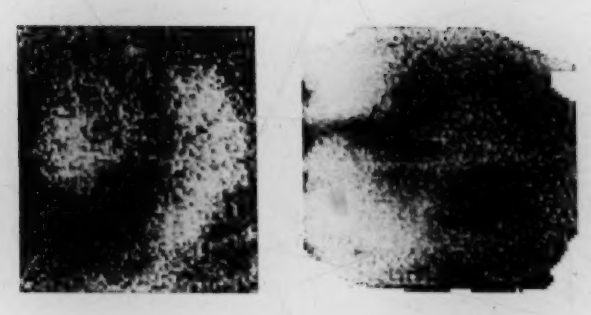

Figure 1-2. Two typical cardiac electrical patterns.

1.3 Problem definition and the research contributions

Cardiologists generally analyze the cardiac electrical patterns using their eyes and make qualitative assessment. In recent years, the quantitative analysis of the acquired data has attracted great interests from the cardiologists. Witkowski et al. [17] showed that high spatial correlation exists in sequential images acquired from a ventricle-fibrillated pig heart. Morley et al. [38] used the local velocity vectors calculated from the image sequences to illustrate the conduction properties of the mouse heart tissue. However, they did not show the method for obtaining the local velocity field. Zaitsev et al. [36] attempted to analyze the characteristics of the sheep heart data in frequency domain. They observed that the frequencies of the electrical activity in sheep hearts during VF exhibit deterministic behavior. Gray et al. [39] also found that during fibrillation, the cardiac transmembrane signals at different sites exhibit a strong periodic component centered at 8 Hz.

It can be easily observed that the cardiac electrical patterns during VF are morphologically similar to turbulent hydro-dynamical systems. Hence the techniques for analyzing the "turbulent hydro-dynamical systems" can also be applied to analyze the cardiac dynamics. Bray et al. [40] and Valderrabano et al. [41] applied the phase portrait method, a classical tool in fluid dynamics, to analyze the phase singularity dynamics in the cardiac tissues.

It has been hypothesized that the VF might be introduced from a fast expanding electrical wave, or from multiple spirals (i.e. rotors), or from multiple random wavelets in the heart, or

from all of the above. It is necessary to extract the pure expanding component and the pure rotational component from the cardiac electrical patterns such that their respective contribution to the VF can be clearly visualized and analyzed.

In this thesis, we present a new mathematical tool, the discrete Hodge-Helmholtz field decomposition (DHHFD) [48-50], to address this problem. The major contributions of this thesis are twofold:

1) A general framework for fluid motion analysis

This framework is composed of three stages: motion estimation, motion decomposition, and motion analysis. First, the velocity fields are calculated from an image sequence using a motion estimation algorithm. A pure expanding component and a pure rotational component are then extracted from an estimated velocity field using a motion decomposition technique. In the stage of motion analysis, the critical points in the fluids, such as the sources/sinks, rotational centers, and other high-order singularities, are detected. If necessary, other parameters can also be extracted from the fluid image sequence to describe the fluid motion. This framework provides a powerful tool for fluid video analysis.

2) A new way for quantitative analysis of the cardiac electrical patterns

For a long time, cardiologists have analyzed the acquired cardiac electrical data with their eyes, and hence, the analysis has been primarily qualitative in nature. Recently, some works have been done to perform quantitative analysis, however, the efficiency of the analysis is not very high. The work reported in this thesis provides an effective tool to address this problem. The detected sources/sinks may indicate the pathological changes in the heart tissue, and the specified rotational centers can be used to directly capture the rotors (or spirals) in the heart. The trajectories of these critical points may present important information about the cardiac dynamics. Moreover, this research can lead to a novel mathematical model of the cardiac electrical activity, such that the fatal VF can be effectively controlled.

1.4 Organization of the thesis

The remainder of this thesis is organized as follows. Selected background materials, such as cardiac electro-physiology, image smoothing algorithms, motion estimation algorithms, motion decomposition methods, and a few phase portrait methods for critical point detection are reviewed in Chapter 2. A simplified 2-D DHHFD algorithm based on the regular triangular grids is proposed in Chapter 3. The computational complexity of the proposed 2-D DHHFD algorithm is analyzed and compared to that of the implementation based on the irregular triangular grids. Chapter 4 focuses on the cardiac video analysis, including image smoothing using the anisotropic diffusion equation, motion estimation using the optical flow constraint equation (OFCE), motion decomposition based on the 2-D DHHFD, and detection of critical points. The conclusions and future research directions are presented in Chapter 5.

Chapter 2

Review of Background Work

In this chapter, we present a brief review of background work. We first review the fundamentals of the cardiac electrophysiology in Section 2.1. We then discuss the mechanisms of the VF in Section 2.2. The pathological meanings of some particular critical points in the heart tissues are presented in Section 2.3. The image smoothing algorithms and a few selected motion estimation algorithms are reviewed in Section 2.4 and Section 2.5, respectively. Three existing motion field decomposition algorithms are reviewed in Section 2.6. In Section 2.7, three traditional approaches for detecting the critical points in a vector field are shortly introduced.

2.1 Fundamentals of cardiac electrophysiology

This section mainly presents three basic concepts of cardiac electro-physiology [46]: the cardiac transmembrane action potential, the pathway of the electrical impulses in a healthy heart, and the abnormal excitation in a fibrillated heart. In addition, the two traditional research methods, the ECG recording and the multi-electrode mapping method, will be briefly presented.

2.1.1 The cardiac transmembrane action potential

In a cardiac cycle, the cardiac action potential (CAP), or the electrical activity of a cardiac cell, is generally divided into five phases, named as phase 0, 1, 2, 3, and 4, respectively. They correspond to different status of the cardiac cells (as shown in Fig. 2-1).

Because of the selective permeability of the cardiac cell membrane to certain ions, namely, sodium (Na^+), potassium (K^+), and calcium (Ca^{2+}), there exist ion concentration gradients between the extracellular and intracellular electrolytes. The ion concentration gradients result in the negative resting transmembrane potential (about –90 mV) when a cardiac cell is not excited (i.e., at rest). This resting status of the cardiac cell corresponds to phase 4 (see Fig. 2-1).

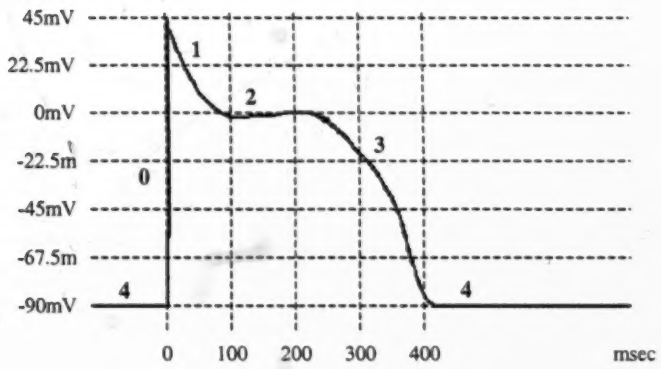

Figure 2-1. Various phases of the cardiac action potential. The numbers in bold indicate the phases of the CAP, i.e., 0: the fast depolarization, 1: the early repolarization, 2: the plateau, 3: the phase-3 repolarization, 4: the resting status.

A cardiac cell has different ion channels that automatically adjust the cell membrane permeability to specific ions. Excitation of a myocyte usually first opens the Na^+ channel, allowing an inrush of Na^+ ions, causing a rapid increase in the transmembrane potential. Once the transmembrane potential reaches a critical threshold (about –60 mV), the Na^+ channel opens wider. As a result, the membrane permeability to the Na^+ ions increases dramatically, and the transmembrane potential rapidly becomes positive. This procedure is referred to as fast depolarization, depicted as the phase 0 in Fig. 2-1.

As the Na^+ channel begins to close, Ca^{2+} channel opens (i.e. the membrane permeability to Ca^{2+} ions increases), causing an inrush of Ca^{2+} ions. After a very short time, K^+ channel also opens (i.e. the membrane permeability to K^+ ions increases), and K^+ ions rush out of the cell. Due to the higher permeability of K^+ channel, the outward flow of K^+ ions is more than the inward flow of positive ions, and hence the membrane potential decreases and becomes negative with small absolute value again. This repolarization procedure is indicated as the phase 1 in Fig. 2-1. The CAP then reaches a steady status around zero mV. This is known as plateau of the CAP, which makes up the phase 2 in Fig. 2-1. In this phase, the inward flow of Ca^{2+} ions is

roughly equal to the outward flow of K^+ ions. After a relatively long period, the permeability to Ca^{2+} ions declines, and the Ca^{2+} channel begins to close, while the K^+ channel remains open and the permeability to K^+ ions stays at a high level. This gives rise to the second repolarization as represented by the phase 3 in Fig. 2-1.

After the second repolarization, the membrane potential becomes marginally lower than the resting membrane potential for a short period of time (not shown in Fig. 2-1). In this period, the cardiac cell is hyperpolarized. The cells then return to their normal resting status corresponding to the phase 4. In phase 4, there exists an important time period, called the refractory period, in which a cell cannot be excited (absolute refractory period) or can only be excited by very strong stimuli (relative refractory period). After this refractory period, a cell can be excited by a stimulus that is stronger than the critical threshold.

An important property of the action potential (which is also observed for other cell types than cardiac cells) is known as the "all-or-nothing" principle. If the excitation of a cell does not reach the critical threshold, no action potential can be fired. On the contrary, as long as the excitation of a healthy cell reaches the threshold, an action potential of almost fixed shape will be generated.

2.1.2 The pathway of the electrical impulses in a healthy heart

A healthy heart can be considered as four pumps that are carefully controlled by an electrical system. This electrical system attempts to regulate the heart rate in a normal range, (e.g. 60-100 beats per minute for human heart in resting status). The initial electrical impulse is generated at the sino-atrial (SA) node, which is located near the top of the right atrium. When the impulse propagates downward to the atrio-ventricular (AV) node, the atria are excited and contract in a coordinated way. The electrical signal is then slightly slowed down and relayed to the bundle of His and the bundle branches in the ventricles. After passing through the left and right bundle branches, the impulse arrives at the Purkinje fibers, where it is transmitted to the muscle cells of the ventricles, causing the ventricles to concertedly contract. The normal

pathway of a healthy heart and the cardiac electrical impulses corresponding to the different heart tissue are shown in Fig. 2-2. In a healthy heart, the SA node is the dominant pacemaker.

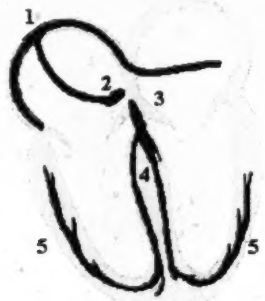

Figure 2-2. The normal pathway of a healthy heart. 1. The SA node; 2. the AV node; 3. the bundle of His; 4. the bundle branches; 5. the Purkinje fibers.

2.1.3 The abnormal excitation in a fibrillating heart

Fenton et al. [11] observed that between normal rhythm and VF, there may exist a short period of tachyarrhythmia known as ventricular tachycardia (VT). The VT has a fast heart rate (usually over 150-250 bpm) initialized in the ventricles [1]. Some non-sustained VTs can automatically return to normal heart rate, and hence they are harmless. This kind of VT may be initialized from temporary disorder of either of the ventricles. On the contrary, a heart with sustained VT is not likely to restore the normality automatically. When VT occurs, it is traditionally believed that there exists at least one additional excitation site in the ventricles, and the additional excitations take over the SA node to be the dominant pacemaker, resulting in a fast heart rhythm [1]. In this case, the ventricles do not get filled with enough blood between consecutive beats to meet the body's needs, causing dizziness. This kind of VT may progress to VF, and hence it is also life-threatening. If VF occurs, there may be multiple excitation sites in the ventricles [1]. The wavefronts of these abnormal excitations can interact with each other and with the cardiac tissue, and make the heart quivers chaotically. This chaotic quivering can pump little or no blood to the body, making the VF fatal. Fig. 2-3 illustrates the abnormal excitations of the ventricles in the case of VT and VF.

a. Abnormal excitation of VT b. Abnormal excitation of VF

Figure 2-3. Abnormal excitations in the ventricles.

2.1.4 The ECG and the multi-electrode mapping

The ECG recording and the multi-electrode mapping methods are traditionally used to monitor electrical activity of the heart. The ordinary ECG signals are sampled from limited (usually 12) selected locations on the surface of the body. Because of its simplicity, the acquisition and analysis of ECG signals are very popular for clinical practice. However, since they reflect the "integrated", rather than the "local", electrical activity of the heart, the ECG signals cannot be used to describe detailed electrophysiological characteristics of the heart. Therefore, only using the ECG signals, it is very hard to accurately locate the pathological area where the cardiac tachyarrhythmia starts [12].

Multiple electrode mapping technique can be used to measure the local cardiac electrical activity. The electrodes are arranged in a 2-D or 3-D lattice structure, such that they can immediately contact a part of the endocardial or the epicardial surface. The cardiac transmembrane action potentials at the locations where the electrodes contact the heart can be directly measured. Based on these measured transmembrane action potential values, an isochronal map can be obtained using interpolation techniques [13, 14]. The isochronal map indirectly supplies clues of the activation of the heart tissue, such as the velocities and the orientations of the cardiac electrical signals. Hence any pathological areas can be located with satisfactory accuracy from the isochronal map. An isopotential map can also be used to visualize the cardiac electrical activity at a given time [15]. Limited by the number of the

electrodes (generally less than 200), the spatial resolution of this technique is generally low.

2.2 Mechanisms of ventricular fibrillation

Although it is well known that the VF is a result of turbulent propagation of the cardiac electrical excitation wave, and it can be induced and terminated by an external electrical current (i.e., the shock signal), the real reasons for VF induction and VF termination are not completely clear. In the past 100 years, numerous theories have been reported to explain the mechanisms of the VF. Three dominant hypotheses: the multiple random wavelet hypothesis, the spiral breakup hypothesis, and the single high-frequency source hypothesis, are reviewed in the following.

2.2.1 The multiple random wavelet hypothesis

The Moe's random multiple-wavelet hypothesis has been dominated the VF explanation for more than four decades. In 1959 Moe and Abildskov [19] experimentally showed that atrial fibrillation (AF) could be introduced by the multiple circuit reentry. In 1964, Moe et al. [20] formally put forward the "multiple wavelet hypothesis" of AF. They simulated the atrial behavior using a cellular automata model (i.e. a 2-D array of coupled excitable elements) with randomly distributed refractory periods. According to this hypothesis, the AF is caused by the heterogeneity of the refractory period of the cardiac tissue. The cardiac cells with refractory periods longer than the stimulant interval cannot recover in time and fail to respond to the stimuli. This causes the fragmentation of the cardiac electrical wave and formation of the wavelets. The wavelets randomly wander in the myocardium, forming non-sustaining reentrant loops with very short lifespan. The wavelets can brake up, fuse or collide with each other and even become extinct when they reach the boundary of the myocardium or encounter refractory tissue. Therefore, the number of wavelets present in a heart, which depends on the refractory period, conduction velocity and mass of the myocardium, varies with time. Furthermore, the number of wavelets may determine the persistence of the fibrillation [20]. Below a critical number, there is a considerable chance for the wavelets to die out. When the number of the

independent wavelets exceeds the critical number, the tachyarrhythmia will be self-sustaining. Moe's hypothesis got theoretical support from Krinsky's work [21]. Allessie et al. [22] and Janse et al. [23] have revealed convincing evidence of a close correlation between the heterogeneity in the refractory periods and fibrillation.

Moe's hypothesis has successfully explained the persistence of fibrillation after the elimination of the initial triggering. However, due to the huge complexity of measuring the refractory periods at a large number of locations, it is difficult to verify this hypothesis with experiments. We still do not know if the heterogeneity in the refractory periods is really a necessary condition for both induction and maintenance of the fibrillation. New evidences obtained from the optical mapping method have shown that at least in some cases, the cardiac electrical events in fibrillation (including AF and VF) appear to have periodicity. In other words, the wavelets are not always "random" or "independent" [24, 25]. Different from Moe's hypothesis, only a small number of wavelets are found in the heart during the VF. In extreme cases, the VF can be introduced by only one wandering wavelet [26]. These inconsistencies give rise to new hypotheses.

2.2.2 The spiral breakup hypothesis

The spiral breakup hypothesis is the most widely accepted explanation about the mechanism of the VF. From the existence of a fixed pathway of the cardiac electrical impulses in a healthy heart (see Fig. 1-1), it can be inferred that the normal cardiac electrical wave on the endocardial ventricle surfaces should be parallel or quasi-parallel. Numerous experiments of multiple electrode mapping and optical mapping have proved this inference. In VT, a few big spiral waves (also referred to as mother rotors), rotating around their tips (also known as vortices), may exist in the ventricles. The tip of a spiral wave corresponds to the single abnormal excitation site mentioned before. For a self-sustained VT, the spiral waves will never restore back to the normal cardiac electrical wave, unless an external interference, such as an electrical shock, is applied. Instead, the spiral waves are likely to break up into multiple smaller

spiral waves (or daughter rotors). The daughter rotors can further split, producing more complex fragmentations and complicating the activation patterns. Excited by the extremely complicated cardiac electrical patterns, the heart loses its normal contractile function and the VF is initiated. Numerous works, such as [27-29], have been reported to support this hypothesis. The history of this theory and more comments can be seen in [30]. According to this hypothesis, the evolution of the cardiac electrical activity during VF is totally chaotic. Hence, it cannot be correctly predicted.

Some researchers believe that this understanding of VF could provide vital clues of VF control. Using this hypothesis, the VF can be terminated by preventing the mother rotors from splitting. Sinha et al. [31] obtained an unexpected low-amplitude shock threshold (on the order of mV) that could terminate the VF in a very short duration (on the order of 100 ms) using a model based on the FitzHugh-Nagumo (FHN) equations. Panfilov et al. [32] studied the elimination of a spiral wave in cardiac tissue by the application of multiple shocks using external current. Their simulation results showed that multiple shocks applied to the boundary (or edge) of the cardiac tissue could efficiently terminate a mother rotor.

The activation patterns in the spiral breakup hypothesis are the same as the wavelets in the Moe's theory except for one difference: the complex electrical patterns can be generated in both heterogeneous and homogeneous medium. However, the spiral breakup theory cannot explain the periodic activities in the real cardiac data obtained using optical mapping method.

2.2.3 The single high-frequency source hypothesis

Jais et al. [33] demonstrated that the AF could be terminated by removing the pathological "source" using a discrete radiofrequecy (RF) ablation energy. This therapy suggests that only one dominant stable abnormal excitation (rather than multiple randomly-wandering excitations as predicted by Moe's hypothesis) in the heart can induce fibrillation. Mandapati et al. [34] further confirmed that in some isolated sheep hearts, stable micro-reentrant sources could be the most likely underlying mechanism of the AF. According to their theory, the rapidly successive

wave fronts emanating from these high-frequency sources propagate through both atria and interact with heterogeneities of the medium, leading to fragmentation and wavelet formation. Similar results were obtained when analyzing the isolated rabbit hearts with ventricular fibrillation [35]. Zaitsev et al. [36] studied the excitation patterns on the epicardial and endocardial surfaces during VF in frequency domain, and found that striking simplicity and well organization existed in the typical frequency patterns. Their observation implies that the high frequency source results in multiple areas of intermittent block and complex propagating patterns with both deterministic and stochastic components because of the interaction between the waves from the source and the heterogeneities of the cardiac tissue. More comments on this hypothesis can be seen in [30, 37].

2.3 The critical points in the cardiac electrical patterns

Based on the three dominant hypotheses about the mechanisms of VF, cardiologists have realized that the critical points (also known as phase singularities) in the cardiac electrical patterns should be detected and analyzed. The most important critical points that cardiologists concern include the sources/sinks and the vortices. The detection of the critical points is helpful for understanding the cardiac dynamics.

Bray et al. [40] and Valderrabano et al. [41] primarily focused on the vortices (i.e., the tips of the spiral waves in the spiral breakup hypothesis) and they applied the phase portrait method (will be presented later) to detect the vortices in the cardiac electrical patterns.

Intuitively, a source is a small region from which the cardiac electrical signals propagate outwards to its surrounding tissues. In some literatures (such as in [33 - 37]), cardiologists also treated the tips of the spiral waves as "sources". This confusion results from that a spiral wave does contain a pure expanding component. The sources in the cardiac electrical patterns are believed to reflect the pathological changes in the heart tissues. It has been reported that at least in some cases, the atrial fibrillation (AF) and VT can be terminated by removing the abnormal sources in the atria or in the ventricles with discrete radiofrequency (RF) ablation energy [43 -

45]. Although it is not clear if the RF ablation energy can also be applied to control the VF, this method is a promising VF therapy. Success of this therapy greatly depends on the accuracy of source detection.

Compared to the source, the sink has not been paid much attention. In [47], the sink was considered as "the actual current required to excite cells downstream". According to this perspective, a sink is a region that is being depolarized. However, due to the similarity between a sink and a source, a sink should have the same pathological meaning as a source, and hence the sinks should be paid more attention.

2.4 Algorithms for image smoothing

Medical images are usually extremely noisy. To obtain superior image analysis results, image smoothing techniques are applied to reduce the noise. When the noise statistics are not known, the noise is generally treated as Gaussian noise. For Gaussian noise, the frequently used image smoothing techniques are Gaussian lowpass filter, the isotropic diffusion equation [52, 58], the anisotropic diffusion equation [53], and the wavelet thresholding and shrinkage technique [55, 56].

In Gaussian lowpass filtering, a 2-D Gaussian mask is convolved with the noisy image. The smoothed image $I(x, y)$ can be expressed as:

$$I(x, y) = I_0(x, y) * G(x, y) \tag{2-1}$$

where $I_0(x, y)$ represents the noisy image, and $G(x, y)$ represents the Gaussian mask. A shortcoming of the Gaussian filter is that it cannot correctly smooth the image boundary. When a Gaussian filter is used, the salient features, such as edges, of an input image are often blurred or shifted [50, 54]. A suitable Gaussian mask is related to the standard deviation of the noise. For an image with strong noise, the standard deviation of the noise is large, and the elements of a small Gaussian mask will be close to each other. Consequently, the performance of the Gaussian lowpass filter is similar to the averaging of neighboring pixels for an image with

strong noise. In this case, several Gaussian filters are often used in cascade.

By convolving the original image $I_0(x,y)$ with a Gaussian kernel $G(x,y,s)$ of variance s, a family of images $I(x,y,s)$ can be derived by:

$$I(x,y,s) = I_0(x,y) * G(x,y,s) \tag{2-2}$$

All smoothed images corresponding to different values of s form a scale space, and hence the variable s is also often referred to as the scale.

It can be shown that the family of filtered images, i.e. $I(x,y,s)$ in Eq. (2-2), is the solution of the isotropic diffusion equation given below:

$$\left.\frac{\partial I(x,y,s)}{\partial s}\right|_{iso} = \nabla \cdot [c \nabla I(x,y,s)] \tag{2-3}$$

with an initial condition $I(x,y,0) = I_0(x,y)$, where $\nabla I(x,y,s)$ represents the gradient map of the image $I(x,y,s)$, $\nabla \cdot$ is the divergence operator, c is the diffusion constant.

The discretization, and hence the solution of Eq. (2-3) are presented in detail in [52]. Like the Gaussian lowpass filter, the isotropic diffusion equation also smoothes the image equally in all directions. Therefore, when it smoothes a homogeneous region in an image, it also blurs the edges and is likely to shift the singularities.

To efficiently smooth the interior of each region in a noisy image while preserving the salient features, Perona et al. [53] modified the isotropic diffusion equation by replacing the constant diffusion coefficient c, with a diffusion function $c(x,y,s)$, which is a monotonically decreasing function of the image gradient magnitude:

$$c(x,y,s) = f(\| \nabla I(x,y,s) \|) \tag{2-4}$$

The new diffusion equation, known as anisotropic diffusion equation, can be expressed as:

$$\begin{cases} \left.\dfrac{\partial I(x,y,s)}{\partial s}\right|_{aniso} = \nabla \cdot \{c(x,y,s)[\nabla I(x,y,s)]\} \\ I(x,y,0) = I_0(x,y) \end{cases} \tag{2-5}$$

Note that the edges are selectively smoothed or enhanced based on the evaluation of the diffusion function. Although any monotonically decreasing continuous function of $\nabla I(x,y,s)$ can be used as a diffusion function, for simplicity of processing, the following two functions are often used:

$$c_1(x,y,s) = e^{-\frac{1}{K^2}\|\nabla I(x,y,s)\|^2} \tag{2-6a}$$

$$c_2(x,y,s) = \frac{1}{1+\frac{1}{K^2}\|\nabla I(x,y,s)\|^2} \tag{2-6b}$$

where K is a constant that controls the diffusion behavior. If K is small compared to $\|\nabla I\|$, the diffusion function $c(x,y,s)$ decreases quickly to zero. In this case, small intensity gradients are able to block the diffusion process, and hence the edges can easily be preserved. In contrast, if K is set to a large value compared to $\|\nabla I\|$, the salient features in the image are likely to be smoothed. In practice, K is chosen in the range [20 – 100] for the best performance. It should also be emphasized that Eq. (2-6a) favors the high contrast edges over the low contrast ones, and Eq. (2-6b) favors large regions over the small ones.

Using the finite difference method, Eq. (2-5) can be easily discretized as [53]:

$$I_{i,j}^{n+1} = I_{i,j}^{n} + \lambda\left[c_N \cdot \Delta_N I + c_S \cdot \Delta_S I + c_E \cdot \Delta_E I + c_W \cdot \Delta_W I\right]_{i,j}^{n} \tag{2-7}$$

where $I_{i,j}^{n+1}$ is the smoothed image after $n+1$ iterations, i and j indicate the pixel location, λ (essentially the scale step, i.e., $\lambda = \Delta s$) is a constant in the range [0, 0.25] for stability, $\Delta_N I_{i,j}$, $\Delta_S I_{i,j}$, $\Delta_E I_{i,j}$, and $\Delta_W I_{i,j}$ are the brightness variations of the pixel

$I(i,j)$ in four directions (North, South, East, and West), and they are expressed as:

$$\begin{aligned}
\Delta_N I_{i,j} &= I_{i-1,j} - I_{i,j} \\
\Delta_S I_{i,j} &= I_{i+1,j} - I_{i,j} \\
\Delta_E I_{i,j} &= I_{i,j+1} - I_{i,j} \\
\Delta_W I_{i,j} &= I_{i,j-1} - I_{i,j}
\end{aligned} \tag{2-8}$$

In Eq. (2-7), $c^n_{N\,i,j}$, $c^n_{S\,i,j}$, $c^n_{E\,i,j}$, and $c^n_{W\,i,j}$ represent four diffusion functions in the four directions (i.e., North, South, East, and West) after n iterations, and they are expressed as:

$$\begin{aligned}
c^n_{N\,i,j} &= f(|\Delta_N I^n_{i,j}|) \\
c^n_{S\,i,j} &= f(|\Delta_S I^n_{i,j}|) \\
c^n_{E\,i,j} &= f(|\Delta_E I^n_{i,j}|) \\
c^n_{W\,i,j} &= f(|\Delta_W I^n_{i,j}|)
\end{aligned} \tag{2-9}$$

Note that the Eq. (2-7) implies a recursive smoothing of the image. This recursive process usually takes longer computational time than the Gaussian filter. One side effect of the anisotropic diffusion equation is that it often introduces staircases around the pattern boundaries. Excellent comments and techniques to eliminate this drawback can be found in [59 - 61].

The wavelet-based image de-noising technique, proposed by Donoho and Johnstone [55], makes use of the excellent energy compaction capability of the wavelet transform. Here, the image is typically represented by one lowpass subband and several highpass subbands. The small coefficients in the highpass subbands mostly represent the noise and the large coefficients represent the signals. In these subbands, each coefficient is compared to a certain threshold. If the coefficient is less than the threshold, it is shrunk to zero; otherwise, it is kept or shrunk to another value depending on the thresholding rule. A de-noised image can be reconstructed by inversely transforming the thresholded wavelet coefficients back to image domain.

Although the original algorithm of the wavelet thresholding provides excellent de-noising performance for 1-D signal, it is likely to introduce artifacts when applied to multi-dimensional signals. For instance, a wavelet de-noised image often contains ripples near the edges or region

boundaries. This might result from the fixed threshold used in an entire subband. It has been reported that the use of adaptive thresholds, which are driven by the datasets in the wavelet domain, can significantly improve the performance [57].

2.5 Motion estimation algorithms

Although a large number of motion estimation algorithms have been proposed, most of them can be classified into four categories: the techniques based on (i) the optical flow constraint equation (OFCE), (ii) the block matching algorithm (BMA), (iii) the statistical model of the motion vectors, and (iv) the phase correlation. The OFCE-based algorithm and the BMA are widely used, and hence they are presented in the following sub-sections in more detail. The spatio-temporal auto-regression (STAR) model, one of the statistics based algorithm, and the phase correlation based algorithm will be briefly introduced.

2.5.1 The OFCE-based algorithm

The OFCE-based algorithm [51] is an efficient motion estimation algorithm. It assumes that the brightness of the pixel roughly remains unchanged after its movement. The formulation of this algorithm requires that the pixel move very slowly. If the pixel moves too fast, this algorithm will fail. This algorithm also assumes that a motion vector cannot deviate from its neighboring motion vectors too much.

Let the two consecutive frames from an image sequence be denoted as frame-1 and frame-2, and let the brightness of a pixel located at (x, y) in frame-1 be expressed as $I(x, y, t)$, where t indicates time. At time $t + dt$, this pixel moves to a new location $(x + dx, y + dy)$, and its brightness can be expressed as $I(x + dx, y + dy, t + dt)$. Assume that the brightness of the pixel remains identical after its movement. After simple manipulations, this assumption leads to the following Optical Flow Constraint Equation (OFCE):

$$I_x u + I_y v + I_t \approx 0 \qquad (2\text{-}10)$$

where I_x, I_y and I_t represent the partial derivatives of image brightness with respect to x, y and t, respectively; while u and v are the velocities in horizontal and vertical directions. Note that the brightness variation of a single pixel may greatly affect the values of the I_x, I_y and I_t. Hence, Eq. (2-10) is very sensitive to the brightness variation of the pixels

Since there are two variables u and v in Eq. (2-10), unique solution of u and v is not possible. Hence, rectangular mesh grids are used. This setting is based on the assumption that a block of pixels shares the same motion vector. To obtain a smooth velocity field, another constraint equation, known as smoothness constraint, is applied. This constraint assumes that the brightness of the target varies smoothly over a short time period. This assumption implies that the motion vector at a certain location is roughly equal to the average of those of its neighbours. Let us define $(\bar{u},\bar{v})$ as the average of (u,v) pairs of a 3×3 neighborhood as shown in Fig. 2-4. Hence, $(\bar{u},\bar{v})$ can be expressed as:

$$(\bar{u},\bar{v})=\left(\frac{1}{8}\sum_{i=1}^{8}u_i,\ \frac{1}{8}\sum_{i=1}^{8}v_i\right) \tag{2-11}$$

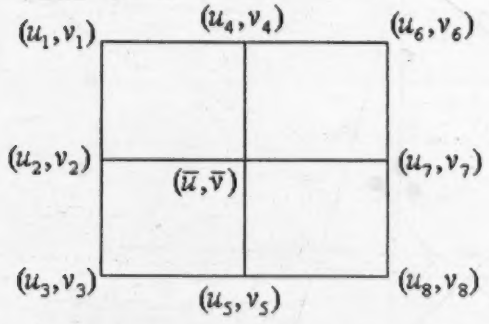

Figure 2-4. Definition of the average motion vector.

The smoothness constraint on the whole image domain Ω can then be expressed as minimization of the following energy functional:

$$P_2(u,v) = \int_{\Omega} (\bar{u}-u)^2 + (\bar{v}-v)^2 d\Omega \tag{2-12}$$

Combining the two constraints, the following energy equation is obtained:

$$P(u,v) = \int_{\Omega} \{(I_x u + I_y v + I_t)^2 + \lambda^2[(\bar{u}-u)^2 + (\bar{v}-v)^2]\} d\Omega \tag{2-13}$$

where $\lambda \in [0,\infty)$ is a trade-off factor between sensitivity and smoothness. In OFCE-based algorithm, the optima motion vector is obtained by minimizing $P(u,v)$ in Eq. (2-12) on Ω.

In order to minimize the $P(u,v)$, we use the two conditions $\partial P/\partial u = 0$ and $\partial P/\partial v = 0$. We obtain:

$$\frac{\partial P}{\partial u} = 2I_x(I_x u + I_y v + I_t) - 2\lambda^2(\bar{u}-u) = 0 \tag{2-14a}$$

and

$$\frac{\partial P}{\partial v} = 2I_y(I_x u + I_y v + I_t) - 2\lambda^2(\bar{v}-v) = 0 \tag{2-14b}$$

Solving Eqs. (2-13a) and (2-13b), the motion vector (u,v) can be written as:

$$u = \bar{u} - \frac{I_x\bar{u} + I_y\bar{v} + I_t}{K} I_x \tag{2-15a}$$

and

$$v = \bar{v} - \frac{I_x\bar{u} + I_y\bar{v} + I_t}{K} I_y \tag{2-15b}$$

where

$$K = I_x^2 + I_y^2 + \lambda^2 \tag{2-16}$$

In practice, Eqs. (2-15a) and (2-15b) can be implemented using an iterative scheme:

$$u^{n+1} = \bar{u}^n - \frac{I_x\bar{u}^n + I_y\bar{v}^n + I_t}{K} I_x \tag{2-17a}$$

and

$$v^{n+1} = \overline{v}^n - \frac{I_x \overline{u}^n + I_y \overline{v}^n + I_t}{K} I_y \tag{2-17b}$$

Note that the $(\overline{u}^n, \overline{v}^n)$ in Eq. (2-17) can be solved using the following iterative expression:

$$\overline{u}^n = \frac{1}{8} \sum_{i=1}^{8} u_i^n \tag{2-18a}$$

and

$$\overline{v}^n = \frac{1}{8} \sum_{i=1}^{8} v_i^n \tag{2-18b}$$

where the (u_i, v_i) pairs have been shown in Fig. 2-4.

The initial (u^0, v^0) pair can be arbitrary numbers. After several (e.g., 100 - 1000) iterations, the (u, v) pair reaches to a stable solution. This iterative scheme can be considered as a coarse-to-fine estimation.

Although it has been used by many researchers, the OFCE-based algorithm is very sensitive to variation of a single pixel and suitable only for slow image motion. For an image sequence with fast motion, this algorithm often fails, because Eq. (2-10) is not valid in this case.

2.5.2 The block matching algorithm

The block matching algorithm (BMA) [69] is one of the most frequently used motion estimation algorithms, especially in video coding applications. This algorithm assumes that a block of pixels has the same translation motion vector from one image frame to another, and the motion vectors are smaller than a pre-estimated threshold (i.e., the search region). The key idea of BMA is to search the mutual corresponding blocks in two image frames. In other words, the BMA finds the shortest distance between two brightness patterns in two local regions, one in each video frame. The following distance functional is generally minimized to estimate a motion vector from the block $I(x, y, t)$ to the block $I(x+u, y+v, t+1)$:

$$D(u,v) = \sum_x \sum_y | I(x+u, y+v; t+1) - I(x,y,t) |^2 \qquad (2\text{-}19)$$

Using an exhaustive searching scheme, the optimal motion vector, which corresponds to the shortest distance, can be obtained. The BMA can handle fast motion by pre-setting a large search region. However, a large search region leads to dramatic increase of the computational complexity. Several sub-optimal searching schemes have been proposed to speed up the motion estimation (see [70, 71]). Derived from the block comparison rather than pixel correspondence, the BMA is not sensitive to brightness change of a single pixel.

2.5.3 The spatio-temporal auto-regression motion model

The spatio-temporal auto-regression (STAR) model based algorithm, recently proposed by Chang et al. [72], assumes that a pixel in an image frame can be treated as a linear combination of its neighboring pixels in the next frame. The motion vector at a source location at a given time can be considered as a random variable with a probability distribution function. The optimal motion vector is most likely to be the vector with highest probability. This algorithm further assumes that the probability distribution function is proportional to the correlation coefficient, and hence the motion vector can be determined by searching the highest correlation coefficient between two pixel blocks. As the STAR model based algorithm uses the same idea as that of the BMA, it is essentially a variation of the BMA.

2.5.4 The phase correlation based algorithm

Phase correlation based algorithm is a frequency domain motion estimation method that makes use of the shifting property of the Fourier Transform (FT). Note that a spatial shift in the image domain is equivalent to a phase shift in the frequency domain [73]. If $I_1(x,y)$ and $I_2(x,y)$ are two brightness patterns before and after a motion $\vec{\xi} = (u,v)$, then $I_2(x,y) = I_1(x+u, y+v)$. If the FT of I_1 and I_2 are denoted by $F(I_1)$ and $F(I_2)$,

respectively, the following relationship can be obtained:

$$F(I_2)(\omega_x,\omega_y)=e^{j(u\omega_x+v\omega_y)}F(I_1)(\omega_x,\omega_y) \tag{2-20}$$

The phase correlation is then defined as:

$$\frac{F(I_2)F^*(I_1)}{|F(I_1)|^2}=e^{j(u\omega_x+v\omega_y)} \tag{2-21}$$

The "*" indicates complex conjugate operator. Note that the Inverse Fourier Transform (IFT) of the right-hand side of Eq. (2-21) is a single pulse at (u,v). Therefore, the motion vector $\vec{\xi}=(u,v)$ can be obtained from the IFT of the left-hand side of Eq. (2-21).

The phase correlation based algorithm provides a new perspective to understand the motion activity in an image sequence, but it is not as widely accepted as the BMA and OFCE-based algorithms. According to Hill's comments [74], phase correlation is not suitable for small images, because the number of samples used by FT determines the resolution in the frequency domain. Hence the use of small images limits the accuracy of this algorithm.

2.6 Motion field decomposition

A complex motion field generally contains rich information about the target. Sometimes, we only need to analyze selected motion information while ignoring others. Hence, it is necessary to separate the needed components from the complex motion field. In the following subsections, a few existing vector field decomposition techniques are discussed.

2.6.1 Local translation decomposition and singular value decomposition

Lawton and Gardner [76] presented a low-level local translational decomposition (LTD), which can separate the pure translation field from a given motion field. However, this work did not attract much attention from the research community. Black et al. [77] proposed a parametric

motion model that decomposes a complex motion field using the singular value decomposition (SVD). The authors succeeded in applying this model to represent the motions of different facial expressions and gaits. This motion description method is simple to implement. In fluid motion analysis, important features, such as the singularities, are often needed to describe the fluidal structures. Unfortunately, the above two motion descriptions (LTD and SVD) cannot provide any information of the singularities about the fluid motion. Moreover, the motion parameters as well as the basis motions do not have any direct physical meanings in the SVD-based motion decomposition framework.

2.6.2 The discrete Hodge-Helmholtz field decomposition

The Hodge-Helmholtz decomposition [75] is a convenient method to decompose a continuous vector field into three components: a curl-free component, a divergence-free component, and a harmonic remainder. Polthier and Preuβ [48] recently showed that this decomposition can also be extended to decompose a discrete vector field. They have also presented a numerical algorithm to implement the 2-D field decomposition using the finite element method (FEM) [49]. Later, Tong et al. [50] further extended the 2-D discrete Hodge-Helmholtz field decomposition (DHHFD) to analyze 3-D vector fields. All these works deal with the decomposition of general vector fields, and hence they all utilize the irregular grids. As a result, their implementations have high computational complexity.

The 2-D DHHFD is illustrated in Fig. 2-5.

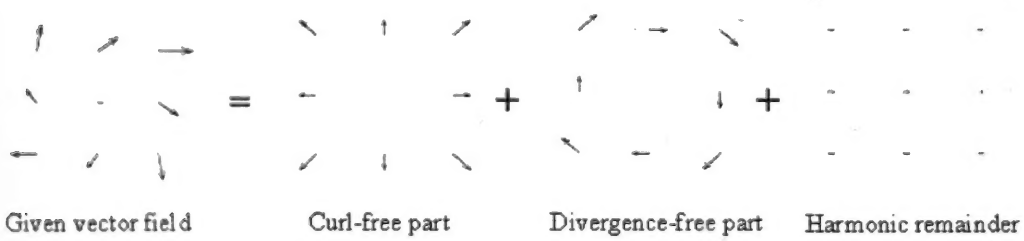

Figure 2-5. Illustration of the 2-D DHHFD.

Although there exists an analytical solution to the decomposition of a continuous vector field [75], it is not feasible to directly apply the continuous Hodge-Helmholtz field decomposition to decompose a discrete vector field. The numerical approximation of the decomposition of a discrete vector field is the only possible way.

In the DHHFD, an arbitrary flow field $\vec{\xi}$ can be expressed as:

$$\vec{\xi} = (\nabla E) + (\nabla \times \vec{W}) + \vec{R} \tag{2-22}$$

where ∇E is the curl-free part (satisfying $\nabla \times (\nabla E) = \vec{0}$), $\nabla \times \vec{W}$ is the divergence-free part (satisfying $\nabla \cdot (\nabla \times \vec{W}) = 0$) and $\vec{R}$ is the harmonic remainder part (satisfying $\nabla \cdot \vec{R} = 0$ and $\nabla \times \vec{R} = \vec{0}$ simultaneously). Note that ∇, $\nabla \cdot$, and $\nabla \times$ refer to the gradient operator, the divergence operator, and the curl operator, respectively. E is a scalar potential function of ∇E, and $\vec{W}$ is a vector potential function of $\nabla \times \vec{W}$. Because $\nabla \times$ is a 3-D vector operator, all variables in Eq. (2-22), i.e. $\vec{\xi}$, ∇E, $\nabla \times \vec{W}$ and $\vec{R}$, are 3-D vectors. Therefore, when the 3-D DHHFD is directly applied to decompose a 2-D vector field, the input 2-D vector field $\vec{\xi}$ has to be extended to 3-D form by setting its 3rd component to zero.

2.7 Critical point detection in a fluid image sequence

The critical points, such as sources, sinks, vortices, rotational centers, and saddles, are the basic structural features of a fluid motion field. Hence the detection of these critical points is very important for the analysis of fluid motion. Traditionally, this task can be accomplished by exploiting the phase portrait of the fluid vector field. The phase portrait draws the trajectories of the particles in the fluid, and hence it describes the streamlines of the fluid field [79]. Fig. 2-6 shows the phase portraits of six fundamental fluid motions [78]. Note that the nodes, centers, spirals, and saddles in the phase portrait respectively correspond to the sources/sinks, rotational centers, vortices, and saddles in the vector field.

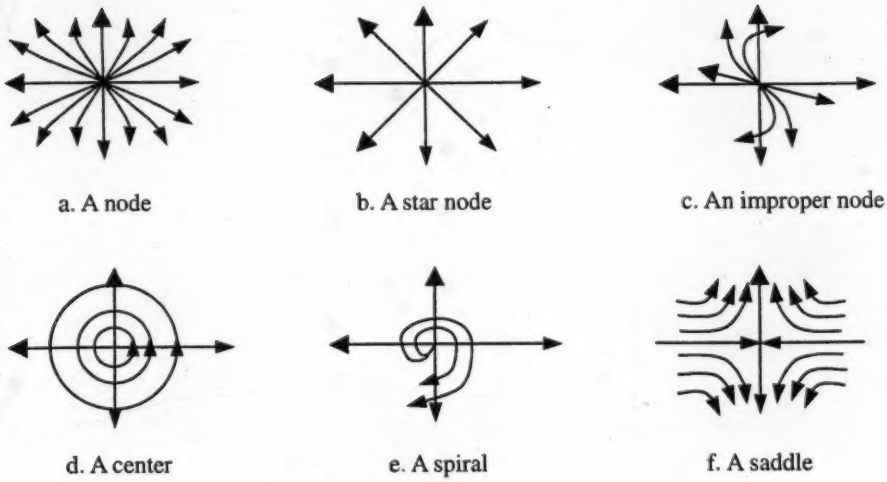

Figure 2-6. The phase portraits of six fundamental fluid motions.

There are several methods to detect the critical points in a fluid motion field. We discuss three phase portrait based methods in the following.

Method-1. Here, a set of isoclines is used to detect some particular critical points, such as sources, vortices, and saddles [79]. The isoclines are window-clipped straight lines emanating from the local origin as shown as Fig. 2-7. The window (shown as the bold dashed box) keeps shifting in the vector field. Let us use α and θ to denote the inclination of an isocline and the orientation angle of the vector valued at the point where the isocline intersects a streamline, respectively. If $\frac{\partial \theta}{\partial \alpha}$ is always positive, the local origin is a source or a vortex; if $\frac{\partial \theta}{\partial \alpha}$ is always negative, the local origin is a saddle.

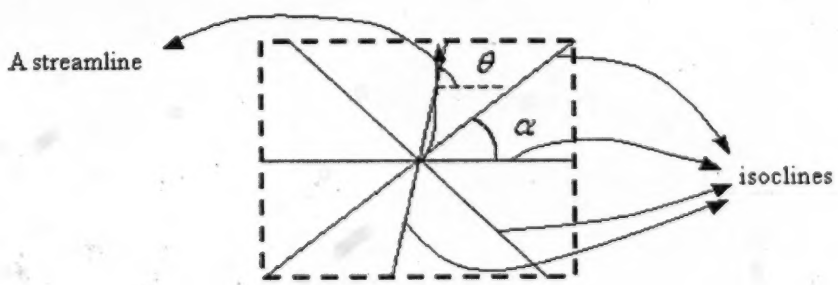

Figure 2-7. Window-clipped isoclines.

Method-2. Here, the index of the Jordan curve is used to detect the fluid structure [78, 81, 82]. A Jordan curve is a simple and closed plane curve, which is topologically equivalent to the unit circle. As shown in Fig. 2-8, the Jordan curve intersects a streamline at a point where the orientation angle of the streamline is denoted as θ. Traveling one lap anticlockwise along the Jordan curve, if the local origin is a source or a vortex, the change of θ (denoted as $\Delta\theta$) should be 2π; if the local origin is a saddle, $\Delta\theta$ should be -2π.

The index of a Jordan curve is defined as:

$$Index(J) = \frac{\Delta\theta}{2\pi}$$

Therefore, if the local origin is a source or a vortex, the index of the Jordan curve is 1; if the local origin is a saddle, the index of the Jordan curve is -1.

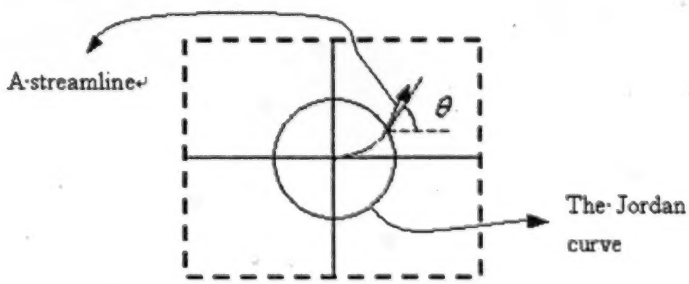

Figure 2-8. Index of a Jordan curve.

Method-3. Here, the motion field in a local window is expressed as an affine model [78]:

$$\begin{bmatrix} u(x,y) \\ v(x,y) \end{bmatrix} = A\vec{X} + b$$

where $\vec{X} = (x, y)$ is a pixel location, u and v are the velocity components valued at $\vec{X}$, and A is a 2×2 matrix. Note that A is not a constant matrix, and all four elements of matrix A depend on the spatial location $\vec{X}$. The critical points can be detected according to the eigenvalues of the matrix A. The relationship between the phase portrait structure and the

eigenvalues of A is presented in Table 2-1.

The phase portrait based methods have been widely used to analyze the fluid dynamics [79 - 81]. However, the former two methods (Methods 1 and 2) cannot correctly distinguish the sources from the vortices, and cannot correctly detect the rotational centers. These methods need to slide the window and calculate the features pixel-by-pixel, resulting in intensive computation [80, 83, 84].

Table 2-1. Eigenvalues of the matrix A and the corresponding phase portraits.

Eigenvalues of A	**Jordan form**	**Type**	**Phase portrait**
$\lambda_1 \neq \lambda_2$, and both of them are real number	$\begin{bmatrix} \lambda_1 & 0 \\ 0 & \lambda_2 \end{bmatrix}$, and λ_1 and λ_2 have same sign	Node	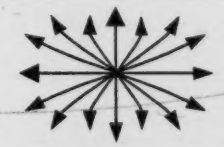
	$\begin{bmatrix} \lambda_1 & 0 \\ 0 & \lambda_2 \end{bmatrix}$, and λ_1 and λ_2 have opposite sign	Saddle	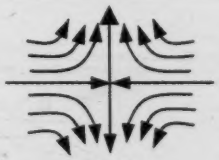
$\lambda_1 = \lambda_2$	$\begin{bmatrix} \lambda_1 & 0 \\ 0 & \lambda_1 \end{bmatrix}$	Star-node	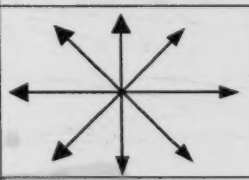
	$\begin{bmatrix} \lambda_1 & 1 \\ 0 & \lambda_1 \end{bmatrix}$	Improper node	
$\lambda_{1,2} = \alpha \pm i\beta$	$\begin{bmatrix} 0 & -\beta \\ \beta & 0 \end{bmatrix}$, $\alpha = 0$	Center	
	$\begin{bmatrix} \alpha & -\beta \\ \beta & \alpha \end{bmatrix}$, $\alpha \neq 0$	Spiral	

2.8 Summary

In this Chapter, the fundamentals of the cardiac electro-physiology have been reviewed first. The properties of the cardiac transmembrane action potential provide meaningful clues for choosing an appropriate motion estimation algorithm. The pathway of the cardiac electrical impulses in a healthy heart and the abnormal excitation in a fibrillated heart are helpful for understanding the abnormal cardiac electrical activity. The two traditional methods in cardiology research provide widely accepted results that can be compared to those obtained from the optical mapping method. The three widely accepted explanations about the mechanisms of VF indicate an important research direction: to capture the high-frequency sources/sinks and the vortices. Based on this indication, the pathological meanings of these critical points have also been introduced.

A few selected image processing techniques have also been reviewed. An image smoothing technique can be used to filter out the noise in the acquired cardiac electrical patterns. A motion estimation algorithm can recover a motion field from two consecutive image frames. A motion decomposition algorithm can extract the needed motion components while ignoring others. Finally, we have also presented three phase portrait based methods for detecting the critical points in a fluid vector field. Due to the need for a moving window and the reconstruction of the streamlines, all the three methods are highly computation-intensive.

Chapter 3

Efficient Hodge-Helmholtz Decomposition of Motion Fields

In Chapter 2, a brief review of various video processing techniques was presented. It was observed that motion analysis is an important tool for video analysis. A motion field provides information about the motion of various objects in a video, and hence many important features, such as the contour of a target [85], can be extracted from a motion field. In fluid motion analysis, it is often required to extract a few components of interest from a given complex motion field [65, 77] such that the contributions of different components to the fluid behavior can be quantitatively evaluated.

In Section 2.6.2, we introduced the basic idea of the discrete Hodge-Helmholtz field decomposition (DHHFD). Two implementations (2-D and 3-D) were briefly discussed based on irregular grids. However, both these implementations are highly computation-intensive because of the use of irregular grids. Note that regular rectangular grids are generally used in most existing motion estimation algorithms. The use of regular grids greatly simplifies the problem while preserving enough accuracy. In order to apply the DHHFD to efficiently analyze the image motion fields, it is necessary to re-derive the DHHFD using regular grids.

In this chapter, we present an efficient implementation of the DHHFD based on regular triangular grids (RTG). Sections 3.1 and 3.2 introduce the theory of the DHHFD based on RTG (DHHFD-RTG). We then present the properties of DHHFD in Section 3.2. Exploiting these three properties, the implementation details of the DHHFD-RTG are presented in Section 3.3. The computational complexities of the DHHFD-RTG and the DHHFD based on irregular triangular grids (DHHFD-ITG) are analyzed and compared in Section 3.4. In Section 3.5, a synthetic complex vector field is decomposed using the proposed 2-D DHHFD-RTG algorithm, to demonstrate the performance of the 2-D DHHFD-RTG.

3.1 The Proposed 2-D DHHFD-RTG

As mentioned in Section 2.6.2, an arbitrary (continuous or discrete) vector field can be uniquely decomposed into three components using DHHFD: a divergence-free part, a curl-free part, and a harmonic remainder.

The task is to derive the 2-D DHHFD-RTG algorithm, starting from Eq. (2-22) that is essentially the expression of 3-D DHHFD based on irregular tetrahedral grids. We also use the FEM, mimicking the works done by Polthier et al. [49] and Tong et al. [50], to re-derive the 2-D DHHFD. In order to efficiently apply the 2-D DHHFD to video analysis, our derivation makes use of the RTG.

3.1.1 Setup of RTG and notations

Assume that the image domain Ω is divided into triangular grids as shown in Fig. 3-1. This can be easily achieved by dividing each rectangular grid used in a conventional motion estimation algorithm into two triangles. We assume that $\vec{\xi}$ is an estimated motion field with $M \times N$ motion vectors, and each motion vector is valued at the grid nodes. It is easy to count that there are $M * N$ nodes and $2*(M-1)*(N-1)$ triangle grids on the image domain Ω. Table 3-1 explains some important mathematical symbols.

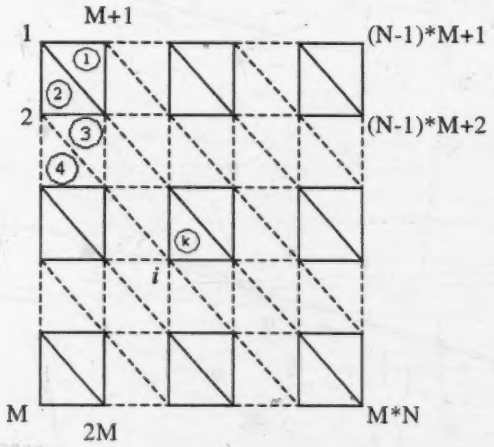

Figure 3-1. Triangulation of the image domain Ω

Table 3-1. The symbols and their meanings.

Symbols	Meanings
L	The total number of the nodes on the image domain Ω, and $L = M * N$
$\vec{p}$	An arbitrary location inside the image domain, $\vec{p} = (x, y)$
$\vec{p}_i$	The location of the i^{th} node on the image domain Ω, indicated by the *italic* letter "*i*" in Fig. 3-1.
T_k	The k^{th} triangle on the image domain Ω, indicated by the circled letter "k" in Fig. 3-1.
E_i	The potential E in Eq. (2-22) valued at $\vec{p}_i$
$\vec{W}_i$	The potential $\vec{W}$ in Eq. (2-22) valued at $\vec{p}_i$
$\vec{\xi}_k$	The motion vector estimated at the geometrical center of the triangle T_k

The two continuous potential functions E and $\vec{W}$ are discretized as two $M \times N$ matrices. These matrices can be expressed as:

$$E = \begin{bmatrix} E_1 & E_{M+1} & \cdots & E_{(N-1)*M+1} \\ E_2 & E_{M+2} & \cdots & E_{(N-1)*M+2} \\ \cdots & \cdots & \cdots & \cdots \\ E_M & E_{2M} & \cdots & E_{M*N} \end{bmatrix} \tag{3-1a}$$

and

$$\vec{W} = \begin{bmatrix} \vec{W}_1 & \vec{W}_{M+1} & \cdots & \vec{W}_{(N-1)*M+1} \\ \vec{W}_2 & \vec{W}_{M+2} & \cdots & \vec{W}_{(N-1)*M+2} \\ \cdots & \cdots & \cdots & \cdots \\ \vec{W}_M & \vec{W}_{2M} & \cdots & \vec{W}_{M*N} \end{bmatrix} \tag{3-1b}$$

By re-organizing these two matrices column-wise, E and $\vec{W}$ can be expressed as two $L\times 1$ vectors. Note that $L = M * N$. In other words, $E = (E_1, E_2, \cdots, E_L)^T$ and $\vec{W} = (\vec{W}_1, \vec{W}_2, \cdots, \vec{W}_L)^T$, respectively.

The velocity $\vec{\xi}_k$ has been defined in Table 3-1 as the average of the three motion vectors at the vertices of the triangle T_k. Hence, $\vec{\xi}_k$ can be calculated as:

$$\vec{\xi}_k = \frac{1}{3}\sum_{i\in T_k}\vec{\xi}_i, \quad k \in [1, 2*(M-1)*(N-1)] \tag{3-2}$$

We further assume that the potential functions, E and $\vec{W}$, are piece-wise linear, and hence, their first-order derivatives ∇E and $\nabla\times\vec{W}$ are piece-wise constant. Let a piecewise-linear basis function $\phi_i(\vec{p})$ be defined as 1 at the i^{th} node $\vec{p}_i$ and 0 at all other nodes (as illustrated as Fig. 3-2).

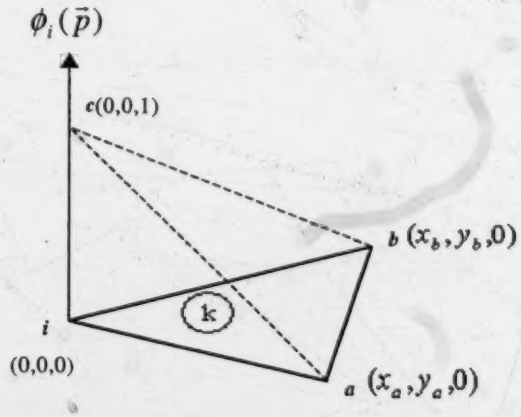

Figure 3-2. Definition of the piecewise-linear basis function.

In the later context, we also use $\phi_{ik}(\vec{p})$ to represent the $\phi_i(\vec{p})$ belonging to T_k. Note that the i^{th} node is shared by several triangles. Assume that T_k is a neighboring triangle of

the i^{th} node, and in addition to the i^{th} node, let the other two vertices of the triangle T_k be denoted as node a and node b. The sequence of nodes i, a, and b are strictly arranged in anticlockwise order. $\vec{p}_a$, $\vec{p}_b$ are the locations of nodes a and b on the image domain Ω, respectively. According to the definition of $\phi_i(\vec{p})$, we have,

$$\begin{aligned} &\phi_i(\vec{p}) = \phi_i(\vec{p}_i) = 1, \text{ if } \vec{p} = \vec{p}_i; \\ &\phi_i(\vec{p}) = \phi_i(\vec{p}_a) = 0, \text{ if } \vec{p} = \vec{p}_a; \\ &\phi_i(\vec{p}) = \phi_i(\vec{p}_b) = 0, \text{ if } \vec{p} = \vec{p}_b. \end{aligned} \tag{3-3}$$

As shown in Fig. 3-2, we build a local coordinate system, such that the i^{th} node is treated as the origin, and the coordinate of the auxiliary point c is $(0,0,1)$. For the sake of generality, we assume that the coordinates of nodes a and b are $(x_a, y_a, 0)$ and $(x_b, y_b, 0)$ in this local coordinate system. Note that the plane abc can be expressed as:

$$d_x x + d_y y + d_\phi \phi_i + d_0 = 0 \tag{3-4}$$

where d_x, d_y, d_ϕ, and d_0 are constant coefficients. Substituting the coordinates of points a, b, and c into Eq. (3-4), the following equation can be obtained:

$$\phi_i(\vec{p}) = \phi_i(x, y) = \left(\frac{y_b - y_a}{Z_k} \right) x + \left(\frac{x_a - x_b}{Z_k} \right) y + 1 \tag{3-5}$$

where

$$Z_k = y_a x_b - x_a y_b \tag{3-6}$$

On the image domain Ω, it can easily be shown that Z_k is always positive, and $Z_k = 2A_k$, where A_k is the area of the triangle T_k. Eq. (3-5) shows that the gradient of $\phi_i(\vec{p})$ corresponding to the triangle T_k is:

$$\nabla\phi_{ik} = \left(\frac{y_b - y_a}{2A_k}, \frac{x_a - x_b}{2A_k} \right) \tag{3-7}$$

Note that the gradient $\nabla\phi_{ik}(\vec{p})$ is the vector normal to the triangle abc in Fig. 3-2, and the direction of this normal vector complies with the right-hand rule. Extending Eq. (3-7) to 3-D form, we obtain:

$$\nabla\phi_{ik} = \left(\frac{y_b - y_a}{2A_k}, \frac{x_a - x_b}{2A_k}, 0 \right) \tag{3-8a}$$

Similarly, the gradients of $\phi_a(\vec{p})$ and $\phi_b(\vec{p})$ can be obtain as:

$$\nabla\phi_{ak} = \left(\frac{y_i - y_b}{2A_k}, \frac{x_b - x_i}{2A_k}, 0 \right) \tag{3-8b}$$

$$\nabla\phi_{bk} = \left(\frac{y_a - y_i}{2A_k}, \frac{x_i - x_a}{2A_k}, 0 \right) \tag{3-8c}$$

The two potential functions can be approximately represented as superposition of $\phi_i(\vec{p})$:

$$E(\vec{p}) = \sum_{i=1}^{L} \phi_i(\vec{p}) E_i \tag{3-9a}$$

$$\vec{W}(\vec{p}) = \sum_{i=1}^{L} \phi_i(\vec{p}) \vec{W}_i \tag{3-9b}$$

where E_i and $\vec{W}_i$ are potentials E and $\vec{W}$ valued at $\vec{p}_i$.

3.1.2 Computing the curl-free component

The curl-free component ∇E of the motion field $\vec{\xi}$ is the projection of $\vec{\xi}$ onto the space of curl-free fields. The distance between $\vec{\xi}$ and ∇E can be expressed as:

$$D(E) = \int_{\Omega} \| \nabla E - \vec{\xi} \|^2 d\Omega \tag{3-10}$$

To find the optimal ∇E, the distance $D(E)$ in Eq. (3-10) needs to be minimized. Applying

the necessary condition $\partial D/\partial E_i = 0$ and using Eq. (3-9a), we obtain (see Appendix A):

$$\forall i, \int_{\Omega} \nabla \phi_i \cdot (\nabla E - \vec{\xi}) d\Omega = 0 \tag{3-11}$$

or

$$\forall i, \int_{\Omega} (\nabla \phi_i \cdot \nabla E)\ d\Omega = \int_{\Omega} (\nabla \phi_i \cdot \vec{\xi})\ d\Omega \tag{3-12}$$

Eq. (3-12) can be approximately re-written at each node as a simple sum over the neighbouring triangles:

$$\forall i, \sum_{T_k \in N(i)} [\nabla \phi_{ik} \cdot (\nabla E)_k] A_k = \sum_{T_k \in N(i)} (\nabla \phi_{ik} \cdot \vec{\xi}_k) A_k \tag{3-13}$$

where $N(i)$ is the set of all triangles immediately adjacent to the i^{th} node. Note that the areas of all triangles on Ω are identical in our case, and hence Eq. (3-13) can be further simplified as:

$$\forall i, \sum_{T_k \in N(i)} [\nabla \phi_{ik} \cdot (\nabla E)_k] = \sum_{T_k \in N(i)} (\nabla \phi_{ik} \cdot \vec{\xi}_k) \tag{3-14}$$

Expanding both sides of Eq. (3-14), we get a linear equation (see Appendix B):

$$S_1 E = B \tag{3-15}$$

where S_1 is an $L \times L$ sparse element matrix determined only by the gradients of the basis functions (i.e. $\nabla \phi_i$), $E = (E_1, E_2, \cdots, E_L)^T$ is the $L \times 1$ vector to be computed, and B is an $L \times 1$ vector determined by the given velocity field $\vec{\xi}$ and the gradients of the basis functions $\nabla \phi_i$. Because S_1 is independent of the input vector field, it can be constructed offline.

Once the $L \times 1$ vector E is determined by Eq. (3-15), it can be inversely re-organized back into the form given as Eq. (3-1a), such that E can be treated as a discrete surface. The curl-free field ∇E, can then be easily calculated.

3.1.3 Computing the divergence-free component

The divergence-free component $\nabla\times\vec{W}$ of the given field $\vec{\xi}$ is the projection onto the space of divergence-free fields. The distance between $\nabla\times\vec{W}$ and $\vec{\xi}$ can be expressed as:

$$G(\vec{W}) = \int_{\Omega} \| \nabla\times\vec{W} - \vec{\xi} \|^2 \, d\Omega \tag{3-16}$$

To find the optimal $\nabla\times\vec{W}$, the distance $G(\vec{W})$ in Eq. (3-16) needs to be minimized. Applying the necessary condition $\partial G/\partial\vec{W}_i = \vec{0}$, we obtain:

$$\forall i, \int_{\Omega} [\frac{\partial(\nabla\times\vec{W})}{\partial\vec{W}_i} \cdot (\nabla\times\vec{W} - \vec{\xi})] \, d\Omega = \vec{0} \tag{3-17}$$

Using Eq. (3-9b) and basic vector calculus, we have (see Appendix C):

$$\forall i, \int_{\Omega} [\nabla\phi_i \times (\nabla\times\vec{W} - \vec{\xi})] \, d\Omega = \vec{0} \tag{3-18}$$

or,

$$\forall i, \int_{\Omega} [\nabla\phi_i \times (\nabla\times\vec{W})] \, d\Omega = \int_{\Omega} (\nabla\phi_i \times \vec{\xi}) \, d\Omega \tag{3-19}$$

Eq. (3-19) can be approximated at each node as a simple sum over the neighbouring triangles:

$$\forall i, \sum_{T_k \in N(i)} [\nabla\phi_{ik} \times (\nabla\times\vec{W})_k] A_k = \sum_{T_k \in N(i)} (\nabla\phi_{ik} \times \vec{\xi}_k) A_k \tag{3-20}$$

For regular triangular grids, the area of each triangle, A_k, is a constant. Dividing both sides of Eq. (3-20) by A_k, we obtain:

$$\forall i, \sum_{T_k \in N(i)} [\nabla\phi_{ik} \times (\nabla\times\vec{W})_k] = \sum_{T_k \in N(i)} (\nabla\phi_{ik} \times \vec{\xi}_k) \tag{3-21}$$

In our particular case, as indicated by Eq. (3-8), each $\nabla\phi_{ik}$ (i.e., $\nabla\phi_i$ belonging to T_k) is essentially a 2-D vector, because the third component is zero. Meanwhile, because the input

$\vec{\xi}$ is a 2-D vector field, $\vec{\xi}_k$, which has been defined by Eq. (3-2), is actually a 2-D vector, and hence its third component is also zero. Thus, the right-hand side of Eq. (3-21) can be expressed as:

$$\forall i, \sum_{T_k \in N(i)} \nabla \phi_{ik} \times \vec{\xi}_k = \sum_{T_k \in N(i)} \begin{vmatrix} \vec{i} & \vec{j} & \vec{k} \\ (\nabla \phi_{ik})_x & (\nabla \phi_{ik})_y & 0 \\ \xi_{kx} & \xi_{ky} & 0 \end{vmatrix} = c_i \vec{k} \tag{3-22}$$

where c_i is a constant and can be calculated as:

$$c_i = \sum_{T_k \in N(i)} \begin{vmatrix} (\nabla \phi_{ik})_x & (\nabla \phi_{ik})_y \\ \xi_{kx} & \xi_{ky} \end{vmatrix} \tag{3-23}$$

Note that the right-hand side of Eq. (3-21) has the form of $(0,0,c_i)$. Using the right-hand rule of the $\nabla\times$ operator, $\vec{W}_i$, the i^{th} element of the vector $\vec{W}$ $(=(\vec{W}_1,\vec{W}_2,\cdots,\vec{W}_i,\cdots,\vec{W}_L)^T)$ must have the form of $(0,0,W_i)$, such that Eq. (3-21) can be correctly equated. In other words, the vector potential function $\vec{W}$ can be directly treated as a scalar function, denoted as $W=(W_1,W_2,\cdots,W_i,\cdots,W_L)^T$. We also note that each side of Eq. (3-21) has two zero components. Therefore, although Eq. (3-21) is a vector equation, it can also be considered as a scalar equation.

Expanding both sides of Eq. (3-21), we obtain a new linear equation (see Appendix D):

$$S_2 W = C \tag{3-24}$$

where S_2 is an $L\times L$ sparse element matrix, W is the $L\times 1$ vector to be calculated, $C=(-c_1,-c_2,\cdots,-c_i,\cdots,-c_L)^T$ is an $L\times 1$ vector, which can be computed using Eq. (3-23).

Once $W=(W_1,W_2,\cdots,W_i,\cdots,W_N)^T$ is obtained, $\forall i, \nabla\times\vec{W}_i$ can be easily calculated as follows:

$$\forall i, \nabla \times \vec{W}_i = \begin{vmatrix} \vec{i} & \vec{j} & \vec{k} \\ \partial/\partial x & \partial/\partial y & \partial/\partial z \\ 0 & 0 & W_i \end{vmatrix} = (\partial W_i/\partial y)\vec{i} - (\partial W_i/\partial x)\vec{j} = (\nabla W_i)^{\perp} \tag{3-25}$$

where $\perp$ is the orthogonal operator. Eq. (3-25) states that the divergence-free component of a 2-D input vector field $\vec{\xi}$ is equal to the co-gradient field of a scalar potential function W, which is determined by Eq. (3-24).

Eq. (3-25) also shows that, although $\nabla\times$ is a 3-D operator, the third component of $\nabla\times\vec{W}$ is zero, and hence $\nabla\times\vec{W}$ can be directly treated as a 2-D field. Based on this fact, in the later context, we use $(\nabla W)^{\perp}$ to replace $\nabla\times\vec{W}$.

3.1.4 Computing the harmonic remainder

As discussed above, a simplified 2-D DHHFD can be expressed as:

$$\vec{\xi} = \nabla E + (\nabla W)^{\perp} + \vec{R} \tag{3-26}$$

Note that all fields are 2-dimensional. The harmonic remainder, $\vec{R}$, can be easily solved by the relationship $\vec{R} = \vec{\xi} - \nabla E - (\nabla W)^{\perp}$.

3.2 Properties of the 2-D DHHFD

In Section 3.1, we have presented the theory of the 2-D DHHFD-RTG. We now discuss three important properties of this algorithm in the following.

Property-1: The element matrices S_1 and S_2 are determined by the gradients of the basis functions, and are independent of the input vector field.

When irregular grids are used, S_1 and S_2 are obtained by expanding the left-hand sides of Eqs. (3-13) and (3-20), respectively, and they are explicitly determined by the gradients of the piece-wise linear basis functions (i.e., $\nabla\phi_{ik}$) and the areas of the elements (i.e., A_k). If

regular grids are used, the matrices S_1 and S_2 can be obtained by expanding the left-hand sides of Eqs. (3-14) and (3-21), respectively, and they are determined only by the gradients of the piece-wise linear basis functions $\nabla\phi_{ik}$. As expressed in Eq. (3-8), each $\nabla\phi_{ik}$ is determined by an A_k and the coordinates of the corresponding triangle vertices. Note that $\nabla\phi_{ik}$, A_k and the coordinates of the triangle vertices depend on the adopted grids. Consequently, once the image domain Ω is triangulated, the two element matrices can be constructed independent of the input vector field.

Property-2: The two element matrices S_1 and S_2 are identical, i.e., $S_1 = S_2$.

It has been proved in Appendix D that in the case of using RTG, the two element matrices, S_1 and S_2, are identical to each other. We now prove that this relationship is also valid in the case of using ITG.

Mimicking the derivation of Eq. (D-1) presented in Appendix D, we can simplify the left-hand side of Eq. (3-20) as:

$$\forall i,\ \sum_{T_k \in N(i)} [\nabla\phi_{ik} \times (\nabla \times \vec{W})_k] A_k = -\vec{k} \sum_{T_k \in N(i)} [\nabla\phi_{ik} \cdot (\nabla W)_k] A_k \tag{3-27}$$

It can be easily observed that strong similarity exists between the left-hand side of Eq. (3-13) and the right-hand side of Eq. (3-27). Note that the left-hand side of Eq. (3-13) can be expressed as $S_1 E$, and hence the right-hand side of Eq. (3-27) can be also expressed as $\vec{k} S_2' W$, with $S_2' = -S_1$. Correspondingly, the right-hand side of Eq. (3-20) can be expressed as:

$$\forall i,\ \sum_{T_k \in N(i)} \nabla\phi_{ik} \times \vec{\xi}_k A_k = \sum_{T_k \in N(i)} \begin{vmatrix} \vec{i} & \vec{j} & \vec{k} \\ (\nabla\phi_{ik})_x & (\nabla\phi_{ik})_y & 0 \\ \xi_{kx} & \xi_{ky} & 0 \end{vmatrix} A_k = \vec{k} c_i \tag{3-28}$$

where

$$c_i = \sum_{T_k \in N(i)} \begin{vmatrix} (\nabla \phi_{ik})_x & (\nabla \phi_{ik})_y \\ \xi_{kx} & \xi_{ky} \end{vmatrix} A_k \tag{3-29}$$

Choosing $S_2 = -S_2'$, and equating Eqs. (3-27) and (3-28), we arrive at $S_2 W = C$ again. This formulation is consistent with Eq. (3-24). However, the $L \times 1$ vector $C = [-c_1, -c_2, \cdots, -c_i, \cdots - c_L]^T$ is determined by Eq. (3-29). Therefore, S_1 and S_2 are also identical when ITG is used. Same results can also be obtained using other type of grids (e.g., regular rectangular grids and irregular rectangular grids). In other words, independent of the type of the used grids, the two element matrices S_1 and S_2 are always equal to each other.

This property implies that we only need to construct one of the two element matrices, thus the computation speed can be improved.

Property-3: The rank of the two element matrices, S_1 and S_2, is $L-1$, where L is the total number of the vectors.

To prove this property, we first consider the simplest vector field with 3 vectors. The nodes and the only triangle are labelled as shown as Fig. 3-3.

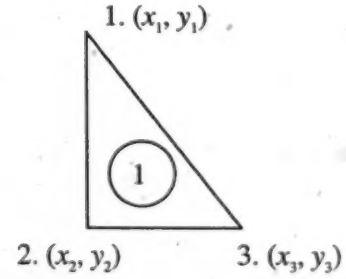

Figure 3-3. The simplest vector field with only 3 vectors.

It can be easily shown that

$$\forall i,\ \sum_{T_k \in N(i)} \nabla\phi_{ik} \cdot (\nabla E)_k A_k = A_1 \begin{bmatrix} \nabla\phi_{11}\cdot\nabla\phi_{11} & \nabla\phi_{11}\cdot\nabla\phi_{21} & \nabla\phi_{11}\cdot\nabla\phi_{31} \\ \nabla\phi_{21}\cdot\nabla\phi_{11} & \nabla\phi_{21}\cdot\nabla\phi_{21} & \nabla\phi_{21}\cdot\nabla\phi_{31} \\ \nabla\phi_{31}\cdot\nabla\phi_{11} & \nabla\phi_{31}\cdot\nabla\phi_{21} & \nabla\phi_{31}\cdot\nabla\phi_{31} \end{bmatrix} \begin{bmatrix} E_1 \\ E_2 \\ E_3 \end{bmatrix}$$

$$= \frac{1}{4A_1} \begin{bmatrix} s_{11} & s_{12} & s_{13} \\ s_{21} & s_{22} & s_{23} \\ s_{31} & s_{32} & s_{33} \end{bmatrix} \begin{bmatrix} E_1 \\ E_2 \\ E_3 \end{bmatrix} = \frac{1}{4A_1} S_1 E$$

where

$$s_{11} = (y_3 - y_2)(y_3 - y_2) + (x_2 - x_3)(x_2 - x_3)$$

$$s_{12} = (y_3 - y_2)(y_1 - y_3) + (x_2 - x_3)(x_3 - x_1)$$

$$s_{13} = (y_3 - y_2)(y_2 - y_1) + (x_2 - x_3)(x_1 - x_2)$$

$$s_{21} = (y_1 - y_3)(y_3 - y_2) + (x_3 - x_1)(x_2 - x_3)$$

$$s_{22} = (y_1 - y_3)(y_1 - y_3) + (x_3 - x_1)(x_3 - x_1)$$

$$s_{23} = (y_1 - y_3)(y_2 - y_1) + (x_3 - x_1)(x_1 - x_2)$$

$$s_{31} = (y_2 - y_1)(y_3 - y_2) + (x_1 - x_2)(x_2 - x_3)$$

$$s_{32} = (y_2 - y_1)(y_1 - y_3) + (x_1 - x_2)(x_3 - x_1)$$

$$s_{33} = (y_2 - y_1)(y_2 - y_1) + (x_1 - x_2)(x_1 - x_2)$$

Note that,

$$s_{31} = -(s_{11} + s_{21}),\ \ s_{32} = -(s_{12} + s_{22}),\ \ s_{33} = -(s_{13} + s_{23})$$

or

$$s_3 = -(s_1 + s_2) \tag{3-30}$$

where $s_1 = [s_{11}, s_{12}, s_{13}]$, $s_2 = [s_{21}, s_{22}, s_{23}]$, and $s_3 = [s_{31}, s_{32}, s_{33}]$ are the three row vectors of S_1. As seen in Eq. (3-30), s_3 can be expressed as a linear combination of s_1 and s_2. In other words, the rank of S_1 is 2.

This phenomenon can be explained using simple geometry. Let us investigate the degree-of-freedom (DOF) of the scalar potential function E built on an irregular triangular mesh. As shown as Fig. 3-4, the triangles $E_1E_2E_3$ and $E_1'E_2'E_3'$ define two piece-wise linear potential functions E and E', respectively, and $E' = E + D$ (where D is an arbitrary constant). Because $\nabla E = \nabla(E + D) = \nabla E'$, there exist a family of piece-wise linear potential functions E minimizing the distance $D(E)$ in Eq. (3-10). Therefore, the potential function E can shift along with the vertical axis. Therefore, the DOF of the potential function E is 1.

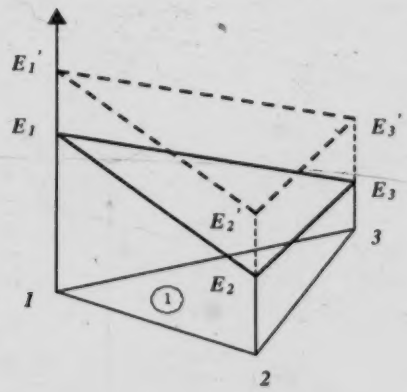

Figure 3-4. The DOF of the potential function built on a triangle.

Let us further consider the case that there are two irregular triangles, and correspondingly, four vectors, on the image domain Ω. In Fig. 3-5, the piece-wise linear potential function E is highlighted as $E_1E_2E_3E_4$. Based on above discussion, the DOF of the triangle $E_1E_2E_3$, as well as that of the triangle $E_1E_3E_4$, is also 1. Because the triangles $E_1E_2E_3$ and $E_1E_3E_4$ are constrained by the same edge E_1E_3, there is no relative movement between them. This constraint reduces the total DOF of the potential function E by 1. The total DOF of the potential function can be calculated by:

$$DOF(E) = DOF(E_1E_2E_3) + DOF(E_1E_3E_4) - 1 = 1 + 1 - 1 = 1$$

We can keep adding new triangular grids on the image domain Ω, and corresponding new

potential triangles, such that the above case can be extended to a vector field with arbitrary number of vectors. In this way, it can be easily shown that, no matter how many vectors are presented in the vector field, the DOF of the potential function E is always 1, and the whole potential surface can shift along the vertical axis. This fact proves that the rank of the element matrix is $L-1$, where L the total number of the vectors.

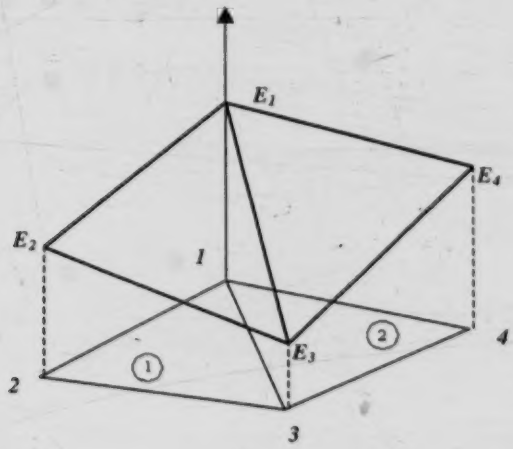

Figure 3-5. The DOF of the potential function built on two triangles.

The Property-1 commonly exists in all instances of FEM. It tells us that we can construct offline the element matrices, S_1 and S_2, without any prior knowledge about the input vector field. However, the Property-2 has not been reported by others. According to this property, we only need to construct one of the two element matrices, i.e., S_1 or S_2. The Property-3 has been implicitly exploited by Polthier et al. [48, 49], and Tong et al. [50]. To obtain unique decomposition of a given vector field, these researchers forced the potential values at the nodes on the boundary of the given vector field to be zeros. However, their methods implies that the rank of S_1 is significantly smaller than L. This conflicts with our derivation. The potential values of E_1 and W_1 are set to zeros, respectively, in our implementation, such that unique solutions to Eqs. (3-10) and (3-16) can be obtained.

3.3 Details of the proposed algorithm

In previous sections, we have presented the theory and three properties of the 2-D DHHFD. In this section, we present the details of the 2-D DHHFD-RTG algorithm. The flowchart of the algorithm is shown in Fig 3-6. The details corresponding to different sub-blocks are presented in the following subsections.

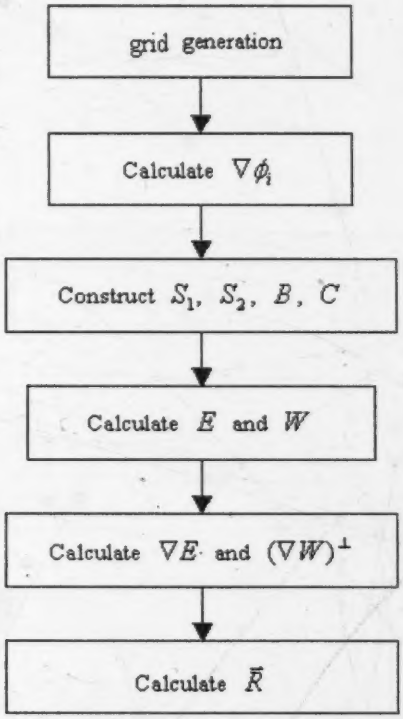

Figure 3-6. The flowchart of the 2-D DHHFD-RTG

3.3.1 Automatic generation of RTG

The RTG can be easily generated from the regular rectangular grids, which are often used in motion estimation algorithms. Let us first investigate the relationship between the nodes and the holes of the regular rectangular grids.

Fig. 3-7 shows a regular rectangular grid scheme. Several nodes and several rectangular holes are labelled by *italic* numbers and circled *italic* numbers, respectively. The i^{th} node

indicates the left-top corner of the rectangle r. It can be easily verified that the following relationship satisfies:

$$i = \left\lfloor \frac{r-1}{M-1} \right\rfloor * M + \mathrm{mod}(r-1, M-1) + 1 \qquad (3\text{-}31)$$

where $\lfloor n \rfloor$ is defined as the largest integer smaller than the real number n, and $\mathrm{mod}(m,n)$ is defined as $m - n * \lfloor m/n \rfloor$.

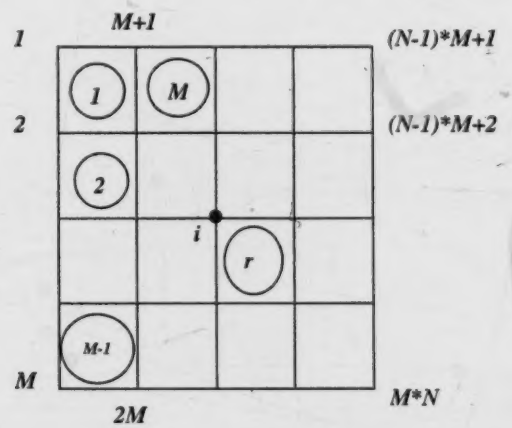

Figure 3-7. The relationship between nodes and holes of the regular rectangular grids.

If the rectangle r is divided into two triangles, as shown as Fig. 3-8, the vertices of the two newly generated triangles must be:

$(i,\ i+M+1,\ i+M)$ and $(i,\ i+1,\ i+M+1)$

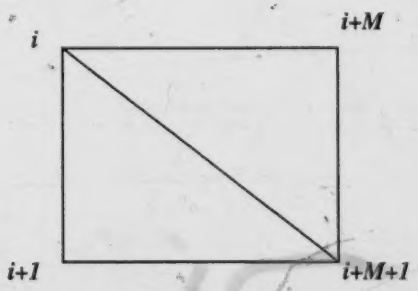

Figure 3-8. Two newly generated triangles and their vertices.

Note that the sequence of the vertices of each triangle must comply with the anticlockwise rule.

For a vector field with $M \times N$ vectors, there must be $(M-1)*(N-1)$ rectangular holes, and hence $2*(M-1)*(N-1)$ triangular holes. The nodal numbers keep unchanged.

The vertices of all newly generated triangular grids are stored in a Grid Table, and the nodal coordinates of the grids are stored in a Node Table. In the Grid Table, each row indicates the three vertices of a triangle. In the Node Table, each row gives the coordinates of a node in the image coordinate system. For a simple vector field with 3×3 vectors (see Fig. 3-13), the relationship between these two tables is shown in Fig. 3-9. The 9 nodes are denoted as (x_i, y_i), where $i \in [1, 9]$.

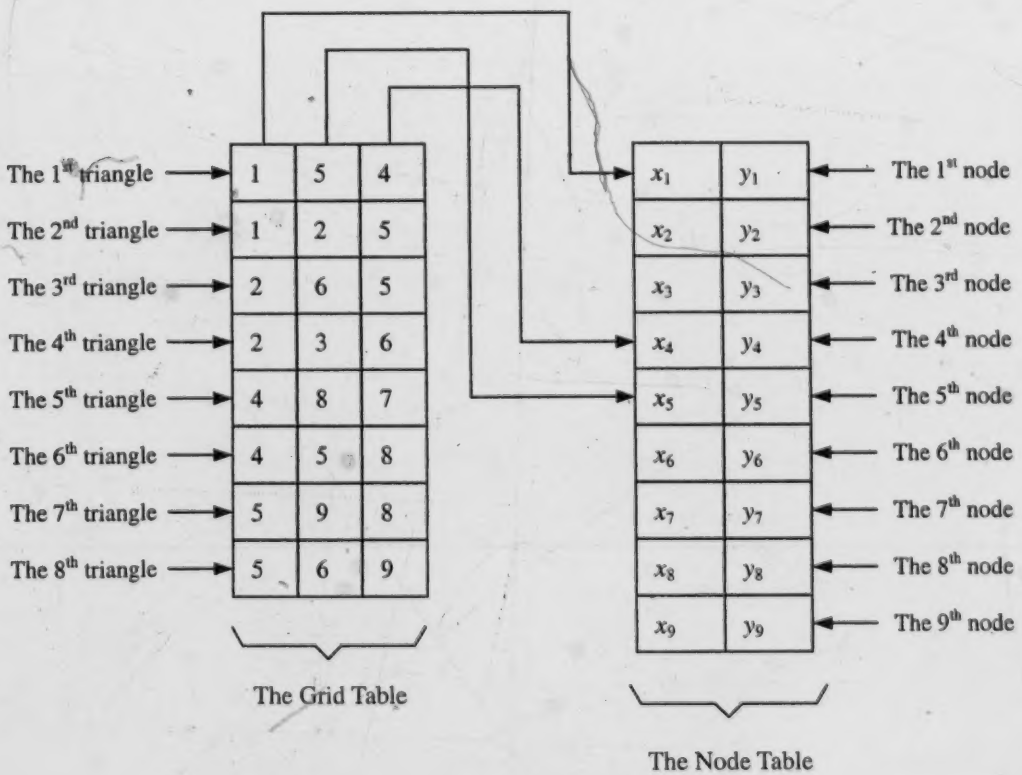

Figure 3-9. The relationship between the Grid Table and the Node Table.

3.3.2 Calculation of $\nabla\phi_i$

Based on the Grid Table and the Node Table, the gradients of the piece-wise linear basis functions $\nabla\phi_i$ can be easily calculated using Eq. (3-8). A Basis Gradient Table is also built to store the calculated $\nabla\phi_i$. The Basis Gradient Table is a 3-D table with a dimension of $TN\times 3\times 2$, where $TN = 2*(M-1)*(N-1)$ is the total number of the triangular holes. Fig. 3-10 shows the two-level structure of the Basis Gradient Table. Each level of the Basis Gradient Table corresponds to one component of the 2-D vector $\nabla\phi_i$ $(=[(\nabla\phi_i)_x,(\nabla\phi_i)_y])$. Tables 3-2a and 3-2b show the detailed mapping of the Basis Gradient Table for a vector field with $M\times N$ vectors. Table 3-2a maps $(\nabla\phi_i)_x$, and Table 3-2b maps $(\nabla\phi_i)_y$.

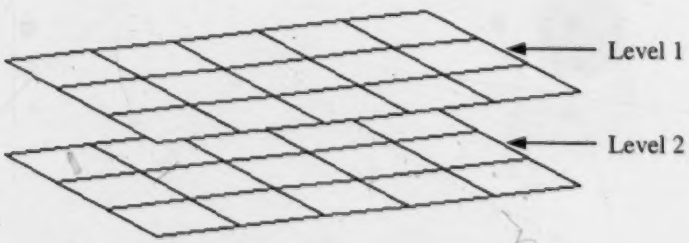

Figure 3-10. The two-level structure of the basis gradient table.

Each row of the Basis Gradient Table corresponds to a triangle. In the Basis Gradient Table, the subscripts i, a, and b in a row point to the three vertices of a corresponding triangle, and the same subscripts i, a, and b in different rows points to different vertices of different triangles. The Basis Gradient Table is the most important data source for the construction of the element matrices, S_1 and S_2, and the two vectors, B and C.

Table 3-2a. The first level of the Basis Gradient Table.

$(\nabla\phi_{i1})_x$	$(\nabla\phi_{a1})_x$	$(\nabla\phi_{b1})_x$
$(\nabla\phi_{i2})_x$	$(\nabla\phi_{a2})_x$	$(\nabla\phi_{b2})_x$
$(\nabla\phi_{i3})_x$	$(\nabla\phi_{a3})_x$	$(\nabla\phi_{b3})_x$
...	...	...
$(\nabla\phi_{i,TN})_x$	$(\nabla\phi_{a,TN})_x$	$(\nabla\phi_{b,TN})_x$

Table 3-2b. The second level of the Basis Gradient Table.

$(\nabla\phi_{i1})_y$	$(\nabla\phi_{a1})_y$	$(\nabla\phi_{b1})_y$
$(\nabla\phi_{i2})_y$	$(\nabla\phi_{a2})_y$	$(\nabla\phi_{b2})_y$
$(\nabla\phi_{i3})_y$	$(\nabla\phi_{a3})_y$	$(\nabla\phi_{b3})_y$
...	...	...
$(\nabla\phi_{i,TN})_y$	$(\nabla\phi_{a,TN})_y$	$(\nabla\phi_{b,TN})_y$

3.3.3 Construction of the element matrices S_1 and S_2

It can be easily observed that the element matrix S_1 (or S_2) contains L rows and L columns, and each row can be constructed by expanding the left-hand side of Eq. (3-14) around a node. The non-zero columns in an expanded row correspond to all the nodes belonging to the triangles in the set $N(i)$.

To understand this better, let us scrutinize the neighborhood of the 5th node in the vector field with 3×3 vectors as shown in Fig. 3-11. The set $N(5)$ contains 6 triangles, i.e. T_1, T_2, T_3, T_6, T_7, and T_8, and hence there are 7 nodes belonging to these triangles, i.e. nodes 1,

2, 4, 5, 6, 8, and 9. This implies that there must be 7 non-zero columns, i.e. columns 1, 2, 4, 5, 6, 8, and 9, in the 5th row of the element matrix S_1. Therefore, the 5th row of the element matrix corresponding to the vector field with 3×3 vectors must have the form of [s_{51}, s_{52}, 0, s_{54}, s_{55}, s_{56}, 0, s_{58}, s_{59}], where each s_{5j} with $j\in[1,2,4,5,6,8,9]$ represents a non-zero number.

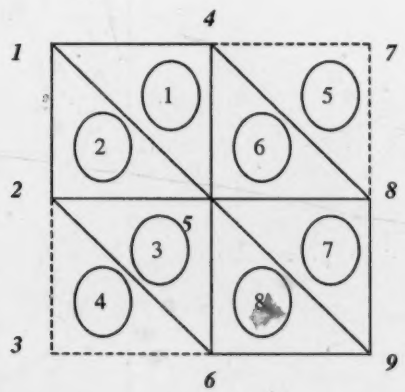

Figure 3-11. The neighborhood of the 5th node in a vector field with 3×3 vectors.

To automatically determine the non-zero numbers in the 5th row, let us look into Fig. 3-11 again. Note that the 1st node simultaneously belongs to triangles 1 and 2. From Appendix B, we know that $s_{51}=\nabla\phi_{51}\cdot\nabla\phi_{11}+\nabla\phi_{52}\cdot\nabla\phi_{12}=\sum_{T_k\in N(1)}\nabla\phi_{5k}\cdot\nabla\phi_{1k}$. Similarly, the 2nd node is also a neighboring node of node 5, and it simultaneously belongs to triangles 2 and 3. We have also known that $s_{52}=\nabla\phi_{52}\cdot\nabla\phi_{22}+\nabla\phi_{53}\cdot\nabla\phi_{23}=\sum_{T_k\in N(2)}\nabla\phi_{5k}\cdot\nabla\phi_{2k}$. Comparing the two expressions of s_{51} and s_{52}, we guess a general expression for all non-zero numbers in the element matrix S_1 as:

$$s_{ij}=\sum_{T_k\in N(j)}\nabla\phi_{ik}\cdot\nabla\phi_{jk} \tag{3-32}$$

where node i is the reference node, node j is a neighboring node of the node i, $N(j)$ is the set containing all triangles immediately adjacent to the node j.

The correctness of Eq. (3-32) can be easily verified by all non-zero numbers in the element matrix S_1 corresponding to the vector field as shown in Fig. 3-11. Eq. (3-32) results in an efficient algorithm for constructing the element matrix S_1. This algorithm is presented in Table 3-3 using pseudo code.

Table 3-3. The algorithm for constructing the element matrix S_1.

```
// Algorithm for construction of the element matrix S1
N(i) ⇐ All triangles containing the node i;
NN(i) ⇐ All nodes belonging to the triangles in N(i);
For each node j in NN(i) loop
    s_ij ⇐ 0;
    N(j) ⇐ All triangles containing the node j;
    For each triangle k in N(j) loop
        Fetch ∇φ_ik and ∇φ_jk in the basis gradient table;
        s_ij ⇐ s_ij + ∇φ_ik · ∇φ_jk;
    End loop;
End loop;
// End of the algorithm
```

3.3.4 Construction of vectors B and C

It has been discussed that the two vectors, B and C, are determined not only by the gradients of the piece-wise linear basis functions (i.e., $\nabla\phi_{ik}$), but also by the input vector field.

Before these two vectors are constructed, it is necessary to build an Average Vector Table to store $\vec{\xi}_k$, which is defined by Eq. (3-2). The Average Vector Table is a 2-D table with L rows and 2 columns as shown in Fig. 3-12. The two columns store the two non-zero components of the $\vec{\xi}_k (= (\xi_{kx}, \xi_{ky}))$, respectively, and each row corresponds to a triangle on the image domain Ω. The algorithm for constructing the vector B can be directly developed from the right-hand side of Eq. (3-14), i.e., $\forall i, b_i = \sum_{T_k \in N(i)} \nabla \phi_{ik} \cdot \vec{\xi}_k$. Table 3-4 gives the algorithm written in pseudo code.

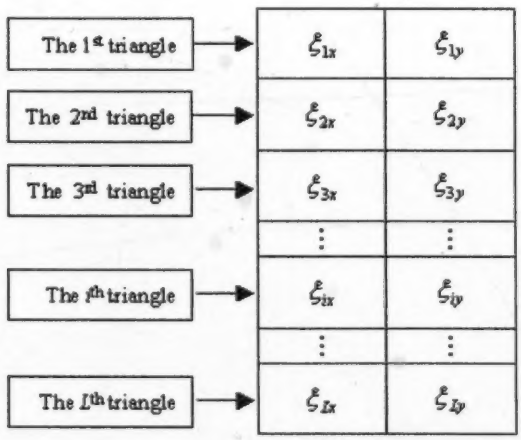

Figure 3-12. The mapping of the Average Vector Table.

The vector C can be easily constructed using the formula:

$$\forall i, c_i = -\sum_{T_k \in N(i)} [(\nabla \phi_{ik})_x \xi_{ky} - (\nabla \phi_{ik})_y \xi_{kx}]$$

The algorithm for constructing the vector C is shown in Table 3-5. Note that the algorithms for constructing the vectors B and C can be easily combined into one algorithm.

Table 3-4. The algorithm for constructing the vector B.

```
//Algorithm for construction of the vector B
N(i) ⇐ All triangles containing the node i;
b_i ⇐ 0;
For each triangle k in N(i) loop
    Fetch ∇φ_ik from the basis gradient table;
    Fetch ξ̄_k from the average vector table;
    b_i ⇐ b_i + ∇φ_ik · ξ̄_k;
End loop;
//End of algorithm
```

Table 3-5. The algorithm for constructing the vector C.

```
//Algorithm for construction of the vector C
N(i) ⇐ All triangles containing the node i;
c_i ⇐ 0;
For each triangle k in N(i) loop
    Fetch ∇φ_ik from the basis gradient table;
    Fetch ξ̄_k from the average vector table;
    c_i ⇐ c_i − [(∇φ_ik)_x ξ_ky − (∇φ_ik)_y ξ_kx];
End loop;
//End of algorithm
```

3.3.5 Calculation of E, ∇E, W, and $(\nabla W)^{\perp}$

Because the rank of S_1 is always equal to $L-1$, there are infinite potential functions, which are able to minimize $D(E)$ in Eq. (3-10). To obtain unique solution, E_1 is set to 0. Let S_r, E_r and B_r be an $(L-1)\times(L-1)$ matrix, two $(L-1)\times 1$ column vectors, and they are respectively defined as:

$$S_1 = \begin{bmatrix} s_{11} & X_1 \\ X_2 & S_r \end{bmatrix},\ E = \begin{bmatrix} E_1 \\ E_r \end{bmatrix}, \text{ and } B = \begin{bmatrix} b_1 \\ B_r \end{bmatrix} \tag{3-33}$$

where X_1 represents a $1\times(L-1)$ row vector, and X_2 is an $(L-1)\times 1$ column vector. It can be easily solved that $E_r = S_r^{-1}B_r$. Thus, using $E_1 = 0$, E can be expressed as:

$$E = \begin{bmatrix} 0 \\ E_r \end{bmatrix}$$

Re-organize E back into a $M \times N$ matrix, such that

$$E = \begin{bmatrix} 0 & E_{M+1} & \cdots & E_{(N-1)*M+1} \\ E_2 & E_{M+2} & \cdots & E_{(N-1)*M+2} \\ \cdots & \cdots & \cdots & \cdots \\ E_M & E_{2M} & \cdots & E_{M*N} \end{bmatrix}$$

Note that $L = M * N$. E can be visualized as a discrete surface, which is called curl-free potential surface in this thesis. ∇E can be calculated using a discrete gradient algorithm, e.g., the well known finite difference method.

In the same way, we also define a $(L-1)\times 1$ column vector C_r such that

$$C = \begin{bmatrix} c_1 \\ C_r \end{bmatrix} \tag{3-34}$$

and hence W can be expressed as:

$$W = \begin{bmatrix} 0 \\ W_r \end{bmatrix}$$

with $W_r = S_r^{-1} C_r$.

Once W has been calculated, it is also re-organized back into a 2-D matrix, i.e.,

$$W = \begin{bmatrix} 0 & W_{M+1} & \cdots & W_{(N-1)*M+1} \\ W_2 & W_{M+2} & \cdots & W_{(N-1)*M+2} \\ \cdots & \cdots & \cdots & \cdots \\ W_M & W_{2*M} & \cdots & W_{M*N} \end{bmatrix}$$

Correspondingly, $\nabla W = [(\nabla W)_x, (\nabla W)_y]$ can be also easily calculated, and $(\nabla W)^{\perp}$ can be expressed as $[(\nabla W)_y, -(\nabla W)_x]$.

As mentioned in Section 3.1, the harmonic remainder, $\vec{R}$, can be obtained with $\vec{R} = \vec{\xi} - (\nabla E) - (\nabla W)^{\perp}$. However, due to the denominator ($= \det(S_r)$) in S_r^{-1}, there often exists a scaling factor k between $(\nabla E) + (\nabla W)^{\perp}$ and $\vec{\xi}$. In this case, Eq. (3-26) is adjusted as:

$$\vec{\xi} = k(\nabla E) + k(\nabla W)^{\perp} + \vec{R} \tag{3-35}$$

hence,

$$\vec{R} = \vec{\xi} - k(\nabla E) - k(\nabla W)^{\perp}$$

with r being defined as:

$$k = \frac{\left\| \vec{\xi} \right\|_{\max}}{\left\| (\nabla E) + (\nabla W)^{\perp} \right\|_{\max}} \tag{3-36}$$

where $\|\cdot\|$ is the magnitude field of a vector field, and $\|\cdot\|_{\max}$ is the largest number in the magnitude field.

Theoretically, the field $\vec{R}$ should simultaneously satisfy $\nabla \cdot \vec{R} = 0$ and $\nabla \times \vec{R} = \vec{0}$. However, due to the computational errors, in practice, there often exist a few divergence components and a few rotational components in the field $\vec{R}$. To address this problem, we can further decompose the "harmonic" remainder $\vec{R}$ into three components such that more

accurate results can be obtained.

3.4 Computational complexity of 2-D DHHFD

In this section, we calculate the computational complexity (CC) of the proposed algorithm (i.e., 2-D DHHFD-RTG), and compare it with the 2-D DHHFD-ITG. Note that the CC of the 2-D DHHFD is mainly determined by the construction of the two element matrices, S_1 and S_2, the two vectors B and C, and the computation of the vectors E and W (see the flowchart shown in Fig. 3-6). In fact, the CC for computing the vectors E and W is fixed, provided that S_1 (or S_2), B and C are known. Therefore, we only need to investigate the CC of the construction of S_1 (or S_2), B and C in the two implementations. In the later text, we use CC_{S_1+RTG}, CC_{B+RTG}, and CC_{C+RTG} to denote the CC for constructing S_1, B, and C based on RTG, respectively. We also use CC_{S_1+ITG}, CC_{B+ITG}, and CC_{C+ITG} to denote the CC for constructing S_1, B, and C based on ITG, respectively. The improvement in the computational efficiency of the 2-D DHHFD-RTG over the 2-D DHHFD-ITG is then quantitatively evaluated.

3.4.1 Computational complexity of the 2-D DHHFD-RTG

In the case that RTG is used, the element matrix S_1 is constructed from the coefficients of the left-hand side of Eq. (3-14), the vector B is constructed from the right-hand side of Eq. (3-14), and the vector C is constructed from the right-hand side of Eq. (3-21). To easily investigate the CC of the construction of the matrix S_1 based on RTG, let us start from the simple case that a vector field with 3×3 vectors is decomposed. Fig. 3-13 shows the RTG in this case.

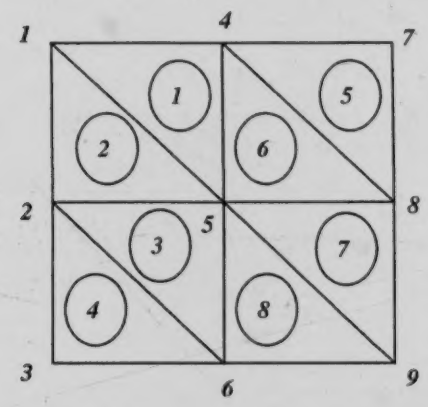

Figure 3-13. Decomposition of a vector field with 3×3 vectors based on RTG

It can be easily observed (see Appendix B) that each element of the matrix S_1 has different number of terms (NOT), depending on the topology of the grids. The NOT of all elements of the matrix S_1 can be mapped as a diagonal-symmetrical Term-Mapping Matrix (TMM):

$$\begin{bmatrix} 2 & 1 & 0 & 1 & 2 & 0 & 0 & 0 & 0 \\ 1 & 3 & 1 & 0 & 2 & 2 & 0 & 0 & 0 \\ 0 & 1 & 1 & 0 & 0 & 1 & 0 & 0 & 0 \\ 1 & 0 & 0 & 3 & 2 & 0 & 1 & 2 & 0 \\ 2 & 2 & 0 & 2 & 6 & 2 & 0 & 2 & 2 \\ 0 & 2 & 1 & 0 & 2 & 3 & 0 & 0 & 1 \\ 0 & 0 & 0 & 1 & 0 & 0 & 1 & 1 & 0 \\ 0 & 0 & 0 & 2 & 2 & 0 & 1 & 3 & 1 \\ 0 & 0 & 0 & 0 & 2 & 1 & 0 & 1 & 2 \end{bmatrix}$$

Either the 1st node or the 9th node belongs to 2 triangles, respectively, so they are grouped together, called class-2 nodes in this thesis. Each of the 3rd node and the 7th node belongs to 1 triangle, and they are called class-1 nodes. A class-3 node, i.e. the 2nd, 4th, 6th, or the 8th node, belongs to 3 triangles, respectively. The 5th node belongs to 6 triangles, and hence it is called a class-6 node. In the above TMM, the rows corresponding to the nodes in the same class contain

the same number of terms. For example, either row 1 or row 9 has 6 terms, either row 3 and row 7 has 3 terms, each row among rows 2, 4, 6, 8 has 9 terms, and row 5 has 18 terms.

We also note that each term in s_{ij} (an element of the matrix S_1) only contains a "dot production", which is equal to 2 multiplications and 1 addition (see Eq. (B-1) in Appendix B), and in each element of S_1, there are totally $2*NOT$ multiplications and $2*NOT-1$ additions. Therefore, in the above TMM, either row 1 or row 9 has 6*2=12 multiplications and (2*2-1)+(2*1-1)+(2*1-1)+(2*2-1)=8 additions. Likewise, either row 3 or row 7 has 3*2=6 multiplications and (2*1-1)+(2*1-1)+(2*1-1)=3 additions, each row among rows 2, 4, 6, and 8 has 9*2=18 multiplications and 13 additions. Row 5 has 18*2=36 multiplications and 29 additions. This rule can be summarized in Table 3-6.

Table 3-6. CC_{S_1+RTG} for decomposing a vector field with 3×3 vectors.

Class of nodes	Number of rows	Multiplications	Additions
2	2	12*2=24	8*2=16
1	2	6*2=12	3*2=6
3	4	18*4=72	13*4=52
6	1	36*1=36	29*1=29
TOTAL	9	144	103

Similarly, it can be shown that the vector B contains 2*2=4 multiplications and 3 additions for a class-2 node, 2 multiplications and 1 addition for a class-1 node, 6 multiplications and 2*3-1=5 additions for a class-3 node, and 2*6=12 multiplications and 2*6-1=11 additions for a class-6 node, respectively. This rule is summarized in Table 3-7.

The vector C contains 2*2=4 multiplications and 3 subtractions for a class-2 node, 2 multiplications and 1 subtraction for a class-1 node, 6 multiplications and 2*3-1=5 subtractions for a class-3 node, and 2*6=12 multiplications and 2*6-1=11 subtractions for a class-6 node, respectively. According to the point of view of binary computation, the subtraction is equivalent

to the addition. Hence, we can obtain a computational rule for constructing vector C identical to Table 3-7.

Table 3-7. CC_{B+RTG} or CC_{C+RTG} for decomposing a vector field with 3×3 vectors.

Class of nodes	Number of rows	Multiplications	Additions
2	2	4*2=8	3*2=16
1	2	2*2=4	1*2=2
3	4	6*4=24	5*4=20
6	1	12*1=12	11*1=11
TOTAL	9	48	49

We now extend the above computational rules to the case that a vector field with $M\times N$ vectors is decomposed. The first node and the last node on the image domain Ω are class-2 nodes, the other two corners are class-1 nodes, all nodes on the boundary except for the four corners are class-3 nodes, and all other nodes are class-6 nodes. Correspondingly, the CC for constructing the full matrix S_1, i.e. CC_{S_1+RTG}, can be summarized as Table 3-8.

Table 3-8. CC_{S_1+RTG} for decomposing a vector field with $M\times N$ vectors.

Class of nodes	Number of rows	Multiplications	Additions
2	2	12*2=24	8*2=16
1	2	6*2=12	3*2=6
3	2*(M+N-4)	36*(M+N-4)	26*(M+N-4)
6	(M-2)*(N-2)	36*(M-2)*(N-2)	29*(M-2)*(N-2)
TOTAL	**M*N**	**36*(M-1)*(N-1)**	**29*M*N-32*M-32*N+34**

The construction of a full vector B and the construction of a full vector C have the same CC, and they are simultaneously summarized as table 3-9.

Table 3-9. CC_{B+RTG} or CC_{C+RTG} for decomposing a vector field with $M \times N$ vectors.

Class of nodes	Number of rows	Multiplications	Additions
2	2	4*2=8	3*2=16
1	2	2*2=4	1*2=2
3	2*(M+N-4)	12*(M+N-4)	10*(M+N-4)
6	(M-2)*(N-2)	12*(M-2)*(N-2)	11*(M-2)*(N-2)
TOTAL	**M*N**	**12*(M-1)*(N-1)**	**11*M*N-12*M-12*N+22**

Thus, to construct the element matrix S_1 and two vectors B and C, the total computational complexity is $CC_{RTG} = CC_{S_1+RTG} + CC_{B+RTG} + CC_{C+RTG}$, which is summarized in Table 3-10.

Table 3-10. CC_{RTG} for decomposing a vector field with $M \times N$ vectors.

Number of multiplications	$60*(M-1)*(N-1)$
Number of additions	$51*M*N-56*M-56*N+78$

3.4.2 Computational complexity of the 2-D DHHFD-ITG

Let us assume that a vector field with $M \times N$ vectors is decomposed based on ITG. To be convenient for comparison, we use the same topological structure as the RTG. As an example, Fig. 3-14 shows the topological structure of the ITG used for decomposing a small vector field with 9 vectors. Note that the topological structure is exactly identical to that shown in Fig. 3-13. It can be easily shown that different topological structures may have different TMM, but the entire CC is fixed for decomposing a particular vector field based on ITG.

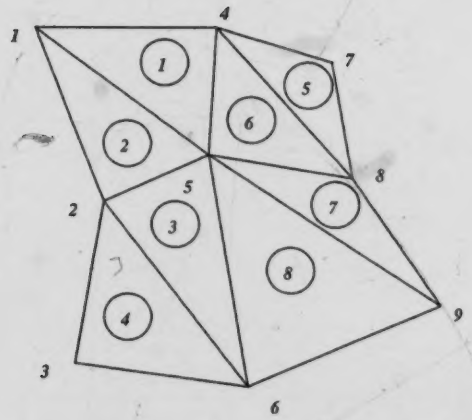

Figure 3-14. Decomposition of a small vector field with 9 vectors using ITG

In this case, the linear equations, $S_1 E = B$ and $S_2 W = C$, are derived from Eqs. (3-13) and (3-20), respectively. Each term in s_{ij} contains the area of the corresponding triangle, so there are 3 multiplications and 1 addition in each term of s_{ij}. Based on this recognition, when ITG is used, the CC for constructing S_1 can be summarized as Table 3-11.

Table 3-11. CC_{S_1+ITG} for decomposing a vector field with $M \times N$ vectors.

Class of nodes	Number of rows	Multiplications	Additions
2	2	18*2=24	8*2=16
1	2	9*2=12	3*2=6
3	2*(M+N-4)	54*(M+N-4)	26*(M+N-4)
6	(M-2)*(N-2)	54*(M-2)*(N-2)	29*(M-2)*(N-2)
TOTAL	**M*N**	**54*(M-1)*(N-1)**	**29*M*N-32*M-32*N+34**

In this situation, the CC for constructing B or C can be summarized in Table 3-12.

Table 3-12. CC_{B+ITG} or CC_{C+ITM} for decomposing a vector field with $M \times N$ vectors.

Class of nodes	Number of rows	Multiplications	Additions
2	2	6*2=12	3*2=16
1	2	3*2=6	1*2=2
3	2*(M+N-4)	18*(M+N-4)	10*(M+N-4)
6	(M-2)*(N-2)	18*(M-2)*(N-2)	11*(M-2)*(N-2)
TOTAL	**M*N**	**18*(M-1)*(N-1)**	**11*M*N-12*M-12*N+22**

Because the areas of all triangles may be different, we need compute the areas of all triangles. According to Eq. (3-7), a triangular area can be computed by two multiplications and 1 addition. Note that in the level of binary computation, the subtraction is equivalent to the addition. Furthermore, because the division by 2 is equivalent to a right-shift-by-1-bit machine instruction, which is usually extremely fast, the CC of the division by 2 is ignored. For decomposing a vector field with $M \times N$ vectors, $2*(M-1)*(N-1)$ triangles are needed to triangulate the image domain Ω. Therefore, the CC for calculating the areas of all these triangles, denoted as CC_A, is $4*(M-1)*(N-1)$ multiplications and $2*(M-1)*(N-1)$ additions.

Without knowing the property-2 of the 2-D DHHFD (i.e., $S_1 = S_2$), S_2 will also have to be constructed. The CC for constructing S_2 is identical to that for constructing S_1. In this case, the entire CC for constructing S_1, S_2, B and C, denoted as CC_{ITG}, is equal to $CC_{S_1+ITG} + CC_{S_2+ITG} + CC_{B+ITG} + CC_{C+ITG} + CC_A$. Table 3-13 presents CC_{ITG}.

With knowing $S_1 = S_2$, the construction of S_2 can be ignored. In this case, the total CC for constructing S_1, S_2, B and C, denoted as CC'_{ITG}, is equal to $CC_{S_1+ITG} + CC_{B+ITG} + CC_{C+ITG} + CC_A$. Table 3-14 presents CC'_{ITG}.

Table 3-13. CC_{ITM} for decomposing a vector field with $M \times N$ vectors.

Number of multiplications	$148*(M-1)*(N-1)$
Number of additions	$82*M*N-90*M-90*N+112$

Table 3-14. CC'_{ITG} for decomposing a vector field with $M \times N$ vectors.

Number of multiplications	$94*(M-1)*(N-1)$
Number of additions	$53*M*N-58*M-58*N+78$

3.4.3 Comparison of CC of the Two Implementations

The CC of the 2-D DHHFD-RTG and the 2-D DHHFD-ITG is compared in Table 3-15. Because the property-2 (i.e., $S_1 = S_2$) has not been reported, we only focus on the comparison between CC_{ITG} and CC_{RTG}.

Table 3-15. Comparison of the CC of the two implementations.

Algorithms	Number of multiplications	Number of additions
2-D DHHFD-ITG	$148*(M-1)*(N-1)$	$82*M*N-90*M-90*N+112$
2-D DHHFD-RTG	$60*(M-1)*(N-1)$	$51*M*N-56*M-56*N+78$

The entire CC of each implementation should include the inversion of the matrix S_r and the multiplications of S_r^{-1} by vectors B and C, respectively. Our practices prove that these steps are so fast that they can be ignored in computational analysis. Therefore, the CC of each of the two algorithms can be roughly represented by the construction of S_1 (or S_2), B, and C. Numerous simulations have also proved that the proposed algorithm (i.e., 2-D DHHFD-RTG)

can save nearly 60% computational time, compared to the 2-D DHHFD-ITG if without knowing $S_1 = S_2$.

Assume that the CC of the 2-D DHHFD is mainly determined by the multiplications, the improvement of computational efficiency of the 2-D DHHFD-RTG over the 2-D DHHFD-ITG can be theoretically calculated as:

$$ratio = \frac{CC_{ITG} - CC_{RTG}}{CC_{ITG}} \approx \frac{88*(M-1)*(N-1)}{148*(M-1)*(N-1)} = \frac{88}{148} = 0.5946 = 59.46\%$$

where the "ratio" represents the improvement of computational efficiency.

It should be pointed out that we implement the 2-D DHHFD-RTG using Matlab programming language. If another professional programming language, such as C/C++, is used, the construction of S_1, B, and C will be very fast. In this case, the computational time of inversion of S_r, and the multiplications of S_r by B_r and C_r may not be ignored. Thus, the improvement of computational efficiency may be much less than the theoretical limit (i.e., 60%).

3.5 Performance evaluation

To guarantee the correctness of the proposed algorithm, a synthetic vector field is decomposed. This experiment is presented here in details such that the overall flowchart of the algorithm (shown in Fig. 3-6) can be better understood.

We first create a potential function $z = xe^{-x^2-y^2}$, which is graphically shown in Fig. 3-15a. The gradient of z, i.e. ∇z, is a curl-free field shown as Fig. 15b. The co-gradient of z, $(\nabla z)^{\perp}$, is a divergence-free field shown as Fig. 15c. A complex field $\vec{\xi}$, shown as Fig. 15d, is generated by adding the two synthetic fields ∇z and $(\nabla z)^{\perp}$, i.e., $\vec{\xi} = \nabla z + (\nabla z)^{\perp}$. In this experiment, there are 21×21 motion vectors in the motion field, so $L = 21*21 = 441$.

The goal is to extract the curl-free component field ∇E and the divergence-free field

$(\nabla W)^{\perp}$ from the synthetic complex field $\vec{\xi}$, and then compare them with the synthetic curl-free field, ∇z, and the synthetic divergence-free field $(\nabla z)^{\perp}$, respectively.

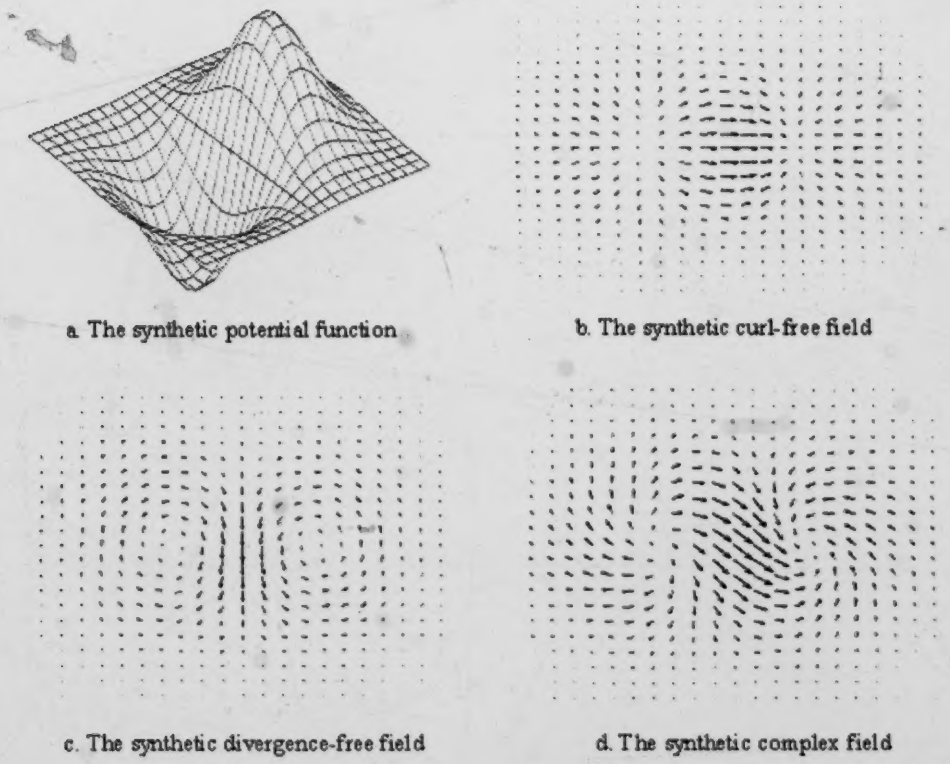

a. The synthetic potential function

b. The synthetic curl-free field

c. The synthetic divergence-free field

d. The synthetic complex field

Figure 3-15. Generation of a synthetic complex field.

Step 1: Construct the 441×441 element matrix S_1, the 441×1 vectors B, and C. Hence, by using Eqs. (3-33) and (3-34), the 440×440 matrix S_r, and the 440×1 vectors B_r and C_r can easily be generated. Thus, S_r^{-1} can be calculated.

Step 2: Calculate the 440×1 vectors E_r and W_r using $E_r = S_r^{-1}B$ and $W_r = S_r^{-1}C$, respectively.

Step 3: Form the two 441×1 vectors E and W using $E = \begin{bmatrix} 0 \\ E_r \end{bmatrix}$ and $W = \begin{bmatrix} 0 \\ W_r \end{bmatrix}$,

respectively. Re-organize them back to two 21×21 matrices, i.e.,

$$E=\begin{bmatrix} 0 & E_{22} & \cdots & E_{421} \\ E_2 & E_{23} & \cdots & E_{422} \\ \cdots & \cdots & \cdots & \cdots \\ E_{21} & E_{42} & \cdots & E_{441} \end{bmatrix} \text{ and } W=\begin{bmatrix} 0 & W_{22} & \cdots & W_{421} \\ W_2 & W_{23} & \cdots & W_{422} \\ \cdots & \cdots & \cdots & \cdots \\ W_{21} & W_{42} & \cdots & W_{441} \end{bmatrix}.$$

These two potential matrices are graphically presented in Figs. 3-16a and 3-16b.

Step 4: Calculate ∇E and ∇W. Convert ∇W into $(\nabla W)^{\perp}$ using $(\nabla W)^{\perp}=[(\nabla W)_y,-(\nabla W)_x]$. Compute $\vec{\xi}'=(\nabla E)+(\nabla W)^{\perp}$. ∇E, $(\nabla W)^{\perp}$, and $\vec{\xi}'$ are shown in Figs. 3-16c, 3-16d, and 3-16e, respectively.

Step 5: Compute the scaling factor k using

$$k=\frac{\|\vec{\xi}\|_{\max}}{\|\vec{\xi}'\|_{\max}}.$$

In this experiment, $k=5.3685$.

Step 6: Obtain the harmonic remainder $\vec{R}$ using $\vec{R}=\vec{\xi}-k(\nabla E)-k(\nabla W)^{\perp}=\vec{\xi}-k\vec{\xi}'$. The obtained harmonic remainder is shown as Fig. 3-16f.

It can be observed that the recovered potential functions E and W (shown as Figs. 3-16a and 3-16b) have almost the same shapes as the given potential function z (shown as Fig. 3-15a). However, compared to the potential function z, the potential functions E and W have been automatically scaled by $1/k$ due to the denominator in the S_r^{-1}. Fortunately, the locations of extrema do not shift. This guarantees the specified critical points (i.e., sources, sinks, and rotational centers) in the component fields are consistent with the ground truth.

When magnified by the scaling factor k, the recovered curl-free field ∇E, divergence-free field $(\nabla W)^{\perp}$, and the complex field $\vec{\xi}'$ (shown as Figs. 3-16c, 3-16d, and 3-16e, respectively) are almost identical to the synthetic curl-free field ∇z, the synthetic divergence-free field $(\nabla z)^{\perp}$, and the synthetic complex field $\vec{\xi}$ (shown as Figs. 3-15b, 3-15c,

and 3-15d, respectively). This proves the correctness of the proposed 2-D DHHFD-RTG algorithm.

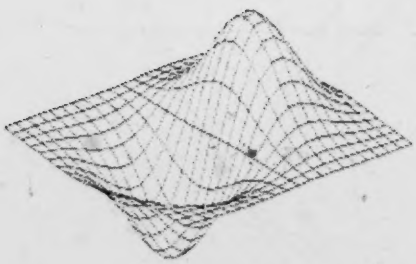

a. Recovered potential function E

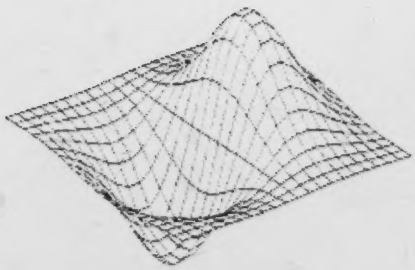

b. Recovered potential function W

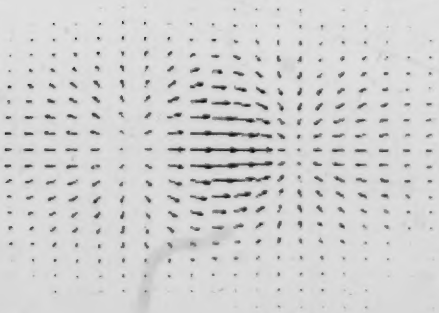

c. Recovered curl-free field ∇E

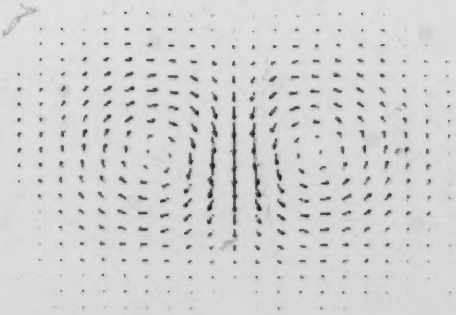

d. Recovered divergence-free field $(\nabla W)^{\perp}$

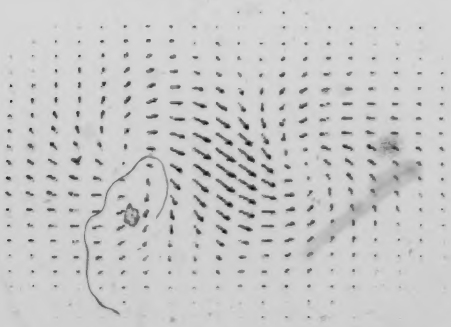

e. Recovered complex field . $\vec{\xi}$

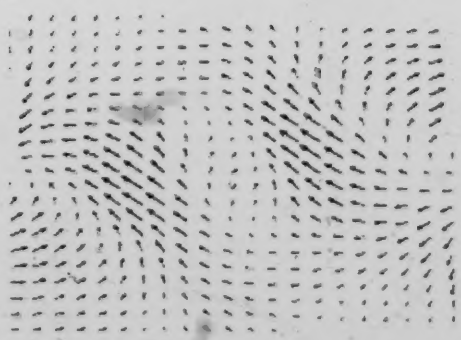

f. Harmonic remainder $\vec{R}$

Figure 3-16. Decomposition of a synthetic complex field.

Note that the synthetic complex field $\vec{\xi}$ does not contain any harmonic term, and hence the resulting $\vec{R}$ should be zero. However, because of computational errors, we obtained a nonzero $\vec{R}$ with very small magnitude. Fig. 3-16f has been magnified by 30 times.

3.6 Summary

In this chapter, a simplified implementation of 2-D DHHFD is demonstrated in details. We first re-derive the 2-D DHHFD based on RTG, such that the proposed implementation can be directly applied to analyze the motion field extracted from two consecutive image frames. Next, three important properties of the 2-D DHHFD are presented. We then expose all details of the implementation, including several crucial data structures and algorithms. Afterwards, the computational complexity of two implementations of the 2-D DHHFD is analyzed, and the improvement of computational efficiency of the proposed algorithm over the implementation based on ITG is quantitatively evaluated. Finally, to verify the correctness of the proposed algorithm (i.e., the 2-D DHHFD-RTG), a synthetic complex motion field is decomposed. The results of this experiment show that the proposed algorithm can be efficiently applied for video analysis.

Chapter 4

Cardiac Video Analysis

In Chapter 3, we have presented the theory and the implementation details of the 2-D DHHFD-RTG. In this chapter, we apply this algorithm to analyze the cardiac electrical patterns. Section 4.1 presents the flowchart of the overall techniques used for cardiac video analysis. Section 4.2 presents the performance of the anisotropic diffusion equation. Section 4.3 presents the performance of the OFCE-based motion estimation algorithm. The performance of the motion decomposition technique is evaluated in Section 4.4. Experimental evaluations are presented in Section 4.5. Finally, the detection of critical points is presented in Section 4.6.

4.1 The flowchart of the overall framework

Using the optical mapping method, a large amount of cardiac video data has been acquired. Fig. 4-1 shows 4 cardiac videos that are briefly described in Table 4-1. The images a(•), b(•), c(•) and d(•) belong to video-1, video-2, video-3, and video-4, respectively. These four videos will be analyzed and compared in order to understand the conduction properties of the heart tissue and the mechanisms of the ventricular tachyarrhythmias.

The cardiac electrical patterns are morphologically similar to cloud, water, or forest fire. Hence the evolution of the cardiac electrical activity is similar to the fluid motion activitly [62]. Consequently, techniques for fluid motion analysis may be helpful for analyzing the turbulent propagation of the cardiac electrical signals.

In this chapter, we present a novel framework to analyze the cardiac electrical patterns using the proposed 2-D DHHFD-RTG. Fig. 4-2 shows the flowchart of the overall framework. All sub-blocks are detailed in the following sections.

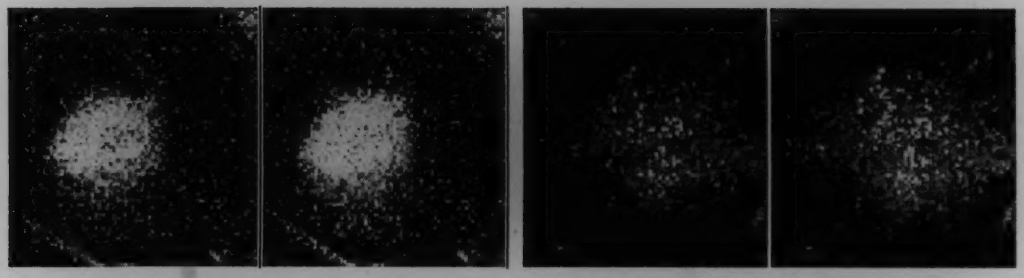

a(i) Frame-19 of video-1 | a(ii) Frame-20 of video-1 | b(i) Frame-54 of video-2 | b(ii) Frame-55 of video-2

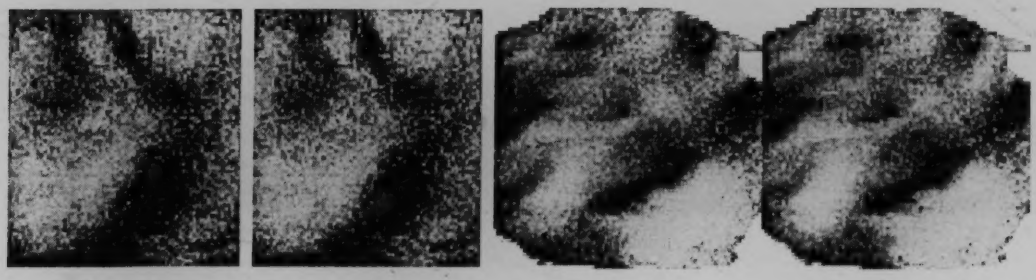

c(i) Frame-170 of video-3 | c(ii) Frame-171 of video-3 | d(i) Frame-370 of video-4 | d(ii) Frame-371 of video-4

Figure 4-1. Image frames sampled from 4 cardiac videos.

Table 4-1. Brief description of the four videos.

	Video 1	**Video 2**	**Video 3**	**Video 4**
Subjects	Left ventricle of an isolated mouse heart	Left ventricle of an isolated rat heart	Left ventricle of an isolated pig heart	Left ventricle of an isolated pig heart
Signals	Pacing	Pacing	VF	Shock failure of VF
Video length (frames)	999	2733	999	2303
Frame rate (fps)	Unknown	1029	838	2667
Image size (pixels)	157×146	157×145	150×132	157×159
Targeted area (cm^2)	Unknown	0.8×0.78	5×5	5×5
Motion artifacts	No	Yes	No	No

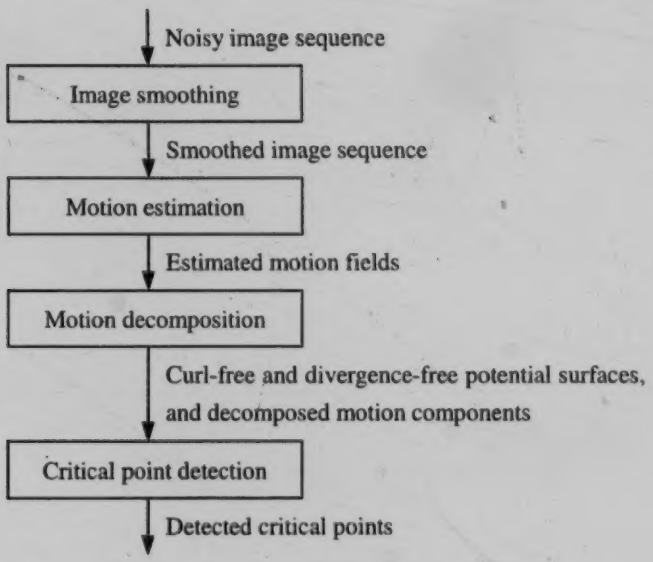

Figure 4-2. Flowchart of the overall framework.

4.2 Image smoothing

It is observed in Fig. 4-1 that the cardiac videos are generally very noisy. Hence, these cardiac videos must be de-noised before further processing. In Section 2.4, several image smoothing techniques have been presented. In this thesis, we use the anisotropic diffusion equation (Eq. (2-7)) to smooth the noisy cardiac image sequences.

The anisotropic diffusion equation has been used to smooth the noisy cardiac videos presented in Fig. 4-1. Table 4-2 presents the parameters in our experiments. Note that we use $c_2(x, y, s)$ (Eq. (2-6b)) as the diffusion function. The cardiac electrical patterns, rather than their boundaries, are our primary targets of interest. For the four test videos, the iteration numbers of the anisotropic diffusion equation are 65, 45, 50, and 65, respectively. Fig. 4-3 shows the smoothed counterparts of the image frames shown in Fig. 4-1.

Table 4-2. The parameters of the discretized anisotropic diffusion equation.

K	λ	Diffusion function
25	0.2	$c_2(x,y,s)=\left[1+\frac{1}{K^2}\|\nabla I(x,y,s)\|^2\right]^{-1}$

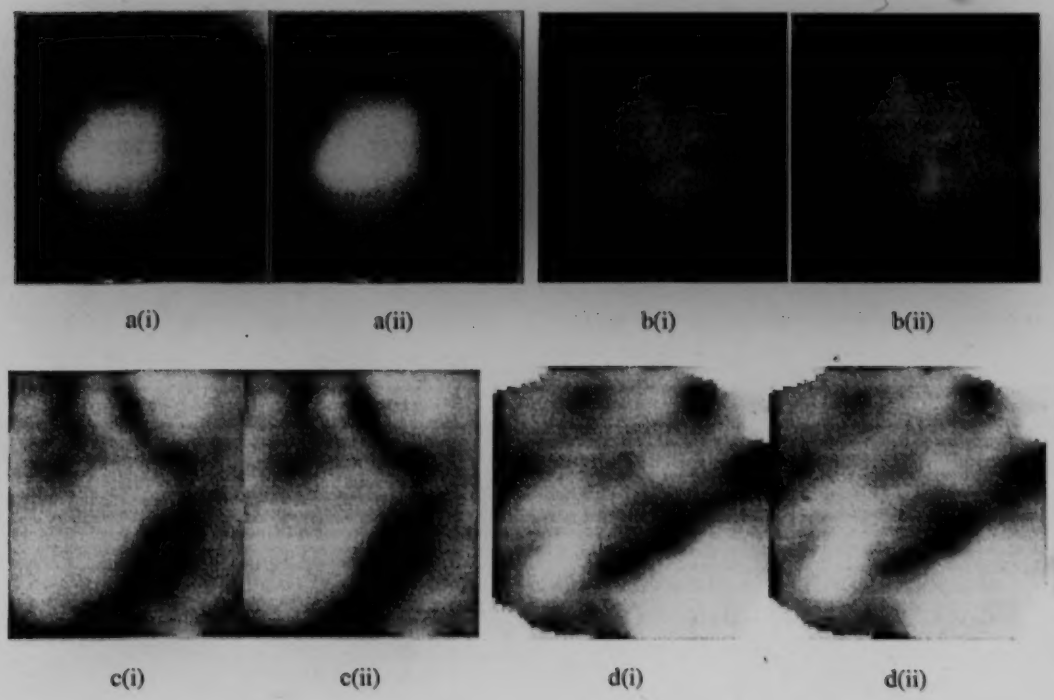

Figure 4-3. Smoothed image frames obtained using the anisotropic diffusion equation. The original noisy images are shown in Fig. 4-1.

To compare the performance of the anisotropic diffusion equation, we have also smoothed the four image sequences using three cascaded Gaussian lowpass filters. The standard deviations of the three Gaussian filters are 4, 5, and 7, respectively. Fig. 4-4 shows the results of the cascaded Gaussian lowpass filters.

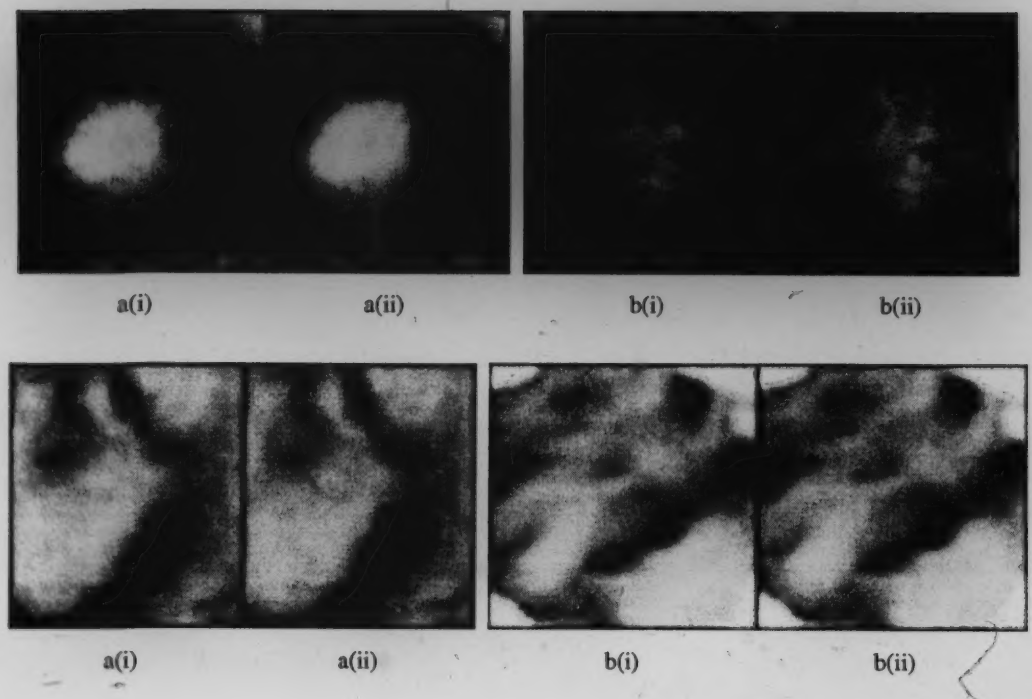

Figure 4-4. Smoothed image frames obtained using three cascaded Gaussian lowpass filters. The original noisy images are shown in Fig. 4-1.

Comparing Fig. 4-3 and Fig. 4-4, it can be inferred that the anisotropic diffusion equation provides a better performance. The ansiotropic diffusion equation not only filters out the strong noise and dilutes the heterogeneities in the images, but also enhances the boundaries of the pattern regions.

4.3 Motion estimation

According to the classification proposed by Kambhamettu et al. [62], there are eight categories of motion: rigid motion, articulated motion, quasi-rigid motion, isometric motion, homothetic motion, conformal motion, elastic motion, and fluid motion. This classification is very important for accurate motion estimation because each class of motion has its own particular physical constraints. For instance, the fluid dynamics constraints have been applied to

cloud motion field recovery from image sequence [63 - 66]. Unfortunately, as the true mechanisms behind the cardiac tachyarrhythmias are not yet known completely, it is very difficult to develop a physical model for the motion estimation of the cardiac electrical events.

Although the cardiac electrical patterns are morphologically similar to cloud, the motion estimation techniques for cloud images cannot be directly applied to extract the conduction velocity field as the true mechanisms of the cardiac electrical signals are very different from cloud. Schunk [68] and Nagel [67] argued that for fluid motion, the motion field should be closely related to the density change of the targeted object. According to their perspectives, the brightness of the cloud image should exponentially change with the divergence of the cloud. Bereziat et al. [66] presented a physical interpretation of this property of the cloud image with the assumption of total brightness preservation. However, the density of the heart cells is believed not to change dramatically over time, and hence the brightness variation of the cardiac electrical patterns is independent of the density of the heart tissue. As mentioned in Section 2.1, the neighboring heart cells are excited almost in the same way. The transmembrane action potentials of all heart cells roughly comply with the "all-or-nothing" property. Consequently, the brightness variation of a pixel in the cardiac data is approximately the same as that of a neighboring pixel. This implies that the total brightness of the cardiac electrical patterns do not preserve since the number of the excited heart cells keeps changing.

The similarity between two consecutive image frames in the cardiac videos can be quantitatively evaluated using the cross-correlation coefficient (CCC) between two patterns. The peak cross-correlation coefficient between two patterns is defined as:

$$\alpha = \frac{\sum_x \sum_y \left\{ [I_1(x,y) - \mu_1] \cdot [I_2(x,y) - \mu_2] \right\}}{\sqrt{\sum_x \sum_y [I_1(x,y) - \mu_1]^2} \sqrt{\sum_x \sum_y [I_2(x,y) - \mu_2]^2}} \qquad (4\text{-}1)$$

where α is the cross-correlation coefficient, $I_1(x,y)$ and $I_2(x,y)$ are the two images, (x,y) is a spatial location, and μ_1 and μ_2 are the mean values of the two images.

The CCC corresponding to the four image pairs shown in Fig. 4-3 are presented in Table 4-3. Note that the similarity between the consecutive image frames is very high.

Table 4-3. CCC between the four image pairs shown in Fig. 4-3.

Image pairs	a(i) and a(ii)	b(i) and b(ii)	c(i) and c(ii)	d(i) and d(ii)
CCC	0.9931	0.9930	0.9955	0.9939

In extreme cases, e.g. in some VF videos, the CCC between two consecutive images may be very small. This violation of the similarity is resulted from the strong motion discontinuities in the VF videos. Before a mature theory of VF mechanisms is completely verified, we have to make some approximation. In this thesis, we assume that the spatial smoothness constraint is roughly satisfied for all cardiac electrical patterns.

Two properties of the cardiac electrical patterns can be summarized as follows. First, the brightness variation of a single pixel is independent of the density of the heart tissue, and the total brightness of the cardiac electrical patterns does not preserve. Secondly, a high similarity exists between two consecutive image frames, and hence the image motion is relatively slow. As a result, in most pixel locations, the spatial smoothness of the motion vectors preserves, and the temporal smoothness is always satisfied.

Based on the two properties of the cardiac electrical patterns, we use the OFCE-based motion estimation algorithm to extract the motion fields of the cardiac electrical patterns. Note that the trade-off factor λ in Eq. (2-12) can be any real number in the range $[0,+\infty)$. It is not easy to choose an appropriate λ. Hence we slightly modify Eq. (2-12) and Eq. (2-16) as follows:

$$P(u,v) = \int_{\Omega} \{\lambda(I_x u + I_y v + I_t)^2 + (1-\lambda)[(\bar{u}-u)^2 + (\bar{v}-v)^2]\} d\Omega \tag{4-2}$$

where $\lambda \in [0,1]$, and

$$K = I_x^2 + I_y^2 + (\frac{1}{\lambda} - 1) \tag{4-3}$$

In [51], the Eqs. (2-16a) and (2-16b) were implemented by locally embedding the temporal smoothness constraint into the computation of I_x and I_y. The overlapping of this processing results in high computational complexity. In our implementation, we treat I_x and I_y only as spatial gradients of pixel brightness without considering the local temporal smoothness constraint.

In this thesis, we introduce a global temporal smoothness constraint to speed up the computation without losing too much accuracy. The global smoothness constraint is achieved as follows. For a fixed location (x, y) in the image domain Ω, the motion vector (u, v) at (x, y) varies with frame number (i.e., time), and hence, it is a function of time, i.e., $(u, v) = (u(t), v(t))$. A typical $u = u(t)$ is plotted as the dotted curve in Fig. 4-5. Note that u fluctuates significantly over time, and the temporal smoothness constraint is violated. We use a 12^{th} order polynomial (shown as the solid curve in Fig. 4-5) to fit the u component of the motion vector in the sense of least square. Similar processing is also applied to obtain a temporally smoothed v component.

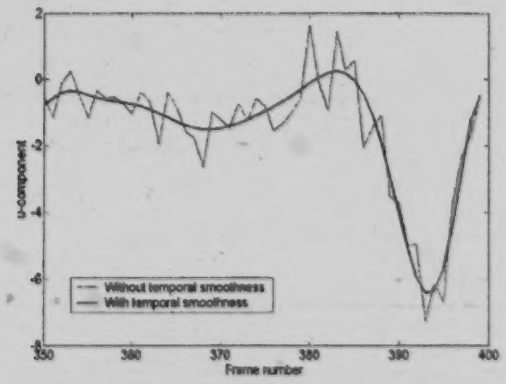

Figure 4-5. The global smoothness constraint.

By using the OFCE-based algorithm, the motion fields are estimated from the four smoothed image pairs (shown in Fig. 4-3) and shown in Fig. 4-6. As a comparison, the performance of the BMA is presented in Fig. 4-7.

Comparison between Fig. 4-6 and Fig. 4-7 shows that the OFCE-based algorithm performs better than that of the BMA for the cardiac electrical events. Note that the motion vectors represent the conduction velocity of the cardiac electrical signals. The distribution of the estimated motion vectors in different directions matches well with the visual observation. We need further verifications to guarantee that the estimated motion vectors match the real conduction velocities of the cardiac electrical signals.

Fig. 4-8 shows a pacing signal in video-4. Due to the heterogeneity of the heart tissue, the cardiac signals propagate like an elliptic wave. The ratio of longitudinal speed v_l (i.e. the velocity in the long axis direction) to the transverse speed v_t (i.e. the velocity in the short axis direction) is an important parameter to describe the conduction property of the heart tissue. When the video-4 was acquired using the optical mapping method, we also measured v_l and v_t using the multi-electrode mapping method. The measured longitudinal speed v_l and the transverse speed v_t are in the ranges 1 - 1.5 mm/ms and 0.5 - 0.8 mm/ms, repectively. The ratio v_l/v_t is in the range 1.3 - 3.

In Fig. 4-8, the longitudinal speed v_l, the transverse speed v_t, and their ratio are approximately 1.2 mm/ms, 0.65 mm/ms, and 1.85, respectively. These results match well with those obtained from the multi-electrode mapping method.

We have also compared several other motion fields estimated from other episodes of the video-4 with the results obtained using the multi-electrode mapping method. This comparison has verified that the OFCE-based motion estimation algorithm can provide satisfactory performance for cardiac video analysis.

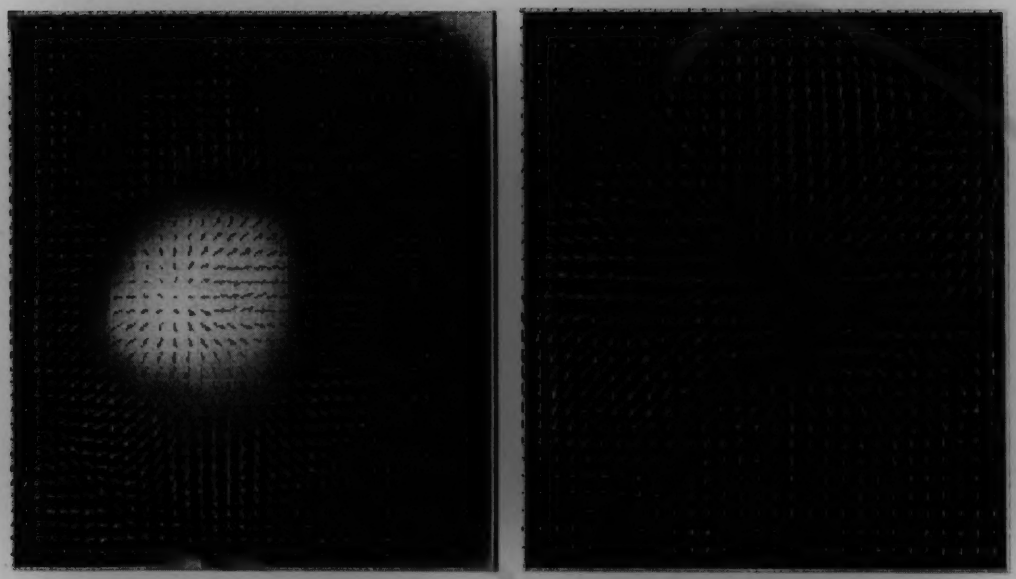

a. Motion field for image pair in Fig. 4-1(a)

b. Motion field for image pair in Fig. 4-1(b)

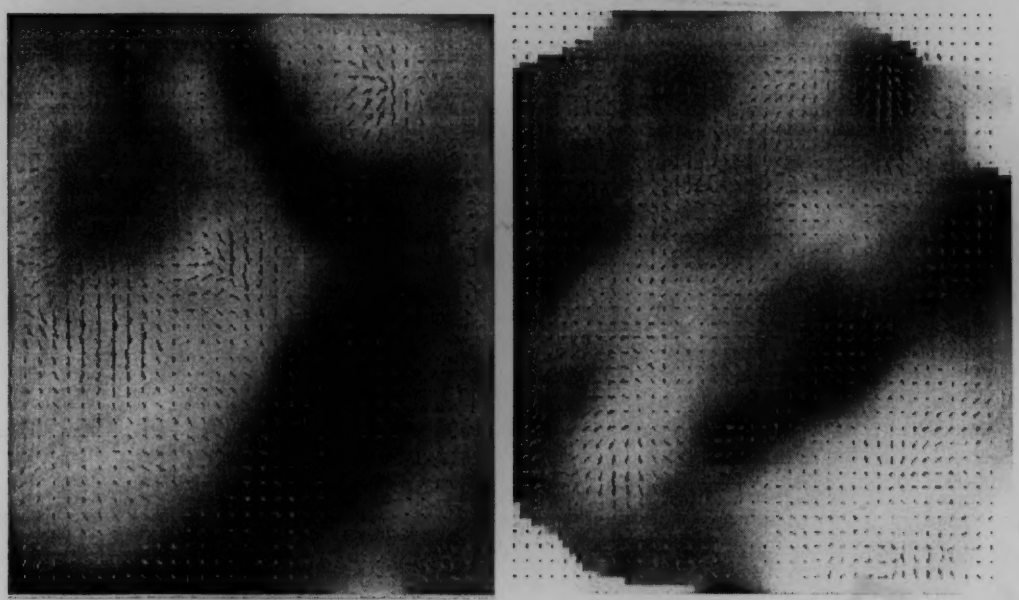

c. Motion field for image pair in Fig. 4-1(c)

d. Motion field for image pair in Fig. 4-1(d)

Figure 4-6. Motion fields obtained using the OFCE-based algorithm.

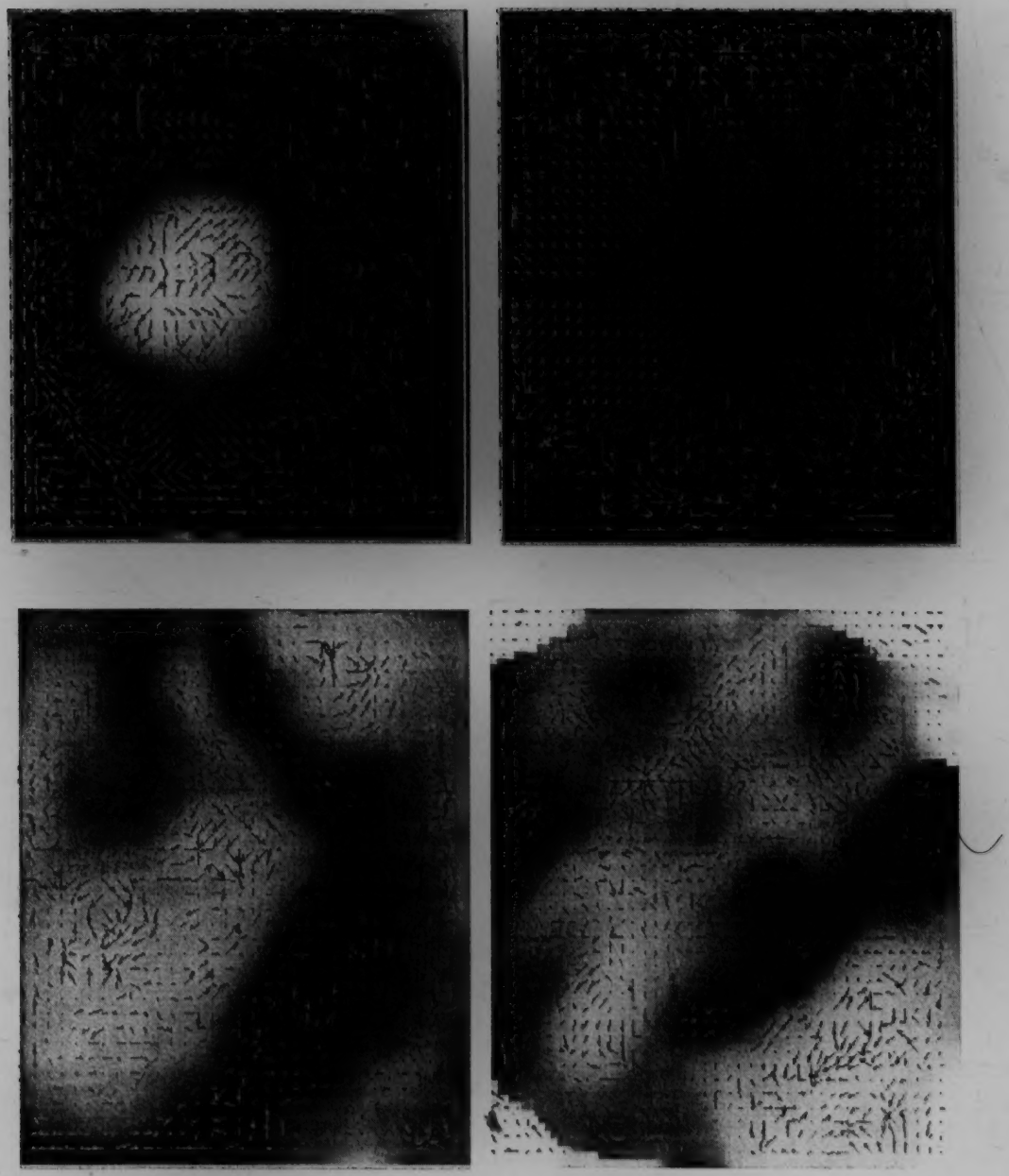

Figure 4-7. Motion fields obtained using the BMA for the four image pairs shown in Fig. 4-1.

Figure 4-8. The local motion field of a pacing signal in Video-4.

The results of our experiments have also verified two important assumptions made in [42]: (i) the conduction velocities of the cardiac electrical signals vary across the heart surface; (ii) the conduction velocity of the cardiac electrical signal sampled at a fixed location may vary dramatically over time.

4.4 Motion decomposition

In this section, we use the proposed 2-D DHHFD-RTG algorithm to decompose the four estimated motion fields shown in Fig. 4-6. Our objective is to visualize the different motion components in the four videos such that the motion components can be easily observed.

The first experiment is to decompose the motion field shown in Fig. 4-6a, which belongs to video-1. This video describes a single pacing wave without motion artifacts. Fig. 4-9 shows the estimated motion field and its three components. Fig. 4-9b shows that the curl-free component captures most motion features of the input motion field. Although it is difficult to distinguish the pure rotational component (i.e., the divergence-free component) from the input motion field, the decomposed divergence-free component (Fig. 4-9c) clearly shows that the pure rotational component in the pacing signals cannot be ignored. Fig. 4-9 also demonstrates that three dominant rotational regions are extracted. The harmonic remainder (Fig. 4-9d) is relatively weak, compared to the curl-free component. Note that this component may also contain the

residual curl-free component and divergence-free component because of the computational errors.

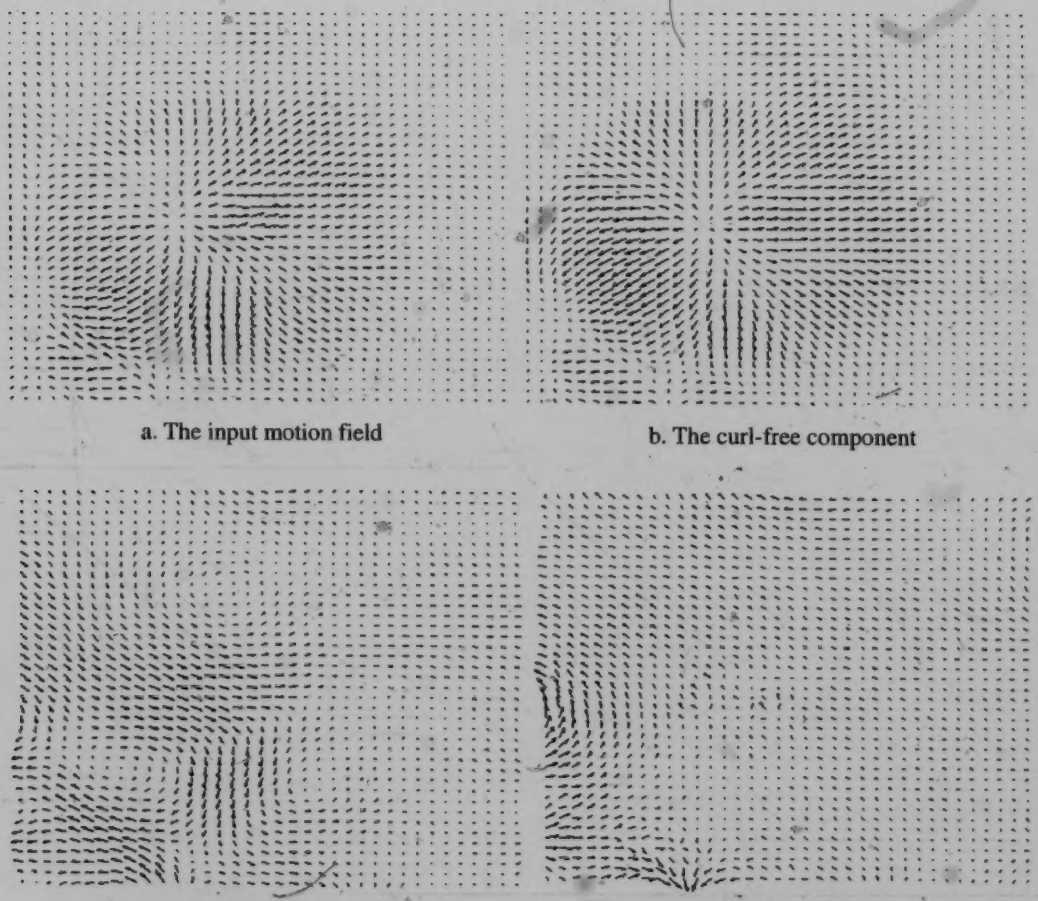

a. The input motion field

b. The curl-free component

c. The divergence-free component, magnified by 1.68 times

d. The harmonic remainder, magnified by 2.04 times

Figure 4-9. Decomposition of the motion field shown in Fig. 4-6a.

The second experiment is to decompose the motion field shown in Fig. 4-6b. This video (video-2) records a pacing wave that is propagating outwards from the pacing center. Note that this video contains strong motion artifacts. Fig. 4-10 shows the input motion field and its decomposed components. Similar to the previous experiment, the curl-free component (Fig. 4-10b) captures the most motion features of the input motion field. The divergence-free

component (Fig. 4-10c) shows that a few pure rotational region are successfully separated from the input motion field. Compared to Fig. 4-9d, Fig. 4-10d appears more chaotic. This may be resulted from the strong motion artifacts in the video-2.

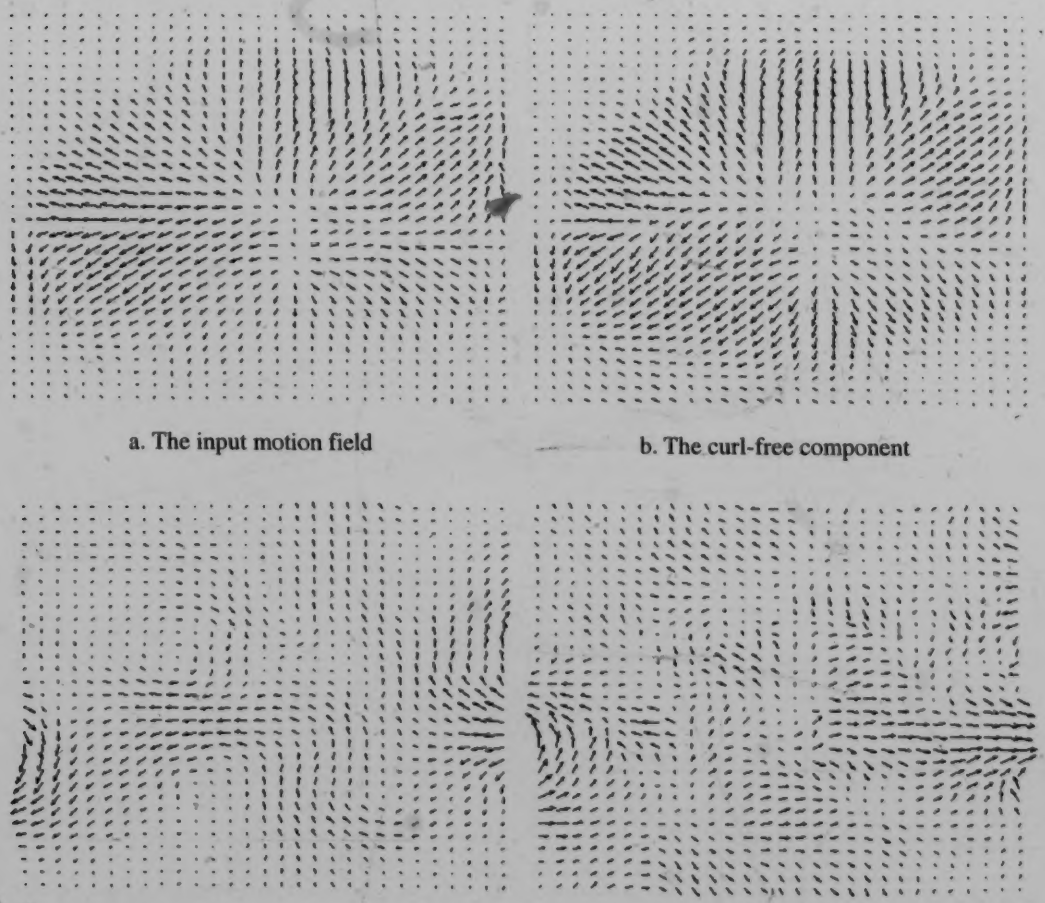

a. The input motion field

b. The curl-free component

c. The divergence-free component, magnified by 1.37 times

d. The harmonic remainder, magnified by 1.59 times

Figure 4-10. Decomposition of the motion field shown in Fig. 4-6b.

The previous two experiments deal with simple pacing waves. The third experiment investigates a complicated case - decomposition of the motion field shown in Fig. 4-6c. The input motion field and its decomposed components are shown in Fig. 4-11. The divergence-free component (Fig. 4-11c) shows that the cardiac electrical pattern is slowly rotating anticlockwise.

This rotation can be easily perceived using human eyes.

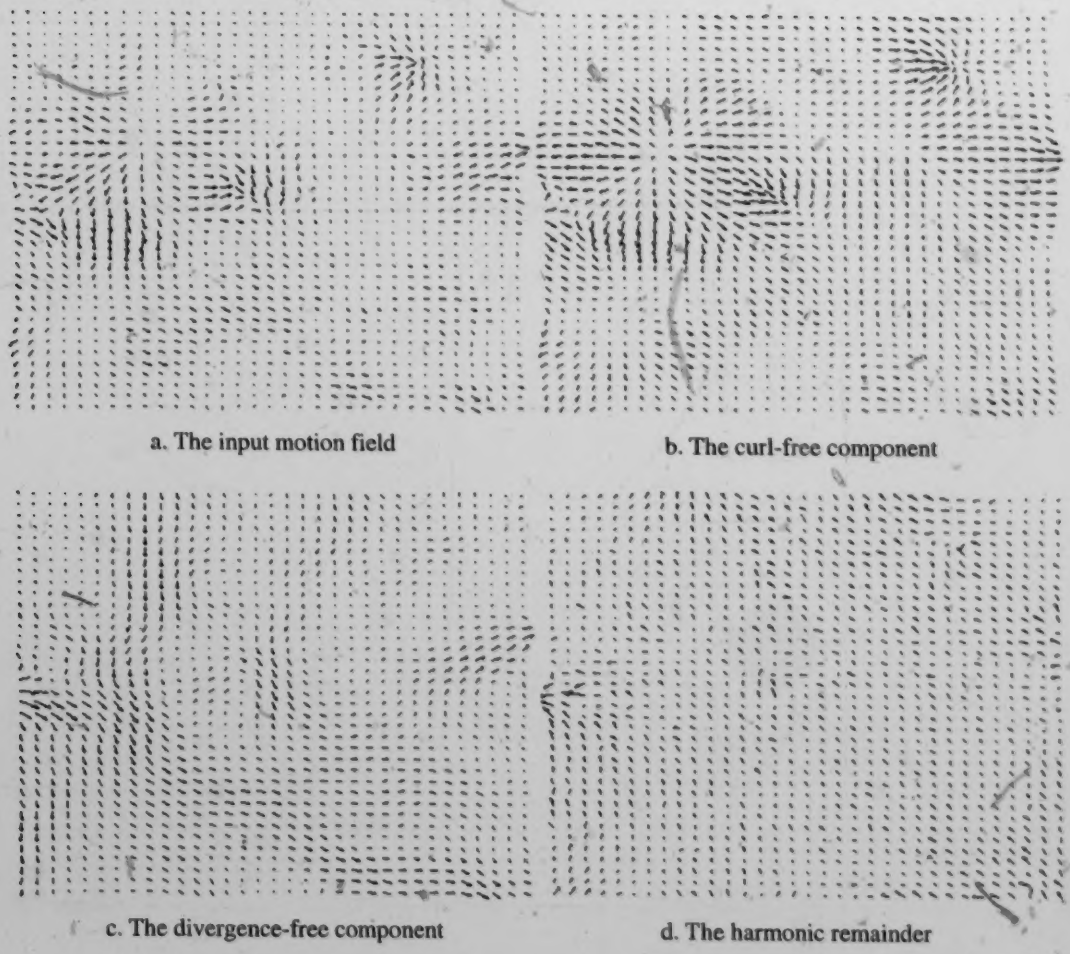

a. The input motion field

b. The curl-free component

c. The divergence-free component

d. The harmonic remainder

Figure 4-11. Decomposition of the motion field shown in Fig. 4-6c.

Let us investigate a more complicated situation. The fourth experiment decomposes the motion field shown in Fig. 4-6d, which describes the chaotic cardiac electrical activity during VF. The input motion field and its decomposed components are shown in Fig. 4-12. Several abnormal excitation spots are clearly captured in the curl-free component (Fig. 4-12a). The divergence-free component (Fig. 4-12c) clearly shows that strong rotational components exist in this video.

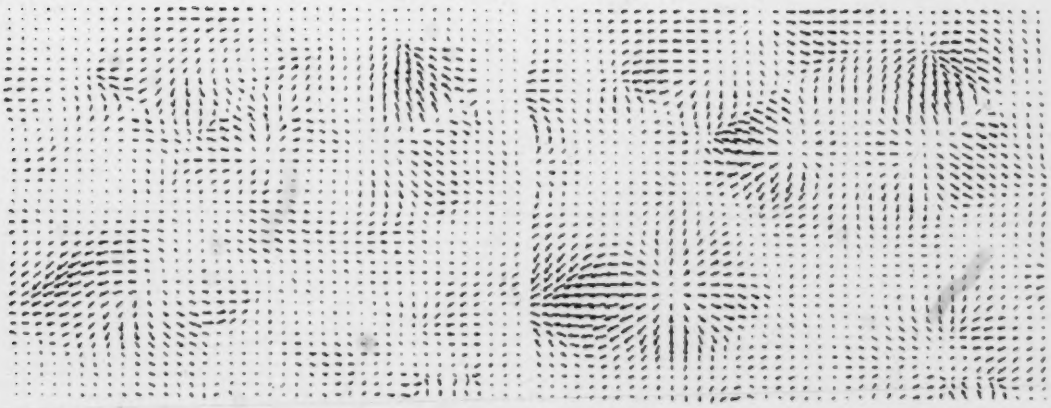

a. The input motion field

b. The curl-free component

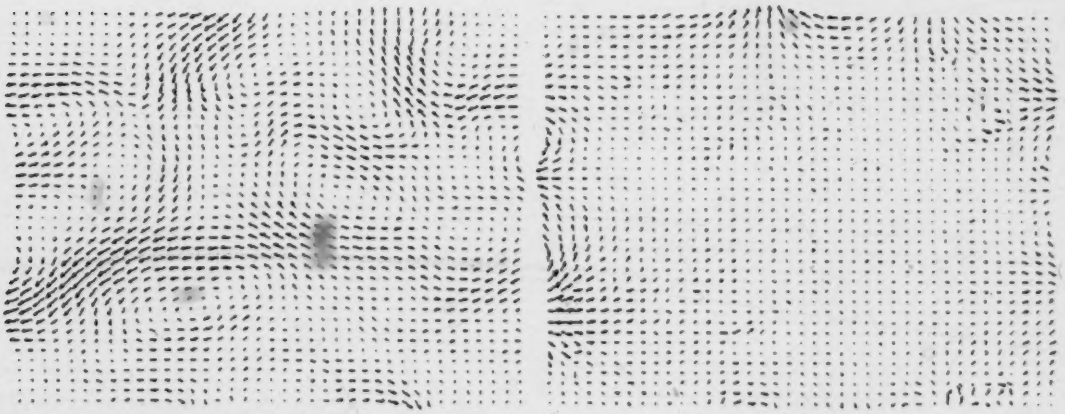

c. The divergence-free component

d. The harmonic remainder

Figure 4-12. Decomposition of the motion field shown as Fig. 4-6d.

The four experiments qualitatively show that the behavior of the heart becomes chaotic if the pure rotational component of the cardiac electrical pattern is strong.

4.5 Motion analysis

In previous section, we have presented the decomposition of four estimated motion fields of the cardiac electrical patterns. In this section, we quantitatively investigate the relationship between the heart behavior and the decomposed motion components.

To quantitatively analyze the different contributions of the different motion components to the heart behavior, especially the VF, we define the total kinetic energy of a motion field as:

$$E_K = \sum_{(x,y)\in\Omega} [u^2(x,y) + v^2(x,y)] \tag{4-5}$$

Let us denote the kinetic energy of the curl-free component and the kinetic energy of the divergence-free component as E_K^{cf} and E_K^{df}, respectively. We also define the strength ratio r_E as the ratio of E_K^{cf} to E_K^{df}, i.e.,

$$r_E = \frac{E_K^{df}}{E_K^{cf}} \tag{4-6}$$

These three quantities corresponding to the four experiments presented in the previous section can be easily calculated, and they are summarized in Table 4-4.

Table 4-4. E_K^{cf}, E_K^{df}, and r_E corresponding to the four experiments.

Experiment	**1**	**2**	**3**	**4**
Description	Pacing	Pacing with motion artifacts	VF	VF with strong chaotic motion
E_K^{cf}	6440	10960	1351	1829
E_K^{df}	1622	2408	910	1523
r_E	0.2519	0.2197	0.6734	0.8336

For the hearts belonging to different animals, the kinetic energy of the same type of motion component may differ greatly due to the conduction properties of different heart tissues. Hence, it is difficult to describe the heart behavior only using the kinetic energy. Fortunately, the strength ratio r_E seems to be able to provide useful information for description of the heart behavior. When r_E is small, the cardiac electrical signals propagate with less rotational

component than the pure expanding component. In this case, the pure expanding component is the dominant component, and hence the heart beats normally. However, when r_E becomes large, the cardiac electrical signals propagate with strong rotational component, which contributes to the fast heart rate.

According to above analyses, we believe that there exists a critical strength ratio, denoted as r_{EC}. If $r_E << r_{EC}$, the heart can be considered as healthy. However, if $r_E >> r_{EC}$ is not true, a tachyarrhythmia is likely to happen to the heart.

It is unreliable to draw any final conclusions based on only four experiments. The existence of the critical strength ratio r_{EC} and the above hypothesis need to be validated by a large number of experiments.

4.6 Critical point detection

It is well known that the critical points, such as sources/sinks, vortices, rotational centers, and saddle points, are crucial features of fluid motion, and hence it is important to detect the critical points of fluid motion for better understanding the fluid behavior. Phase portrait methods are often used to detect the critical points in fluid analysis [78 - 84].

As reviewed in Chapter 2, due to the similarity between the cardiac electrical patterns and the cloud, water, and the forest fire, traditional research methods for fluid analysis have been adopted by cardiologists. For example, Bray et al. [40] and Valderrabano et al. [41] applied the phase portrait based methods to detect the critical points in the cardiac electrical patterns. Efimov et al. [6] used the critical points to explain the mechanism of shock failure. Note that two different terminologies, "source" and the "vortex", are frequently used to indicate the tip of a spiral wave in cardiology [33 - 37].

Although it has been hypothesized that the tachyarrhythimas might be caused by the breakup of the spiral waves in the heart tissue, in practice, it is very difficult to detect a spiral wave in an acquired cardiac video. As a result, it is almost impossible to directly detect the

vortices from the cardiac data. Note that a vortex can be synthesized by a source/sink and a rotational center. In other words, we do not need to directly detect the vortices, if the sources/sinks and the rotational centers have been specified. In this thesis, the sources/sinks and the rotational centers are our primary concerns. Actually, from the acquired videos, the rotational motion of the cardiac electrical patterns can be easily perceived with human eyes. The rotational centers can be used to capture the regions containing pure rotational propagation of the cardiac electrical signals, and the lifespan of a rotational center determines the lifespan of the corresponding rotor. Moreover, as discussed in Chapter 2, periodicity exists in at least a part of the fibrillated heart data [24, 25, 35]. The periodicity of the cardiac electrical patterns can be reflected in the trajectories of the critical points. If the cardiac electrical activity is periodic, the trajectories of the critical points must also be periodic. It should also be pointed out that the pathological meanings of the saddle points are still not clear. Therefore, the vortices and the saddle points are ignored in this thesis. To avoid any confusion, we define the source/sink and the rotational center, which are known as critical points (or phase singularities) in cardiology literature, as follows.

A source is a point or a small region in the heart tissue where electrical signals propagate outward to the surrounding heart tissue.

A sink is a point or a small region in the heart tissue where electrical signals propagate inward from the surrounding heart tissue.

A rotational center is a point or a small region in the heart tissue around which the electrical signals rotate.

These definitions are coherent to the cardiological experiments, and have strict mathematical meanings. A source, a sink and a rotational center are illustrated as Fig. 4-13. It is observed the velocity at a critical point is zero.

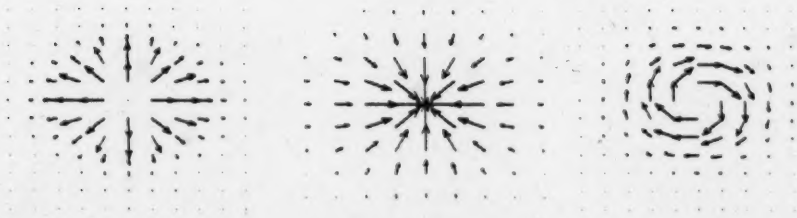

Figure 4-13. Illustration of a source, a sink, and a rotational center.

4.6.1 Criteria for detection of critical points

As mentioned in Chapters 2 and 3, an arbitrary motion field $\vec{\xi}$ can be uniquely decomposed into three components: the curl-free component ∇E, the divergence-free component $(\nabla W)^{\perp}$, and the harmonic remainder $\vec{R}$. Note that E and W are the scalar potential functions of ∇E and $(\nabla W)^{\perp}$, respectively, and they can be visualized as two surfaces.

Because the velocity is zero at a critical point, the sources/sinks can be directly detected in the curl-free field ∇E using phase portrait based methods (see Section 2.7). However, the phase portrait based methods generally require a large computational time. Fortunately, the potential function E provides us a convenient way to detect the sources/sinks in the curl-free field.

When the potential function E reaches an extremum at the location $\vec{p}$, $\partial E/\partial x = 0$ and $\partial E/\partial y = 0$ must be satisfied. In other words, the vector ∇E $(= \frac{\partial E}{\partial x}\vec{i} + \frac{\partial E}{\partial y}\vec{j})$ at location $\vec{p}$ must be zero. Hence, an extremum on the potential surface corresponds to a source/sink in the curl-free field. Taking advantage of this observation and further analyzing the geometric structure of the potential function E, the sources/sinks can be quickly detected using the following criteria:

i) The location $\vec{p}$ is a source, if $E(\vec{p})$ is a minimum;

ii) The location $\vec{p}$ is a sink, if $E(\vec{p})$ is a maximum.

These criteria are illustrated in Fig. 4-14.

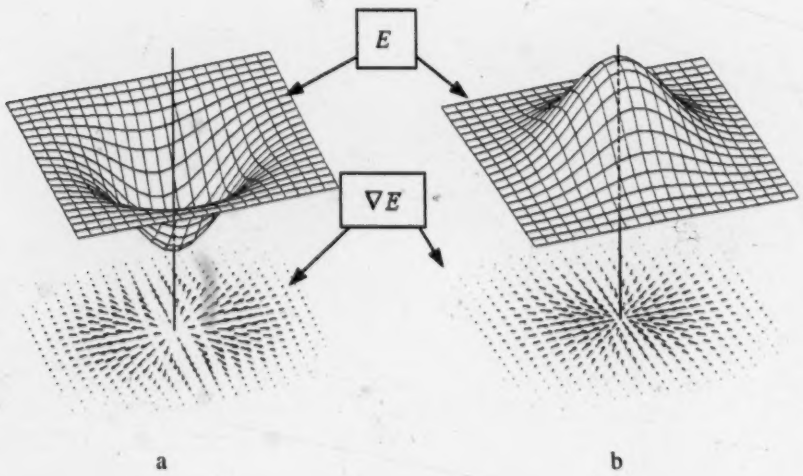

Figure 4-14. Illustration of the criteria for detection of the sources/sinks. (a) A minimum on E corresponds to a source in ∇E; (b) A maximum on E corresponds to a sink in ∇E

Similarly, the rotational centers in the divergence-free field can be detected using the potential function W. The criteria are given as follows:

iii) The location $\vec{p}$ is an anticlockwise rotational center, if $W(\vec{p})$ is a maximum;

iv) The location $\vec{p}$ is a clockwise rotational center, if $W(\vec{p})$ is a minimum.

These criteria are illustrated in Fig. 4-15.

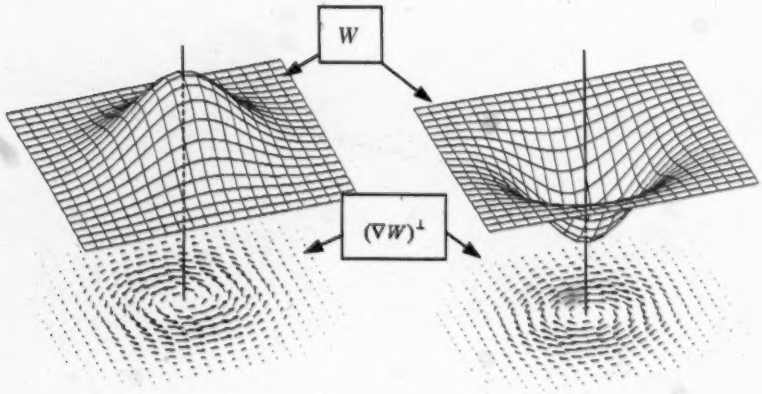

Figure 4-15. Illustration of the criteria for detection of rotational centers. (a) A maximum on W corresponds to an anticlockwise rotational center in $(\nabla W)^{\perp}$; (b) A minimum on W corresponds to a clockwise rotational center in $(\nabla W)^{\perp}$

4.6.2 Coarse detection of the critical points

We have presented four criteria to detect the critical points from the extrema of the potential surfaces. We now present a few criteria to detect the extrema on a potential surface as follows:

v) The potential surface E reaches a minimum at the location $\vec{p}$, if $E(\vec{p}) < E(\vec{q})$ for each $\vec{q}$ is a neighboring node of $\vec{p}$;

vi) The potential surface E reaches a maximum at the location $\vec{p}$, if $E(\vec{p}) > E(\vec{q})$ for each $\vec{q}$ is a neighboring node of $\vec{p}$;

vii) The potential surface W reaches a minimum at the location $\vec{p}$, if $W(\vec{p}) < W(\vec{q})$ for each $\vec{q}$ is a neighboring node of $\vec{p}$;

viii) The potential surface W reaches a maximum at the location $\vec{p}$, if $W(\vec{p}) > W(\vec{q})$ for each $\vec{q}$ is a neighboring node of $\vec{p}$.

To simplify the analysis, in the above criteria, regular rectangular grids are used. The central node $\vec{p}$ and its eight neighboring nodes (labeled as $\vec{q}_i, i \in [1,8]$) are illustrated in Fig. 4-16.

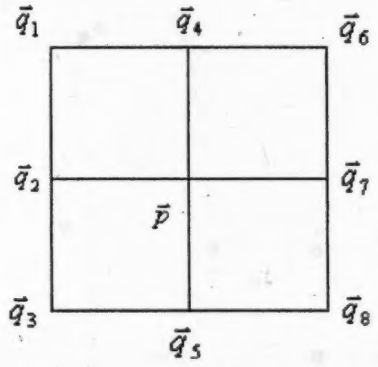

Figure 4-16. A central node and its eight neighboring nodes.

Let us apply the above criteria to detect the critical points in the motion components of the motion field shown in Fig. 4-6a. Fig. 4-17 shows the results of this experiment. The curl-free and the divergence-free potential surfaces (i.e., E and W) are shown in Figs. 4-17a and 4-17b, respectively. A source and three sinks are detected in the curl-free motion component ∇E as shown in Fig. 4-17c. Two anticlockwise rotational centers and three clockwise rotational centers are also detected in the divergence-free component $(\nabla W)^{\perp}$ as shown in Fig. 4-17d. To observe the detected critical points clearly, we magnify two regions respectively surrounding a source and an anticlockwise rotational center. The two magnified regions are shown in Figs. 4-17e and 4-17f.

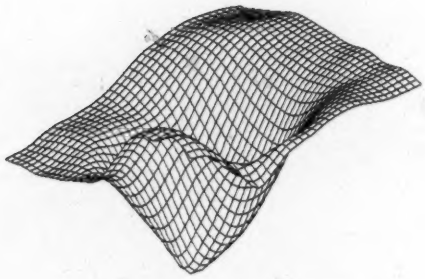

a. The curl-free potential surface E

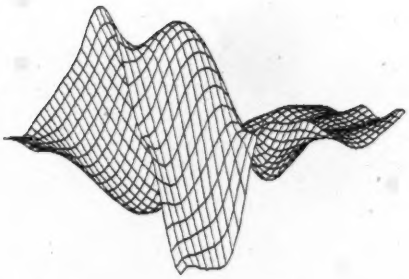

b. The divergence-free potential surface W

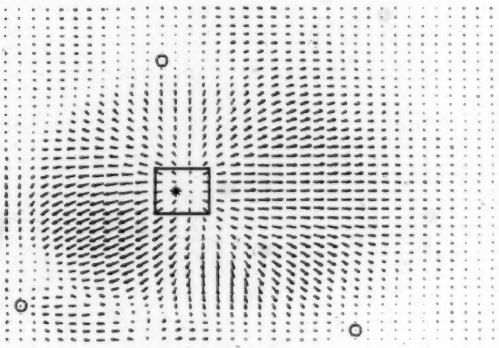

c. A source and three sinks

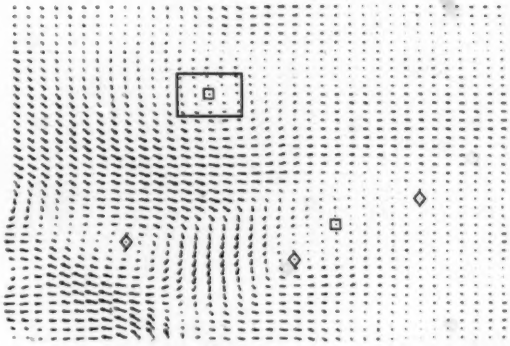

d. Two anticlockwise centers and three clockwise centers

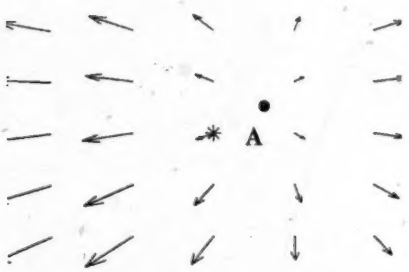

e. The magnified region in panel c.

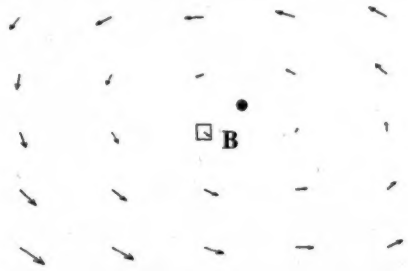

f. The magnified region in panel d.

Figure 4-17. Coarse detection of the critical points. A "*" denotes a source, a "○" denotes a sink, a "□" denotes an anticlockwise rotational center, a "◊" denotes a clockwise rotational center, and a "•" denotes a critical center obtained from visual observation.

There are several limitations of the critical point detection algorithm. First, too many critical points are detected. In the clinical experiment, only one pacing wire is set to contact the heart surface, and hence, only one source and no sinks should be detected. However, three sinks have been detected by the proposed algorithm. Likewise, in this experiment, the number of the rotational centers should be much less than detected. Secondly, as shown as Figs. 4-17e and 4-17f, the detected critical points are not consistent with the visual centers (indicated as "A" and "B", respectively). Note that all detected critical points are located at the mesh grids, at which the component vectors do not vanish. This violates the definitions of the critical points. In other words, the accuracy of the results is not very high, when the above criteria are directly applied to detect the critical points.

4.6.3 Fine detection of the critical points

As shown in previous subsection, there exists a discrepancy between a detected critical point and the true visual center. This discrepancy mainly results from three factors: the size of the grid, computational errors and the limitation of the discrete gradient algorithm.

As discussed in [51], the grids downsample the image domain, and they result in the quantization error. If the size of a regular rectangular grid is $\Delta x \times \Delta y$, the largest quantization error is $\frac{1}{2}\Delta x \times \frac{1}{2}\Delta y$. This means that a detected critical point may deviate from its corresponding visual center by $\frac{1}{2}\Delta x \times \frac{1}{2}\Delta y$ (see Figs. 4-17e and 4-17f).

It is expected that the two potential surfaces are absolutely smooth. However, computational errors result in a few trivial extrema in the potential surfaces. These trivial extrema, which correspond to the trivial critical points surrounded by small vectors (see Figs. 4-17c and 4-17d), do not deviate too much from the potential values of their corresponding neighbors. From the point of view of fluid dynamics, the behavior of the fluid is mainly determined by those dominant critical points surrounded by large vectors, rather than the trivial critical points. Thus the trivial critical points, or more essentially, the trivial extrema on the

potential surfaces, should be removed.

The discrepancy between the detected critical points and the visual centers also arises from the discrete gradient algorithm. Theoretically, on a continuous potential surface E, an extremum exists where $\partial E/\partial x = 0$ and $\partial E/\partial y = 0$ satisfy. However, on a discrete potential surface E, an extremum does not always correspond to the location where $\partial E/\partial x = 0$ and $\partial E/\partial y = 0$. Fig. 4-18 demonstrates a discrete potential surface and its corresponding gradient field. It can be clearly observed that the minimum corresponds to the detected source marked as "A", rather than the visual center that is marked as "B".

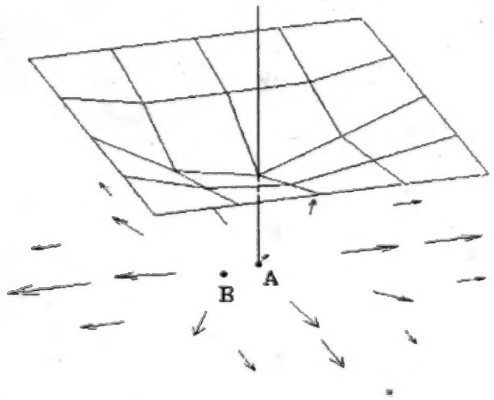

Figure 4-18. The discrepancy between a detected source and its corresponding visual center.

To effectively remove the trivial extrema on a discrete potential surface, the surfaces is smoothed using the anisotropic diffusion equation. As presented in Section 2.4, the anisotropic diffusion equation does not shift the locations where the extrema occur. Fig. 4-19 shows two smoothed potential surfaces corresponding to Figs. 4-17a and 4-17b. In later of this chapter, the gradient field of the curl-free potential surface and the the co-gradient field of the divergence-free potential surface are called the smoothed curl-free field and the smoothed divergence-free field, respectively.

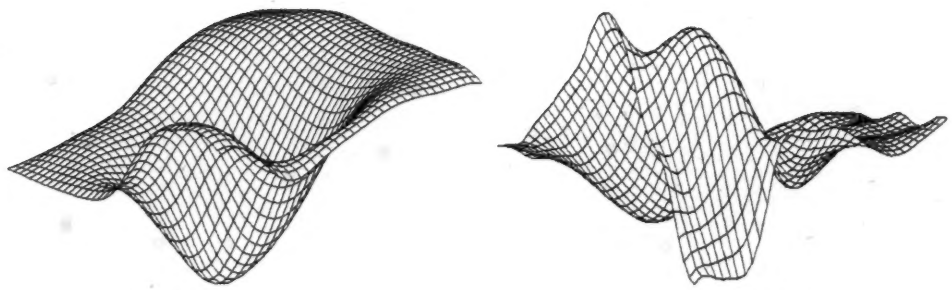

a b

Figure 4-19. Smoothed potential surfaces using the anisotropic diffusion equation.

(a) Smoothed version of Fig. 4-17a; (b) Smoothed version of Fig. 4-17b

To improve the accuracy, the size of the grid has to be reduced. However, reducing the size of all grids globally results in the decrease of the efficiency. To balance the accuracy and the efficiency, a local coarse-to-fine pyramid is built to hierarchically search the critical points.

The hierarchical searching scheme is illustrated in Fig. 4-20. First, we find the coarse extrema on a potential surface using the criteria presented in Subsection 4.6.2. The location of a critical point corresponding to a coarse extremum can be straightforwardly specified. Note that this coarse critical point is often different from the visual center. We then locally insert a new grid node between two neighboring nodes in the 5×5 symmetrical neighborhood of the coarse critical point such that a local 9×9 neighborhood around the coarse critical point is generated. Hence, the size of each local grid is reduced. Based on the newly generated 9×9 grids, another small potential surface can be built by bicubical interpolation (shown as the middle-layer surface in Fig. 4-20a). Re-searching the extremum on the newly built surface, a finer critical point can be located. This coarse-to-fine hierarchical searching scheme can be iteratively used till the discrepancy between the detected critical point and the corresponding visual center is small. A fine critical point is indicated as the lower point in Fig. 4-20b.

If the location of a coarse critical point is very close (less than 3 grid nodes) to the boundary of the potential surface (or more essentially, close to the boundary of the image), the

5×5 symmetrical neighborhood cannot be used. In this case, a 3×3 symmetrical neighborhood, or another asymmetrical neighborhood can be chosen as an alternative. Three typical neighborhood configurations are shown in Fig. 4-21. To guarantee the smoothness of the newly generated surface, the bicubical interpolation is preferred.

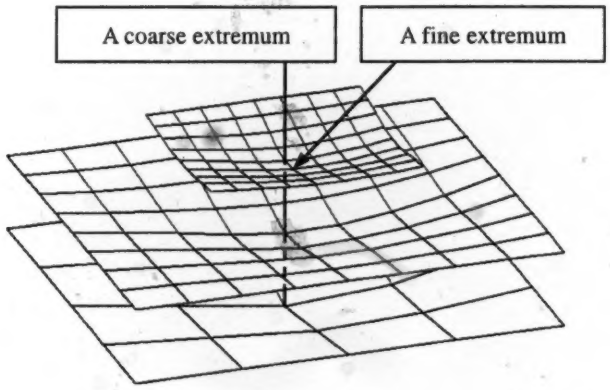

a. The coarse-to-fine potential surface pyramid

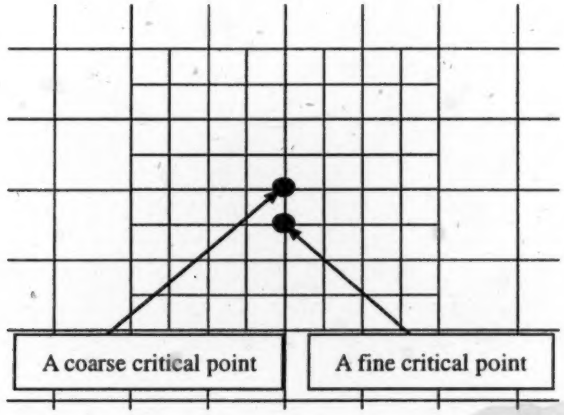

b. Coarse-to-fine detection of critical point

Figure 4-20. Illustration of the hierarchical searching scheme.

Note that he bicubical interpolation may introduce a few new local extrema, and hence additonal critical points are generated. We only keep the extremum that satisfies following two conditions. First, the type of the newly detected extremum is same as that of the original coarse

extremum. In other words, if the original coarse extremum is a minimum (or a maximum), the newly detected extremum is also a minimum (or a maximum). Secondly, the location of the finer extremum is closest to the location of the original coarse extremum among all same-type candidates.

The discrepancy can be reduced by iteratively using the coarse-to-fine searching scheme. However, the discrepancy caused by the discrete gradient algorithm cannot be removed. Fortunately, when the size of the grid is small, the accuracy of the hierarchical searching scheme generally provides very good results.

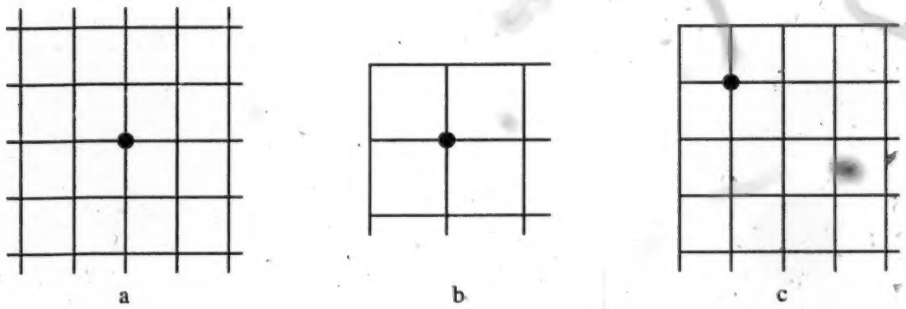

Figure 4-21. Three typical neighborhood configurations for bicubical interpolation. (a) A 5×5 symmetrical neighborhood; (b) A 3×3 symmetrical neighborhood; (c) An asymmetric neighborhood

4.6.4 Performance of the fine detection

In the previous subsection, we presented the method used in this thesis for critical point detection with high accuracy. This method contains two key techniques: the smoothing of the potential surfaces and a hierarchical searching scheme. In this subsection, we evaluate the performance of this method with four experiments.

In Experiment-1, the critical points are detected for the motion field shown in Fig. 4-6a. Note that the pacing source, essentially the small region where the pacing wire contacts the heart surface, is known in advance. Moreover, no motion artifacts interfere with the experimental results. The results of this experiment are shown in Fig. 4-22. The source is

detected in the smoothed curl-free component of the given motion field as shown in Fig. 4-22a. Two anticlockwise centers and a clockwise center are deteceted in the smoothed divergence-free field as shown in Fig. 4-22b. Fig. 4-22c shows all detected critical points superposed on the corresponding smoothed image. The rotational directions around the detected rotational centers are also indicated by the dashed arrows.

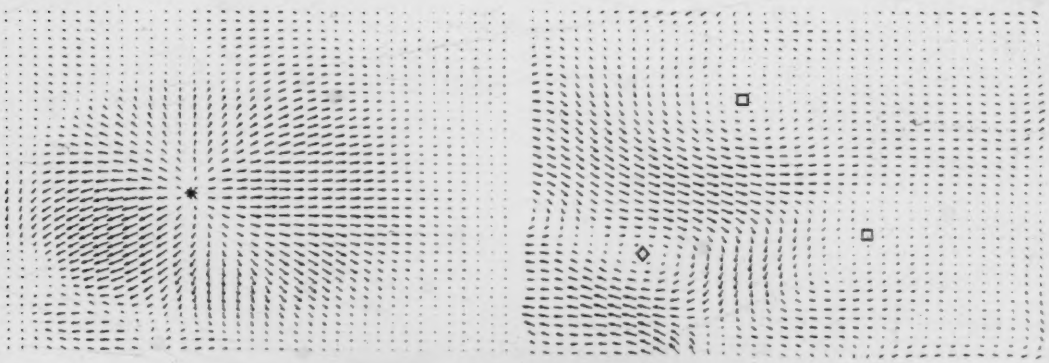

a. The detected source

b. The detected rotational centers

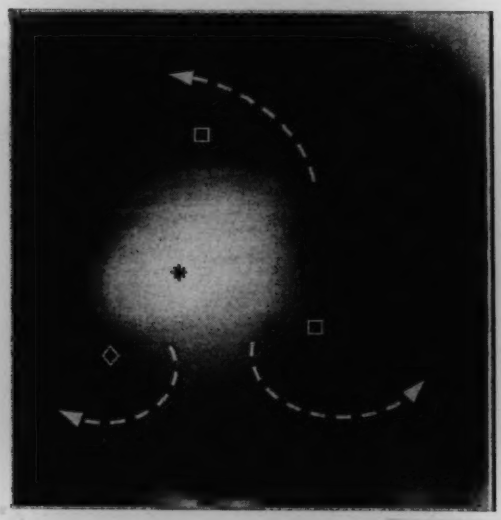

c. All critical points superposed on the smoothed image

Figure 4-22. Detected critical points in Experiment-1. Figs. (a) and (b) are obtained by the smoothed potential surfaces shown in Figs. 4-19a and 4-19b.

The detected source matches very well with the pacing setting. We have also detected the critical points in other image frames of this video, and the results show that the proposed method can provide satisfactory performance. The largest error between the detected source and the pacing setting is less than 3 pixels. Direct visual observation also verifies the correctness of the detected rotational centers.

In Experiment-2, the critical points are detected for the motion field shown in Fig. 4-6b. This video records a pacing wave with strong motion artifacts. Fig. 4-23 shows the results of this experiment. The rotational directions of the cardiac electrical signals have been indicated by the dashed arrows in Fig. 4-23e.

The detected source matches satisfactorily with the pacing setting. Further tests of this video show that the largest error between the detected source and the pacing setting is less than 5 pixels. The detected rotational centers match well with direct visual observation.

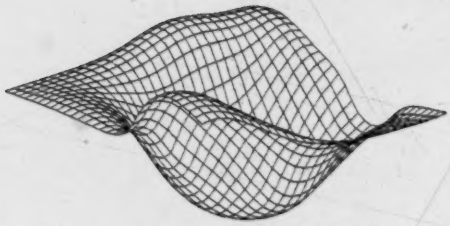

a. The smoothed curl-free potential surface E

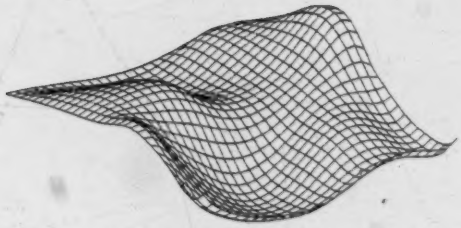

b. The smoothed divergence-free potential surface W

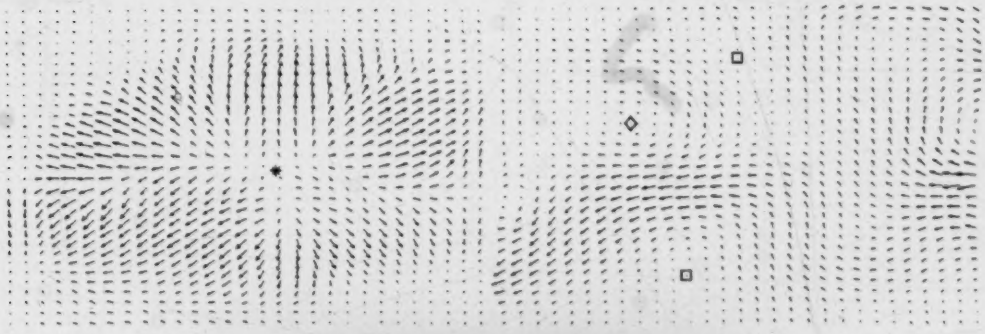

c. The detected source

d. The detected rotational centers

e. All critical points superposed on the smoothed image

Figure 4-23. Detected critical points in Experiment-2.

In clinical practice, the source is often referred to a region rather than only one pixel. For the video-1 and the video-2, the detected sources are mostly within the regions where the pacing wires contact with the heart surface. Therefore, the proposed algorithm can provide satisfactory results.

To observe the behavior of the cardiac electrical signals during VF, we further investigate the detection of the critical points for the two motion fields shown in Figs. 4-6c and 4-6d. The motion of the cardiac electrical patterns in video-3 can be easily perceived with human eyes. Therefore, we detect the critical points in the motion field shown in Fig. 4-6c first. The results of this experiment (denoted as Experiment-3) are presented in Fig. 4-24. The detected critical points in this experiment match very well with the visual observation.

In Experiment-4, we detect the critical points for the motion field shown in Fig. 4-6d. The results of this experiment are shown in Fig. 4-25. Because the patterns in video-4 are much more chaotic than those in video-3, the critical points in this video cannot be directly distinguished. Hence, the results of experiment-4 cannot be verified with human eyes.

Although some cardiologists believe that the pathological changes in the heart tissue can introduce abnormal sources in the cardiac electrical patterns, short animation of the detected sources shows that not all of the detected sources are caused by pathological changes in the heart tissue. Some sources are temporarily formed by the interaction between the dominant source and the heterogeneity of the heart tissue. Similarly, some sinks and some rotational centers can also be temporarily formed in the same way. As a result, the number of the detected critical points keeps changing. It is highly possible that some old critical points disappear, some new critical points generate, and meanwhile, some other critical points keep wandering. It is very difficult to locate them using other techniques, including clinical experiments. In other words, it is difficult to validate the results obtained in Experiment-4.

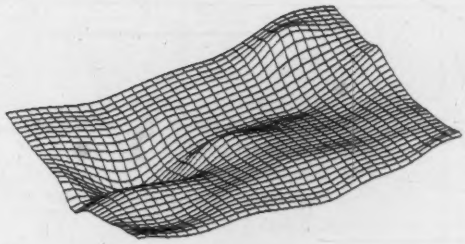

a. The smoothed curl-free potential surface E

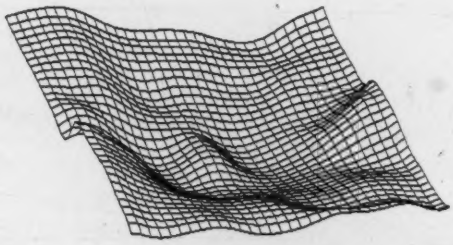

b. The smoothed divergence-free potential surface W

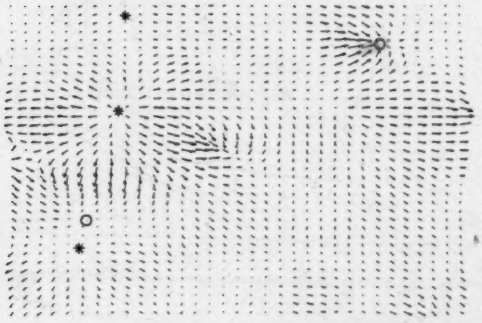

c. The detected sources and sinks

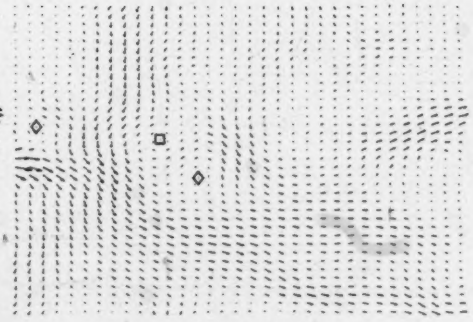

d. The detected rotational centers

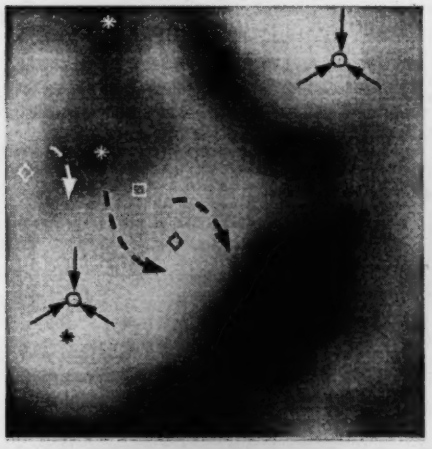

e. All critical points superposed on the smoothed image

Figure 4-24. Detected critical points in Experiment-3.

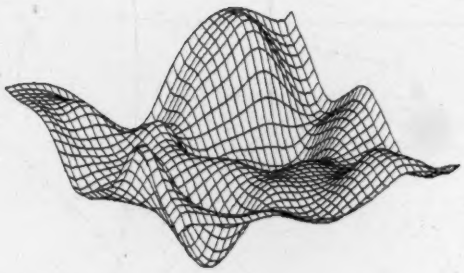

a. The smoothed curl-free potential surface E

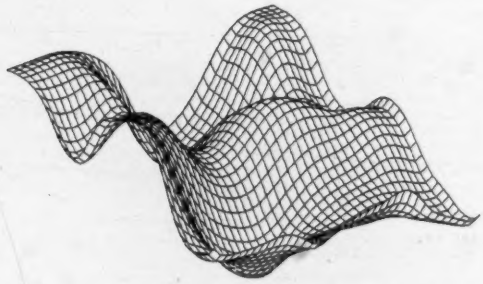

b. The smoothed divergence-free potential surface W

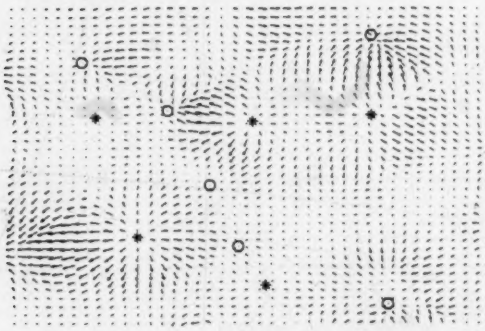

c. The detected sources and sinks

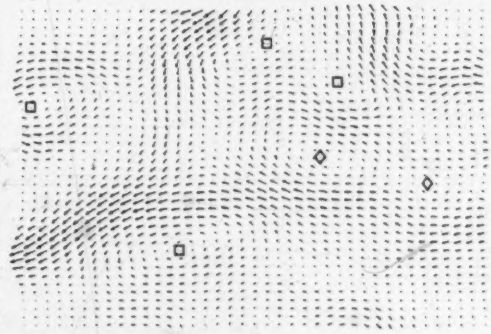

c. The detected rotational centers

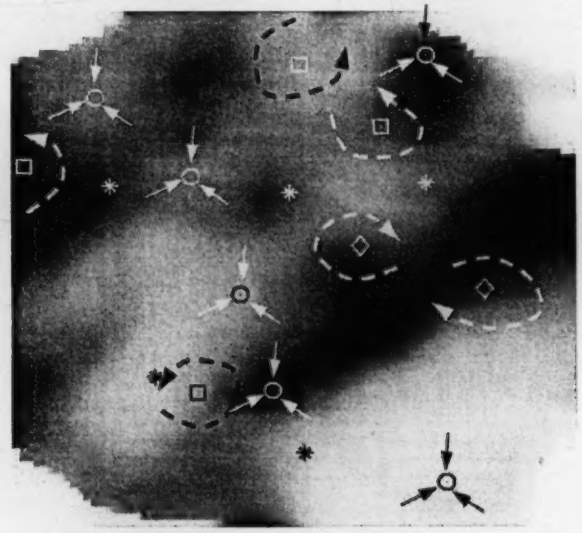

e. The critical points superposing on the smoothed iamge

Figure 4-25. Detected critical points in Experiment-4.

4.7 Summary

In this chapter, we have presented a novel framework for cardiac video analysis. This framework contains four stages: image smoothing, motion estimation, motion decomposition, and critical point detection. The anisotropic diffusion equation has been used to smooth the noisy cardiac electrical patterns. The motion fields of the cardiac electrical patterns have then been estimated using the OFCE-based motion estimation algorithm. Next, the estimated motion fields have been decomposed using the proposed 2-D DHHFD-RTG. Finally, we have detected the critical points in the motion fields using a hierarchical searching scheme.

Four experiments have been carried out to quantitatively analyze the decomposed motion components and evaluate the performance of the proposed techniques. The results of these experiments suggest that the heart behavior can be determined by the strength ratio of the pure rotational component to the pure expanding component of a motion field. If the strength ratio is large, a tachyarrhythmia may be introduced. The simulation results also show that the proposed framework provides satisfactory performance in detecting the critical points in the estimated motion fields.

Chapter 5

Conclusions and Future Work

The VF is the main cause of sudden cardiac death in the industrialized world. Cardiologists believe that the VF is related to the turbulent propagation of the cardiac electrical signals. It has been hypothesized that the VF are introduced from a high-frequency electrical source, or from the breakup of a large spiral wave, or from multiple random wavelets in the heart, or from all of the above. To visualize and analyze the cardiac electrical signals, a voltage-sensitive dye is injected into the heart to convert the cardiac electrical signals into observable optical patterns. The optical patterns are then captured by a high-speed video camera. Although a large number of cardiac electrical patterns have been acquired, the analysis of the dynamic patterns is not very efficient.

In this thesis, we have proposed a novel framework to quantitatively analyze the acquired cardiac electrical patterns. This framework contains four stages: image smoothing, motion estimation, motion decomposition, and critical point detection. In the image smoothing stage, the anisotropic diffusion equation is applied to smooth the cardiac electrical patterns such that strong noise present in the acquired cardiac videos can be removed while the salient features in the image sequence can be preserved. In the motion estimation stage, the motion fields of the cardiac electrical patterns are estimated using the OFCE-based algorithm. In the motion decomposition stage, the proposed 2-D DHHFD-RTG algorithm is used to decompose an estimated motion field into three components: a pure expanding part, a pure rotational part, and a harmonic remainder. Thus, the contributions of the pure expanding part and the pure rotational part to the heart behavior can be directly observed. In the stage of critical point detection, the critical points, which can describe the structure of an estimated motion field, are detected with high accuracy using two potential surfaces and a hierarchical searching scheme. Compared to the traditional phase portrait methods that are based on the local pattern matching, the proposed framework is simpler, faster, and more efficient. The detected critical points not only provide

important clues for therapy of the tachyarrhythmias, but also are helpful for understanding the cardiac dynamics.

Several experiments have been carried out to evaluate the proposed framework. The results of the experiments give rise to a hypothesis that a tachyarrhythmia is likely to happen to the heart when the strength ratio of the pure rotational component to the pure expanding component in a motion field of the cardiac electrical signals is significant. Our experiments also show that the detected critical points match well with the visual observations if the cardiac electrical patterns contain less chaotic motion. Theoretically, the proposed framework can also be used to analyze an arbitrary fluid flow.

5.1 Future work

This work can be extended along the following four directions:

A) To build a multi-scale parametric motion model, which can be used for target recognition, target tracking, and video indexing.

It is necessary to study the 2-D DHHFD in-depth. Note that the 2-D DHHFD implicitly provides a parametric model for complex image motions, such as deformable motion and fluid motion. The parameters of this motion model can include the critical points, the strength of each critical point, the area of the region around a critical point, and other salient features. It is well known that most meaningful salient features can be directly detected using the two potential surfaces. Therefore, the parametric motion model can be easily built. Moreover, fine-to-coarse potential surfaces can be obtained using the anisotropic diffusion equation in different scale to smooth the two potential surfaces (i.e., the curl-free potential surface and the divergence-free potential surface). Hence, smoothed motion components in different scale can also be obtained. In this way, the single-scale parametric motion model can be further extended to a multi-scale parametric motion model. Like other motion models [77, 87], this parametric motion model can also be used for target recognition and target tracking. The multi-scale parametric motion model can also be applied to video indexing [88].

B) To synthesize the dynamic texture using the 2-D DHHFD.

A complex motion field can be generated by arbitrarily creating the critical points and their corresponding parameters. If a source image is available, a target image can be synthesized from the source image and the generated complex motion field. Based on this simple idea, the 2-D DHHFD can also be used to synthesize the dynamic texture [89].

C) To develop a robust motion estimation algorithm, which can deal with the motion discontinuities and fast image motion.

The correctness of the proposed video analysis framework is mostly determined by the quality of the estimated motion fields, which cannot be verified in most cases. If the quality of the estimated motion fields is not satisfactory, the results of the framework are generally unacceptable. For example, the OFCE-based motion estimation algorithm assumes that the image motion must be spatially smooth. As a result, it does not perform well when applied to estimate the motion fields of a VF video with strong chaotic motion. In this case, the motion discontinuities cannot be correctly captured. Another limitation of the OFCE-based motion estimation algorithm is that it requires slow image motion. Hence, the sampling rate of the high-speed video camera has to be high.

It can be easily inferred that a robust motion estimation algorithm is strongly needed. The desired motion estimation algorithm must satisfy two conditions: (i) it is able to deal with the motion discontinuities in a cardiac video with strong chaotic motion; (ii) it can correctly estimate the fast image motion. The layered motion model [86] might be a possible solution for addressing this issue.

D) To remove the motion artifacts in an original cardiac electrical video such that the proposed framework can be used to analyze the electrical signals of the heart *in vito*

The proposed framework may not be directly used to analyze the cardiac electrical patterns with strong motion artifacts. The motion artifacts give rise to abrupt emergence or disappearance of some patterns. Therefore, if the motion artifacts exist, the estimated motion fields are likely to have errors. Furthermore, if the temporal sampling rate of the camera is not

very high, the motion artifacts result in violation of the temporal smoothness constraint in the motion estimation algorithm. This limitation also implies that the proposed framework may not achieve satisfactory results when directly applied to analyze the electrical propagation of a heart *in vivo*. This challenging problem has been attracting great research interests, however, no breakthrough has been reported.

Bibliography

1 E. Stein, *Rapid analysis of arrhythmias: A self-study program.* 3rd Edn. Lippincott Williams & Wilkins. 2000.

2 A. V. Holden, "A last wave from the dying heart," *Nature*, Vol. 392, pp. 20–21, 1998.

3 L. S. Gettes, W. E. Cascio, and W. E. Sanders, "Mechanisms of sudden cardiac death," *Cardiac electrophysiology: From cell to bedside*, 2nd edition, eds: D. P. Zipes and J. Jalife, Philadelphia, PA: Saunders, pp. 527–538, 1995.

4 Bernus, B. Van Eych, H. Verschelde, and A. V. Panfilov, "Transition from ventricular fibrillation to ventricular tachycardia: a simulation study on the role of Ca^{2+}-channel blockers in human ventricular tissue," *Physics in Medicine and Biology*, Vol. 47, pp. 4167-4179, 2002.

5 K. Skouibine, N. Trayanova, P. Moore, "Success and failure of the defibrillation shock: insights from a simulation study," *Journal of Cardiovascular Electrophysiology*, Vol. 11, No. 7, pp. 785-796, 2000.

6 I. R. Efimov, Y. Cheng, D. R. Van Wagoner, T. Mazgalev, P. J. Tchou, "Virtual electrode-induced phase singularity: a basic mechanism of defibrillation failure," *Circulation Research*, Vol. 82, No. 8, pp. 918-925, 1998.

7 L. Wang, "Implantable cardioverter–defibrillator therapy: The state-of-the-art and future perspectives," *Indian Heart Journal.* 2002; 54: 672–675.

8 F. J. Chorro, J. Canoves, J. Guerrero, L. Mainar, J. Sanchis, L. Such and V. Lopez-Merino, "Alteration of ventricular fibrillation by Flecainide, verapamil, and solatol. An experimental study," *Circulation*, Vol. 101, pp. 1606–1615, 2000.

9 F. J. Chorro, J. Canoves, J. Guerrero, L. Mainar, J. Sanchis, E. Soria, L. Such, A. Rosado and V. Lopez-Merino, "Opposite effects of myocardial stretch and verapamil on the complexity of the ventricular fibrillatory pattern:and experimental study," *Pacing and Clinical Electrophysiology,* Vol. 23 pp. 1594–1603, 2000.

10 F. H. Samie, R. Mandapati, R. A. Gray, Y. Watanabe, C. Zuur, J. Beaumont, and J. Jalife, "A mechanism of transition from ventricular fibrillation to tachycardia: effect of calcium channel blockade on the dynamics of rotating waves," *Circulation Research*. Vol. 86, pp. 684-491, 2000.

11 F. H. Fenton, A. Karma, H. M. Hastings, and S. J. Evans, "Transition from ventricular tachycardia to ventricular fibrillation as function of tissue characteristics in a computer model," Europace, Vol. 1, Supplement D, paper no. 109P/10 (2000).

12 R. H. Clayton, A. Murray, R. W. Campbell, "Analysis of the body surface ECG measured in independent leads during ventricular fibrillation in humans," *Pacing Clinical Electrophysiol.* Vol. 18, No. 10, pp. 1876-1881, 1995.

13 Q. Ni, R. S. Macleod, R. L. Lux, and B. Taccardi, "A novel interpolation method for electric potential fields in the heart during excitation," *Annals of Biomedical Engineering*, Vol. 26, pp. 597–607, 1998.

14 M. Shenasa, M. Borggrefe, G. Breithardt, W. Haverkamp, and G. Hindricks, *Cardiac Mapping*, Future Publishing Company, Inc. Mount Kisco, NY. pp. 225-235, 1993.

15 A. M. Gillis, V. G. Fast, S. Rohr, and A. G. Kleber, "Mechanism of ventricular defibrillation: the role of tissue geometry in the changes in transmembrane potential in patterned myocyte cultures," *Circulation*. 2000; 101:2438-2445.

16 F. X. Witkowski, L. J. Leon, P. A. Penkoske, R. B. Clark, M. Spano, W. L. Ditto, W. R. Giles, "A method for visualization of ventricular fibrillation: Design of a cooled fiberoptically coupled image intensified CCD data acquisition system incorporating wavelet shrinkage based adaptive filtering," *Chaos*, Vol. 8, No. 1, pp. 94-102, 1998.

17 F. X. Witkowski, L. J. Leon, P. Penkoske, W. Giles, M. Spano, W. L. Ditto, A. Winfree, "Spatiotemporal evolution of ventricular fibrillation," *Nature*. Vol. 392, pp. 78 – 82, 1998.

18 D. Sung, J. H. Omens, and A. D. McCulloch, "Model-based analysis of optically mapped epicardial activation patterns and conduction velocity," *Annals of Biomedical Engineering*, Vol. 28, pp. 1085-1092, 2000.

19 G. K. Moe, and J. A. Abildskov, "Atrial fibrillation as a self-sustained arrythmia independent of focal discharge," America Heart Journal. Vol. 58, pp. 59-70, 1959.

20 G. K. Moe, W. C. Rheinbolt, and J. A. Abildskov, "A computer model of atrial fibrillation," *America Heart Journal*. Vol. 67, pp. 200-220, 1964.

21 V. I. Krinsky, "Spread of excitation in an inhomogeneous medium (state similar to cardiac fibrillation)," *Biophyisiology*. Vol. 11, pp. 776-784, 1966.

22 M. A. Allessie, "Reentrant mechanisms underlying fibrillation," In Cardiac electrophysiology. From cell to bedside (Eds. D. P. Zipes & J. Jalife) 2nd edn, pp. 562-566. Philadelphia, PA: Saunders. 1995.

23 M. J. Janse, "Vulnerability to ventricular fibrillation," *Chaos*. Vol. 8, pp. 149-156, 1998.

24 J. Chen, R. Mandapati, O. Berenfeld, A. C. Skanes, and J. Jalife "High-frequency periodic sources underlie ventricular fibrillation in the isolated rabbit heart," *Circulation Research*. 2000; 86:86-93.

25 A. Garfinkel, P. Chen, D. O. Walter, H. S. Karagueuzian, B. Kogan, S. J. Evans, M. Karpoukhin, C. Hwang, T. Uchida, M. Gotoh, O. Nwasokwa, P. Sager, and J. N. Werss, "Quasiperiodicity and chaos in cardiac fibrillation," *Journal of Clinical Investigation*. Vol. 99, No. 2, pp. 305-314, 1997.

26 R. A. Gray, J. Jalife, A. Panfilov, W. T. Baxter, C. Cabo, and A. M. Pertsov, "Non-stationary vortex-like reentrant activity as a mechanism of polymorphic ventricular tachycardia in the isolated rabbit heart," *Circulation*. Vol. 91, pp. 2454-2469, 1995.

27 J. M. Starobin and C. F. Starmer, "Spiral wave meandering, wavefront-obstacle separation and cardiac arrhythmias," *Computers in Cardiology*, pp. 233-236, 1996.

28 F. H. Fenton, E. M. Cherry, H. M. Hastings, and S. J. Evans, "Multiple mechanisms of spiral wave breakup in a model of cardiac electrical activity." *Chaos*, Vol. 12, pp. 852-892, 2002.

29 A. Xu, and M. R. Guevara, "Two forms of spiral-wave reentry in an ionic model of ischemic ventricular myocardium," Chaos. Vol. 8, No. 1, 1998.

30 A. Panfilov, A. Pertsov, "Ventricular fibrillation: evolution of the multiple-wavelet hypothesis," *Phil. Trans. R. Soc. Lond.* A (2001) 359, 1315-1325.

31 S. Sinha, A. Pande, and R. Pandit, "Defibrillation via the elimination of spiral turbulence in a model for ventricular fibrillation," *Physics Review Letters*, Vol. 86, pp. 3678-3681, 2001.

32 A. Panfilov, S. Muller, V. Zykov, and J. Keener, "Elimination of spiral waves in cardiac tissue by multiple subthreshold shocks," Phys. Rev. E61 (2000), 4644-4647.

33 P. Jais, M. Haissaguerre, D. C. Shah, S. Chouairi, L. Gencel, M. Hocini, and J. Clementy, "A focal source of atrial fibrillation treated by discrete radiofrequency ablation," *Circulation*. 1997; 95:572-576.

34 R. Mandapati, A. Skanes, J. Chen, O. Berenfeld, J. Jalife, "Stable microreentrant source as a mechanism of atrial fibrillation in the isolated sheep heart," *Circulation*. 2000; 101: 194-197.

35 J. Chen, R. Mandapati, O. Berenfeld, A. C. Skanes, and J. Jalife, "High-frequency periodic sources underlie ventricular fibrillation in the isolated rabbit heart," *Circulation Research*. 2000;86:86-93.

36 A. Zaitsev, O. Berenfeld, S. Mironov, J. Jalife, and A. Pertsov, "Distribution of excitation frequencies on the epicardial and endocardial surfaces of the fibrillating ventricular wall of the sheep heart," *Circulation Research*. 2000; 86:408-417.

37 F. H. Samie, J. Jalife, "Mechanisms underlying ventricular tachycardia and its transition to ventricular fibrillation in the structurally normal heart," *Cardiovascular Research*. 2001 May; 50(2):242-250.

38 G. E. Morley and D. Vaidya "Understanding conduction of electrical impulses in the mouse heart using high-resolution video imaging technology," *Microscopy research and technique* 52:241-250, 2001.

39 R. A.Gray, A. M. Pertsov, and J. Jalife, "Spatial and temporal organization during cardiac fibrillation," *Nature*. Vol. 392, pp. 75-78, 1998.

40 M. A. Bray, S. Lin, R. R. Aliev, B. J. Roth, and J. P. Wikswo Jr, "Experimental and

theoretical analysis of phase singularity dynamics in cardiac tissue," *Journal of Cardiovascular Electrophysiology*. 2001; 12(6):716-722.

41 M. Valderrabano, P. Chen, and S. Lin, "Spatial distribution of phase singularities in ventricular fibrillation," *Circulation*, 2003; 108(3): 354-359.

42 R. S. MacLeod, Q. Ni, R. O. Kuenzler et al, "Spatiotemporal analysis of cardiac electrical activity," In *The Thirty-Second Asilomar Conference on Signals, Systems, and Comptuters*, M.B. Matthews, Ed., 1998, pages 309--313. IEEE Press.

43 M. Eldar, D. G. Ohad, J. J. Goldberger, Z. Rotstein, S. Hsu, D. K. Swanson, and A. J. Greenspan, "Transcutaneous multielectrode basket catheter for endocardial mapping and ablation of ventricular tachycardia in the pig," *Circulation*. 1997; 96:2430-2437.

44 J. K. .Mell, D. A. Jordan, Y. Xiao, Y. Zheng, J. G. Akar, and D. E. Haines, "Wavelet analysis atrial fibrillation electrograms," *IEEE International Conference on Acoustics, Speech, and Signal Processing*, II:357-360, 2003.

45 Y. Xiao, Y. Zheng, D. A. Jordan, J. G. Akar, and D. E. Haines, "Parameter estimation of spiral waves from atrial electrograms," *IEEE International Conference on Acoustics, Speech, and Signal Processing*, V:245-248, 2003.

46 J. Jalife, *Basic Cardiac Electrophysiology for the Clinician*. 1st Edn., Futura Publishing Co., 1998.

47 K. R. Laurita, D. S. Rosenbaum, "Interdependence of modulated dispersion and tissue structure in the mechanism of unidirectional block," *Circulation Research*. 2000;87:922

48 K. Polthier and E. Preuβ, "Variational approach to vector field decomposition," Scientific Visualization, Springer Verlag, *Proc. of Eurograhics Workshop on Scientific Visualization*, 2000.

49 K. Polthier and E. Preuβ, "Identifying vector fields singularities using a discrete Hodge Decomposition," *Visualization and Mathematics III*, Eds: H. C. Hege, K. Polthier, pp. 113-134, Springer Verlag, 2003.

50 Y. Tong, S. Lombeyda, A. N. Hirani, and M. Desbrum, "Discrete multiscale vector field

decomposition," *ACM SIGRAPH'03*, July 27-31, Sandiego, 2003.

51 B. Horn and B. Schunk, "Determining optical flow," *Artificial Intelligence*, 17:185–203, 1981.

52 T. Lindeberg, "Scale-space theory in computer vision", Kluwer Academic Publishers, 1994.

53 P. Perona, and J. Malik, "Scale-space and edge detection using anisotropic diffusion," *IEEE Transactions on Pattern Analysis and Machine Intelligence*. Vol. 12, No. 7, pp. 629-639, 1990.

54 Q. Li, T. Li, S. Zhu, and C. Kambhamettu, "How well can wavelet denoising improve the accuracy of computing fundamental matrices?" *IEEE Workshop on Motion and Video Computing*, pp. 247-252, Dec. 2002, Orlando, FL, USA.

55 D. L. Donoho, and I. M. Johnstone, "Ideal spatial adaptation via wavelet shrinkage," *Biometrika*, Vol. 81, pp. 425-455, 1994.

56 D. L. Donoho, "De-noising by soft-thresholding," *IEEE Transactions on Information Theory*, Vol. 41, No. 3, pp. 613-627, May 1995.

57 S. G. Chang, B. Yu, and M. Vattereli, "Adaptive wavelet thresholding for image denoising and compression," *IEEE Transactions on Image Processing*, Vol. 9, No. 9, pp. 1532-1546, 2000.

58 J. Babaud, A. Witkin, M. Baudin, and R. Duda, "Uniqueness of the gaussian kernel for scale-space filtering," *IEEE Transactions on Pattern Analysis and Machine Intelligence*, Vol. 8, No. 1, pp. 26-33, 1986.

59 Y. L. You, W. Xu, A. Tannenbaum, and M. Kaveh, "Behavioral analysis of anisotropic diffusion in image processing," *IEEE Transactions on Image Processing*, Vol. 5, No. 11, pp. 1539-1553, Nov. 1996.

60 G. W. Wei, "Generalized Perona-Malik equation for image restoration," *IEEE Transactions on Signal Processing Letters*," Vol. 6, No. 7, July, 1999.

61 U. Clarenz, U. Diewald, and M. Rumpf, "Anisotropic geometric diffusion in surface

processing," *In Proceedings of IEEE Visualization'00*, pp. 397-405, 2000.

62 C. Kambhamettu, D. B. Goldgof, D. Terzopoulos, and T. S. Huang, "Nonrigid motion analysis," In Tzay Young, editor, Handbook of Pattern Recognition and Image Proccessing: Computer Vision, Volumn 2, pp: 405-430. Academic Press, San Diego, California, 1994.

63 L. Zhou, C. Kambhamettu, and D.B. Goldgof, "Extracting nonrigid motion and 3D structure of hurricanes from satellite image sequences without correspondences," *IEEE Conference on Computer Vision and Pattern Recognition*, Vol. 2, pp. 280-285, 1999.

64 L. Zhou, C. Kambhamettu, and D.B. Goldgof, "Structure and nonrigid motion analysis of satellite cloud images," *Indian Conference on Computer Vision, Graphics, and Image Processing*, pp. 285-291, Dec. 1998.

65 T. Corpetti, E. Memin, P. Perez, "Dense estimation of fluid flows," *IEEE Transactions on Pattern Recognition and Machine Intelligence*, Vol. 24, No. 3, pp. 365-380, March 2002.

66 D. Bereziat, I. Herlin, and L. Younes, "A generalized optical flow constraint and its physical interpretation," *IEEE Conference on Computer Vision and Pattern Recognition*, Vol. 2, pp. 2487-2492, 2000.

67 H. Nagel, "On a constraint equation for the estimation of displacement rates in image sequences," *IEEE Transactions on Pattern Analysis and Machine Intelligence*, Vol. 11, pp. 13–30, 1989.

68 B. Schunck, "The motion constraint equation for the optical flow," *International Conference on Pattern Recognition*, pp. 20–22, 1984.

69 P. Anandan, "A computational framework and an algorithm for the measurement of visual motion," *International Journal of Computer Vision*, 2:283-310, 1989.

70 R. Li, B. Zeng, and M. L. Liou, "A new three-step search algorithm for fast block motion estimation," *IEEE Transactions on Circuits and Systems for Video Technology*, Vol. 4, pp. 438-442, Aug. 1994.

71 L. M. Po, and W. C. Ma, "A novel four-step search algorithm for fast block motion estimation," *IEEE Transactions on Circuits and Systems for Video Technology*, Vol. 6, No.

3, pp. 313-317, Jun. 1996.

72 J. Chang, D. Edwards, and Y. Yu, "Statistical estimation of fluid flow fields," *ECCV workshop on Statistical Methods in Video Processing*, Copenhagen, pp. 91-96, June 2002.

73 A. Mitiche, *Computational Analysis of Visual Motion*, Plenum Press, New York, 1994.

74 L. Hill, and T. Vlachos, "Shape adaptive phase correlation," *IEE Electronics Letters*, Vol. 37, No. 25, pp1512-1513. 2000.

75 R. Abraham, J. Marsden, and T. Ratiu, (Eds), *Manifolds, Tensor Analysis, and Applications*. Applied Mathematical Sciences, Vol. 75, Springer 1988.

76 D. T. Lawton, and W. F. Gardner, "Translational decomposition of flow fields," *in Proceedings of the DARPA Image Understanding Workshop*, pp. 697-705, April 1993. Washington, D.C.

77 M. J. Black, Y. Yacoob, A. D. Jepson and D. J. Fleet, "Learning parameterized models of image motion," *IEEE Conference on Computer Vision and Pattern Recognition*, pp. 561-567, 1997.

78 R. M. Ford and R. N. Struckland, "Representing and visualizing fluid flow images and velocimetry data by nonlinear dynamical systems," *Graphical Models And Image Processing*, Vol. 57, No. 6, November, pp. 462-482, 1995.

79 R. M. Ford, "Critical point detection in fluid flow images," *International Conference on Image Processing*, Vol. 2, pp. 700-703, 1997.

80 C. F. Shu, and R. C. Jain, "Vector field analysis for oriented patterns," *IEEE Transactions on Pattern Analysis and Machine Intelligence*, Vol. 6, No. 9, pp. 946-950, 1994.

81 Q. Yang and B. Parvin, "Feature based visualization of geophysical data," *International Conference on Computer Vision and Pattern Recognition*, Vol. 2, pp. 276-281, 2000.

82 Q. Yang, B. Parvin, and A. Mariano, "Singular features in sea surface temperature data," *International Conference on Pattern Recognition*, Vol. 1, pp 516-520, 2000.

83 J. Zhong, T. S. Huang, and R. J. Adrian, "Extracting 3D vortices in turbulent fluid flow," *Transactions on Pattern Analysis And Machine Intellegence*, Vol. 20, No. 2, February, pp.

193-199, 1998.

84 P. C. Hu and R. N. Strichland, "Detection of vortices in flow images using the wavelet transform," *International Conference on Image Processing*. Vol. 2, pp. 740-744, 1999.

85 Rodríguez, J.A., C. Urdiales, A. Bandera, and F. Sandoval, "A multiresolution spatiotemporal motion segmentation technique for video sequences based on pyramidal structures," *Pattern Recognition Letters*, Vol. 23 No. 14, pp. 1761-1769, 2002.

86 J. Y. A Wang and E. H. Adelson, "Representing moving images with layers," *IEEE Transactions on Image Processing Special Issue: Image Sequence Compression*, Vol. 3, No. 5, pp. 625-638, Sept. 1994.

87 G. D. Hager, P. N. Belhumeur, "Efficient region tracking with parametric models of geometry and illumination," *IEEE Transactions on Pattern Analysis and Machine Intelligence*, Vol. 20, No. 10, pp. 1125-1139, 1998.

88 R. Fablet, P. Bouthemy, "Statistical motion-based object indexing using optic flow field," *International Conference on Pattern Recognition*, Vol. 4, pp. 287-290, 2000.

89 G. Doretto, A. Chiuso, Y. Wu, S. Soatto, "Dynamic textures," *International Journal of Computer Vision*, Vol. 51, No. 2, pp. 91-109, 2003.

Appendix A:

Derivation from Eq. (3-10) to Eq. (3-11)

In Subsection 3.1.2, we skipped several derivation steps from Eq. (3-10) to Eq. (3-11) for the sake of simplicity. Here, we present the details between Eq. (3-10) and Eq. (3-11).

We re-write Eq. (3-10) as follows:

$$D(E) = \int_{\Omega} \left\| \nabla E - \vec{\xi} \right\|^2 d\Omega \tag{3-10}$$

Applying the necessary condition $\partial D / \partial E_i = 0$ to the distance function $D(E)$ defined as Eq. (3-10), and using Eq. (3-9a), we have:

$$\begin{aligned}
&\forall i, \int_{\Omega} \frac{\partial(\nabla E - \vec{\xi})}{\partial E_i} \cdot (\nabla E - \vec{\xi}) d\Omega = 0 \\
&\Rightarrow \forall i, \int_{\Omega} \frac{\partial(\nabla E)}{\partial E_i} \cdot (\nabla E - \vec{\xi}) d\Omega = 0 \\
&\Rightarrow \forall i, \int_{\Omega} \frac{\partial(\nabla \sum_{i=1}^{L} \phi_i E_i)}{\partial E_i} \cdot (\nabla E - \vec{\xi}) d\Omega = 0 \\
&\Rightarrow \forall i, \int_{\Omega} \frac{\partial(\sum_{i=1}^{L} (\nabla \phi_i) E_i)}{\partial E_i} \cdot (\nabla E - \vec{\xi}) d\Omega = 0 \\
&\Rightarrow \forall i, \int_{\Omega} \nabla \phi_i \cdot (\nabla E - \vec{\xi}) d\Omega = 0
\end{aligned} \tag{3-11}$$

Appendix B:

Expansion of Eq. (3-14)

In Subsection 3.1.2, we have presented that expansion of Eq. (3-14) can lead to a linear equation, Eq. (3-15). Here, we present the details of the expansion of Eq. (3-14) using a simple example. Eq. (3-14) is re-written as follows:

$$\forall i, \sum_{T_k \in N(i)} \nabla \phi_{ik} \cdot (\nabla E)_k = \sum_{T_k \in N(i)} \nabla \phi_{ik} \cdot \vec{\xi}_k \tag{3-14}$$

Not losing generality, we first consider a simple vector field with 3×3 vectors. The triangulation of this vector field is shown as Fig. B-1. All nodes are labelled by *italic* numbers, and all triangular grids are labelled by circled *italic* numbers.

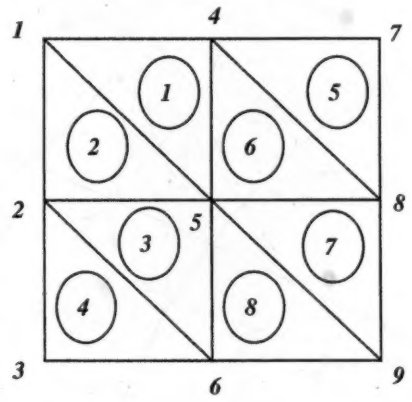

Figure B-1. Triangulation of a simple vector field with 3×3 vectors.

The 1st node has two neighboring triangles, i.e. T_1 and T_2, and hence $N(1) = \{T_1, T_2\}$. The left-hand side of Eq. (3-14) can be expanded as:

$$\sum_{T_k \in N(1)} \nabla \phi_{1k} \cdot (\nabla E)_k = \nabla \phi_{11} \cdot (\nabla E)_1 + \nabla \phi_{12} \cdot (\nabla E)_2$$

$$= \nabla \phi_{11} \cdot (\nabla \sum_{j=1}^{L} \phi_j E_j)_1 + \nabla \phi_{12} \cdot (\nabla \sum_{j=1}^{L} \phi_j E_j)_2$$

$$= \nabla\phi_{11} \cdot (\nabla\phi_{11} E_1 + \nabla\phi_{41} E_4 + \nabla\phi_{51} E_5) + \nabla\phi_{12} \cdot (\nabla\phi_{12} E_1 + \nabla\phi_{22} E_2 + \nabla\phi_{52} E_5)$$

$$= (\nabla\phi_{11} \cdot \nabla\phi_{11} + \nabla\phi_{12} \cdot \nabla\phi_{12}) E_1 + (\nabla\phi_{12} \cdot \nabla\phi_{22}) E_2$$
$$+ (\nabla\phi_{11} \cdot \nabla\phi_{41}) E_4 + (\nabla\phi_{11} \cdot \nabla\phi_{51} + \nabla\phi_{12} \cdot \nabla\phi_{52}) E_5$$

For the 2nd node, $N(2) = \{T_2, T_3, T_4\}$, and therefore

$$\sum_{T_k \in N(2)} \nabla\phi_{2k} \cdot (\nabla E)_k = \nabla\phi_{22} \cdot (\nabla E)_2 + \nabla\phi_{23} \cdot (\nabla E)_3 + \nabla\phi_{24} \cdot (\nabla E)_4$$

$$= \nabla\phi_{22} \cdot (\nabla\phi_{12} E_1 + \nabla\phi_{22} E_2 + \nabla\phi_{52} E_5) + \nabla\phi_{23} \cdot (\nabla\phi_{23} E_2 + \nabla\phi_{53} E_5 + \nabla\phi_{63} E_6)$$
$$+ \nabla\phi_{24} \cdot (\nabla\phi_{24} E_2 + \nabla\phi_{34} E_3 + \nabla\phi_{64} E_6)$$

$$= (\nabla\phi_{22} \cdot \nabla\phi_{12}) E_1 + (\nabla\phi_{22} \cdot \nabla\phi_{22} + \nabla\phi_{23} \cdot \nabla\phi_{23} + \nabla\phi_{24} \cdot \nabla\phi_{24}) E_2 + (\nabla\phi_{24} \cdot \nabla\phi_{34}) E_3$$
$$+ (\nabla\phi_{22} \cdot \nabla\phi_{52} + \nabla\phi_{23} \cdot \nabla\phi_{53}) E_5 + (\nabla\phi_{23} \cdot \nabla\phi_{63} + \nabla\phi_{24} \cdot \nabla\phi_{64}) E_6$$

For the 3rd node, $N(3) = \{T_4\}$. Therefore

$$\sum_{T_k \in N(3)} \nabla\phi_{3k} \cdot (\nabla E)_k = \nabla\phi_{34} \cdot (\nabla E)_4$$

$$= \nabla\phi_{34} \cdot (\nabla\phi_{24} E_2 + \nabla\phi_{34} E_3 + \nabla\phi_{64} E_6)$$

$$= (\nabla\phi_{34} \cdot \nabla\phi_{24}) E_2 + (\nabla\phi_{34} \cdot \nabla\phi_{34}) E_3 + (\nabla\phi_{34} \cdot \nabla\phi_{64}) E_6$$

For the 4th node, $N(4) = \{T_1, T_5, T_6\}$.

$$\sum_{T_k \in N(4)} \nabla\phi_{4k} \cdot (\nabla E)_k = \nabla\phi_{41} \cdot (\nabla E)_1 + \nabla\phi_{45} \cdot (\nabla E)_5 + \nabla\phi_{46} \cdot (\nabla E)_6$$

$$= \nabla\phi_{41} \cdot (\nabla\phi_{11} E_1 + \nabla\phi_{41} E_4 + \nabla\phi_{51} E_5) + \nabla\phi_{45} \cdot (\nabla\phi_{45} E_4 + \nabla\phi_{75} E_7 + \nabla\phi_{85} E_8)$$
$$+ \nabla\phi_{46} \cdot (\nabla\phi_{46} E_4 + \nabla\phi_{56} E_5 + \nabla\phi_{86} E_8)$$

$$= (\nabla\phi_{41} \cdot \nabla\phi_{11}) E_1 + (\nabla\phi_{41} \cdot \nabla\phi_{41} + \nabla\phi_{45} \cdot \nabla\phi_{45} + \nabla\phi_{46} \cdot \nabla\phi_{46}) E_4$$
$$+ (\nabla\phi_{41} \cdot \nabla\phi_{51} + \nabla\phi_{46} \cdot \nabla\phi_{56}) E_5 + (\nabla\phi_{45} \cdot \nabla\phi_{75}) E_7 + (\nabla\phi_{45} \cdot \nabla\phi_{85} + \nabla\phi_{46} \cdot \nabla\phi_{86}) E_8$$

For the 5th node, $N(5) = \{T_1, T_2, T_3, T_6, T_7, T_8\}$.

$$\sum_{T_k \in N(5)} \nabla\phi_{5k} \cdot (\nabla E)_k$$

$$= \nabla\phi_{51}\cdot(\nabla E)_1 + \nabla\phi_{52}\cdot(\nabla E)_2 + \nabla\phi_{53}\cdot(\nabla E)_3 + \nabla\phi_{56}\cdot(\nabla E)_6 + \nabla\phi_{57}\cdot(\nabla E)_7 + \nabla\phi_{58}\cdot(\nabla E)_8$$

$$\begin{aligned}
&= \nabla\phi_{51}\cdot(\nabla\phi_{11}E_1 + \nabla\phi_{41}E_4 + \nabla\phi_{51}E_5) + \nabla\phi_{52}\cdot(\nabla\phi_{12}E_1 + \nabla\phi_{22}E_2 + \nabla\phi_{52}E_5)\\
&+ \nabla\phi_{53}\cdot(\nabla\phi_{23}E_2 + \nabla\phi_{53}E_5 + \nabla\phi_{63}E_6) + \nabla\phi_{56}\cdot(\nabla\phi_{46}E_4 + \nabla\phi_{56}E_5 + \nabla\phi_{86}E_8)\\
&+ \nabla\phi_{57}\cdot(\nabla\phi_{57}E_5 + \nabla\phi_{87}E_8 + \nabla\phi_{97}E_9) + \nabla\phi_{58}\cdot(\nabla\phi_{58}E_5 + \nabla\phi_{68}E_6 + \nabla\phi_{98}E_9)
\end{aligned}$$

$$\begin{aligned}
&= (\nabla\phi_{51}\cdot\nabla\phi_{11} + \nabla\phi_{52}\cdot\nabla\phi_{12})E_1 + (\nabla\phi_{52}\cdot\nabla\phi_{22} + \nabla\phi_{53}\cdot\nabla\phi_{23})E_2 + (\nabla\phi_{51}\cdot\nabla\phi_{41} + \nabla\phi_{56}\cdot\nabla\phi_{46})E_4\\
&+ (\nabla\phi_{51}\cdot\nabla\phi_{51} + \nabla\phi_{52}\cdot\nabla\phi_{52} + \nabla\phi_{53}\cdot\nabla\phi_{53} + \nabla\phi_{56}\cdot\nabla\phi_{56} + \nabla\phi_{57}\cdot\nabla\phi_{57} + \nabla\phi_{58}\cdot\nabla\phi_{58})E_5\\
&+ (\nabla\phi_{53}\cdot\nabla\phi_{63} + \nabla\phi_{58}\cdot\nabla\phi_{68})E_6 + (\nabla\phi_{56}\cdot\nabla\phi_{86} + \nabla\phi_{57}\cdot\nabla\phi_{87})E_8 + (\nabla\phi_{57}\cdot\nabla\phi_{97} + \nabla\phi_{58}\cdot\nabla\phi_{98})E_9
\end{aligned}$$

For the 6th node, $N(6) = \{T_3, T_4, T_8\}$.

$$\sum_{T_k\in N(6)}\nabla\phi_{6k}\cdot(\nabla E)_k = \nabla\phi_{63}\cdot(\nabla E)_3 + \nabla\phi_{64}(\nabla E)_4 + \nabla\phi_{68}(\nabla E)_8$$

$$\begin{aligned}
&= \nabla\phi_{63}\cdot(\nabla\phi_{23}E_2 + \nabla\phi_{53}E_5 + \nabla\phi_{63}E_6) + \nabla\phi_{64}\cdot(\nabla\phi_{24}E_2 + \nabla\phi_{34}E_3 + \nabla\phi_{64}E_6)\\
&+ \nabla\phi_{68}\cdot(\nabla\phi_{58}E_5 + \nabla\phi_{68}E_6 + \nabla\phi_{98}E_9)
\end{aligned}$$

$$\begin{aligned}
&= (\nabla\phi_{63}\cdot\nabla\phi_{23} + \nabla\phi_{64}\cdot\nabla\phi_{24})E_2 + (\nabla\phi_{64}\cdot\nabla\phi_{34})E_3 + (\nabla\phi_{63}\cdot\nabla\phi_{53} + \nabla\phi_{68}\cdot\nabla\phi_{58})E_5\\
&+ (\nabla\phi_{63}\cdot\nabla\phi_{63} + \nabla\phi_{64}\cdot\nabla\phi_{64} + \nabla\phi_{68}\cdot\nabla\phi_{68})E_6 + (\nabla\phi_{68}\cdot\nabla\phi_{98})E_9
\end{aligned}$$

For the 7th node, $N(7) = \{T_5\}$.

$$\sum_{T_k\in N(7)}\nabla\phi_{7k}\cdot(\nabla E)_k = \nabla\phi_{75}(\nabla E)_5 = \nabla\phi_{75}\cdot(\nabla\phi_{45}E_4 + \nabla\phi_{75}E_7 + \nabla\phi_{85}E_8)$$

$$= (\nabla\phi_{75}\cdot\nabla\phi_{45})E_4 + (\nabla\phi_{75}\cdot\nabla\phi_{75})E_7 + (\nabla\phi_{75}\cdot\nabla\phi_{85})E_8$$

For the 8th node, $N(8) = \{T_5, T_6, T_7\}$.

$$\sum_{T_k\in N(8)}\nabla\phi_{8k}\cdot(\nabla E)_k = \nabla\phi_{85}\cdot(\nabla E)_5 + \nabla\phi_{86}\cdot(\nabla E)_6 + \nabla\phi_{87}\cdot(\nabla E)_7$$

$$\begin{aligned}
&= \nabla\phi_{85}\cdot(\nabla\phi_{45}E_4 + \nabla\phi_{75}E_7 + \nabla\phi_{85}E_8) + \nabla\phi_{86}\cdot(\nabla\phi_{46}E_4 + \nabla\phi_{56}E_5 + \nabla\phi_{86}E_8)\\
&+ \nabla\phi_{87}\cdot(\nabla\phi_{57}E_5 + \nabla\phi_{87}E_8 + \nabla\phi_{97}E_9)
\end{aligned}$$

$$\begin{aligned}
&= (\nabla\phi_{85}\cdot\nabla\phi_{45} + \nabla\phi_{86}\cdot\nabla\phi_{46})E_4 + (\nabla\phi_{86}\cdot\nabla\phi_{56} + \nabla\phi_{87}\cdot\nabla\phi_{57})E_5 + (\nabla\phi_{85}\cdot\nabla\phi_{75})E_7\\
&+ (\nabla\phi_{85}\cdot\nabla\phi_{85} + \nabla\phi_{86}\cdot\nabla\phi_{86} + \nabla\phi_{87}\cdot\nabla\phi_{87})E_8 + (\nabla\phi_{87}\cdot\nabla\phi_{97})E_9
\end{aligned}$$

For the 9th node, $N(9) = \{T_7, T_8\}$.

$$\sum_{T_k \in N(9)} \nabla\phi_{9k} \cdot (\nabla E)_k = \nabla\phi_{97} \cdot (\nabla E)_7 + \nabla\phi_{98} (\nabla E)_8$$

$$= \nabla\phi_{97} \cdot (\nabla\phi_{57} E_5 + \nabla\phi_{87} E_8 + \nabla\phi_{97} E_9) + \nabla\phi_{98} \cdot (\nabla\phi_{58} E_5 + \nabla\phi_{68} E_6 + \nabla\phi_{98} E_9)$$

$$= (\nabla\phi_{97} \cdot \nabla\phi_{57} + \nabla\phi_{98} \cdot \nabla\phi_{58}) E_5 + (\nabla\phi_{98} \cdot \nabla\phi_{68}) E_6$$
$$+ (\nabla\phi_{97} \cdot \nabla\phi_{87}) E_8 + (\nabla\phi_{97} \cdot \nabla\phi_{97} + \nabla\phi_{98} \cdot \nabla\phi_{98}) E_9$$

Therefore, the left-hand side of Eq. (3-14) can be expressed as:

$$\forall i, \sum_{T_k \in N(i)} \nabla\phi_{ik} \cdot (\nabla E)_k$$

$$= \begin{bmatrix} s_{11} & s_{12} & 0 & s_{14} & s_{15} & 0 & 0 & 0 & 0 \\ s_{21} & s_{22} & s_{23} & 0 & s_{25} & s_{26} & 0 & 0 & 0 \\ 0 & s_{32} & s_{33} & 0 & 0 & s_{36} & 0 & 0 & 0 \\ s_{41} & 0 & 0 & s_{44} & s_{45} & 0 & s_{47} & s_{48} & 0 \\ s_{51} & s_{52} & 0 & s_{54} & s_{55} & s_{56} & 0 & s_{58} & s_{59} \\ 0 & s_{62} & s_{63} & 0 & s_{65} & s_{66} & 0 & 0 & s_{69} \\ 0 & 0 & 0 & s_{74} & 0 & 0 & s_{77} & s_{78} & 0 \\ 0 & 0 & 0 & s_{84} & s_{85} & 0 & s_{87} & s_{88} & s_{89} \\ 0 & 0 & 0 & 0 & s_{95} & s_{96} & 0 & s_{98} & s_{99} \end{bmatrix} \begin{bmatrix} E_1 \\ E_2 \\ E_3 \\ E_4 \\ E_5 \\ E_6 \\ E_7 \\ E_8 \\ E_9 \end{bmatrix} = S_1 E \qquad \text{(B-1)}$$

where

$$s_{11} = \nabla\phi_{11} \cdot \nabla\phi_{11} + \nabla\phi_{12} \cdot \nabla\phi_{12}$$

$$s_{12} = \nabla\phi_{12} \cdot \nabla\phi_{22}$$

$$s_{14} = \nabla\phi_{11} \cdot \nabla\phi_{41}$$

$$s_{15} = \nabla\phi_{11} \cdot \nabla\phi_{51} + \nabla\phi_{12} \cdot \nabla\phi_{52}$$

$$s_{21} = \nabla\phi_{22} \cdot \nabla\phi_{12}$$

$$s_{22} = \nabla\phi_{22} \cdot \nabla\phi_{22} + \nabla\phi_{23} \cdot \nabla\phi_{23} + \nabla\phi_{24} \cdot \nabla\phi_{24}$$

$$s_{23} = \nabla\phi_{24} \cdot \nabla\phi_{34}$$

$$s_{25} = \nabla\phi_{22} \cdot \nabla\phi_{52} + \nabla\phi_{23} \cdot \nabla\phi_{53}$$

$$s_{26} = \nabla\phi_{23} \cdot \nabla\phi_{63} + \nabla\phi_{24} \cdot \nabla\phi_{64}$$

$$s_{32} = \nabla\phi_{34} \cdot \nabla\phi_{24}$$

$$s_{33} = \nabla\phi_{34} \cdot \nabla\phi_{34}$$

$$s_{36} = \nabla\phi_{34} \cdot \nabla\phi_{64}$$

$$s_{41} = \nabla\phi_{41} \cdot \nabla\phi_{11}$$

$$s_{44} = \nabla\phi_{41} \cdot \nabla\phi_{41} + \nabla\phi_{45} \cdot \nabla\phi_{45} + \nabla\phi_{46} \cdot \nabla\phi_{46}$$

$$s_{45} = \nabla\phi_{41} \cdot \nabla\phi_{51} + \nabla\phi_{46} \cdot \nabla\phi_{56}$$

$$s_{47} = \nabla\phi_{45} \cdot \nabla\phi_{75}$$

$$s_{48} = \nabla\phi_{45} \cdot \nabla\phi_{85} + \nabla\phi_{46} \cdot \nabla\phi_{86}$$

$$s_{51} = \nabla\phi_{51} \cdot \nabla\phi_{11} + \nabla\phi_{52} \cdot \nabla\phi_{12}$$

$$s_{52} = \nabla\phi_{52} \cdot \nabla\phi_{22} + \nabla\phi_{53} \cdot \nabla\phi_{23}$$

$$s_{54} = \nabla\phi_{51} \cdot \nabla\phi_{41} + \nabla\phi_{56} \cdot \nabla\phi_{46}$$

$$s_{55} = \nabla\phi_{51} \cdot \nabla\phi_{51} + \nabla\phi_{52} \cdot \nabla\phi_{52} + \nabla\phi_{53} \cdot \nabla\phi_{53} + \nabla\phi_{56} \cdot \nabla\phi_{56} + \nabla\phi_{57} \cdot \nabla\phi_{57} + \nabla\phi_{58} \cdot \nabla\phi_{58}$$

$$s_{56} = \nabla\phi_{53} \cdot \nabla\phi_{63} + \nabla\phi_{58} \cdot \nabla\phi_{68}$$

$$s_{58} = \nabla\phi_{56} \cdot \nabla\phi_{86} + \nabla\phi_{57} \cdot \nabla\phi_{87}$$

$$s_{59} = \nabla\phi_{57} \cdot \nabla\phi_{97} + \nabla\phi_{58} \cdot \nabla\phi_{98}$$

$$s_{62} = \nabla\phi_{63} \cdot \nabla\phi_{23} + \nabla\phi_{64} \cdot \nabla\phi_{24}$$

$$s_{63} = \nabla\phi_{64} \cdot \nabla\phi_{34}$$

$$s_{65} = \nabla\phi_{63} \cdot \nabla\phi_{53} + \nabla\phi_{68} \cdot \nabla\phi_{58}$$

$$s_{66} = \nabla\phi_{63} \cdot \nabla\phi_{63} + \nabla\phi_{64} \cdot \nabla\phi_{64} + \nabla\phi_{68} \cdot \nabla\phi_{68}$$

$$s_{69} = \nabla\phi_{68} \cdot \nabla\phi_{98}$$

$$s_{74} = \nabla\phi_{75} \cdot \nabla\phi_{45}$$

$$s_{77} = \nabla\phi_{75} \cdot \nabla\phi_{75}$$

$$s_{78} = \nabla\phi_{75} \cdot \nabla\phi_{85}$$

$$s_{84} = \nabla\phi_{85} \cdot \nabla\phi_{45} + \nabla\phi_{86} \cdot \nabla\phi_{46}$$

$$s_{85} = \nabla\phi_{86} \cdot \nabla\phi_{56} + \nabla\phi_{87} \cdot \nabla\phi_{57}$$

$$s_{87} = \nabla\phi_{85} \cdot \nabla\phi_{75}$$

$$s_{88} = \nabla\phi_{85} \cdot \nabla\phi_{85} + \nabla\phi_{86} \cdot \nabla\phi_{86} + \nabla\phi_{87} \cdot \nabla\phi_{87}$$

$$s_{89} = \nabla\phi_{87} \cdot \nabla\phi_{97}$$

$$s_{95} = \nabla\phi_{97} \cdot \nabla\phi_{57} + \nabla\phi_{98} \cdot \nabla\phi_{58}$$

$$s_{96} = \nabla\phi_{98} \cdot \nabla\phi_{68}$$

$$s_{98} = \nabla\phi_{97} \cdot \nabla\phi_{87}$$

$$s_{99} = \nabla\phi_{97} \cdot \nabla\phi_{97} + \nabla\phi_{98} \cdot \nabla\phi_{98}$$

It can be easily observed that S_1 is only determined by the gradients of the basis functions (i.e., $\nabla\phi_{ik}$), and it is independent of the input motion field.

Likewise, right-hand side of Eq. (3-14) can be expanded as:

$$\forall i, \sum_{T_k \in N(i)} \nabla\phi_{ik} \cdot \vec{\xi}_k = \begin{bmatrix} b_1 & b_2 & b_3 & b_4 & b_5 & b_6 & b_7 & b_8 & b_9 \end{bmatrix}^T = B \qquad \text{(B-2)}$$

where

$$b_1 = \nabla\phi_{11} \cdot \vec{\xi}_1 + \nabla\phi_{12} \cdot \vec{\xi}_2$$

$$b_2 = \nabla\phi_{22} \cdot \vec{\xi}_2 + \nabla\phi_{23} \cdot \vec{\xi}_3 + \nabla\phi_{24} \cdot \vec{\xi}_4$$

$$b_3 = \nabla\phi_{34} \cdot \vec{\xi}_4$$

$$b_4 = \nabla\phi_{41} \cdot \vec{\xi}_1 + \nabla\phi_{45} \cdot \vec{\xi}_5 + \nabla\phi_{46} \cdot \vec{\xi}_6$$

$$b_5 = \nabla\phi_{51} \cdot \vec{\xi}_1 + \nabla\phi_{52} \cdot \vec{\xi}_2 + \nabla\phi_{53} \cdot \vec{\xi}_3 + \nabla\phi_{56} \cdot \vec{\xi}_6 + \nabla\phi_{57} \cdot \vec{\xi}_7 + \nabla\phi_{58} \cdot \vec{\xi}_8$$

$$b_6 = \nabla\phi_{63} \cdot \vec{\xi}_3 + \nabla\phi_{64} \cdot \vec{\xi}_4 + \nabla\phi_{68} \cdot \vec{\xi}_8$$

$$b_7 = \nabla\phi_{75} \cdot \vec{\xi}_5$$

$$b_8 = \nabla\phi_{85} \cdot \vec{\xi}_5 + \nabla\phi_{86} \cdot \vec{\xi}_6 + \nabla\phi_{87} \cdot \vec{\xi}_7$$

$$b_9 = \nabla\phi_{97} \cdot \vec{\xi}_7 + \nabla\phi_{98} \cdot \vec{\xi}_8$$

Note that the vector B is determined by both the gradients of the basis functions $\nabla\phi_{ik}$ and the input motion field $\vec{\xi}_k$.

Equating Eq. (B-1) and Eq. (B-2), we obtain Eq. (3-15) as follows:

$$S_1 E = B \tag{3-15}$$

Similarly, for a motion field with $M \times N$ motion vectors, expanding both sides of Eq. (3-14) will always lead to Eq. (3-15).

Appendix C:

Derivation from Eq. (3-17) to Eq. (3-18)

In Subsection 3.1.3, we jumped directly from Eq. (3-17) to Eq. (3-18). Here, we present the details of the middle steps.

Let us first rewrite Eq. (3-17) as below:

$$\forall i, \int_{\Omega}\left[\frac{\partial(\nabla\times\vec{W})}{\partial\vec{W}_i}\cdot(\nabla\times\vec{W}-\vec{\xi})\right]d\Omega=\vec{0} \tag{3-17}$$

Note that Eq. (3-17) contains three scalar equations, i.e.,

$$\forall i, \int_{\Omega}\left[\frac{\partial(\nabla\times\vec{W})}{\partial W_{ix}}\cdot(\nabla\times\vec{W}-\vec{\xi})\right]d\Omega=0$$

$$\forall i, \int_{\Omega}\left[\frac{\partial(\nabla\times\vec{W})}{\partial W_{iy}}\cdot(\nabla\times\vec{W}-\vec{\xi})\right]d\Omega=0$$

$$\forall i, \int_{\Omega}\left[\frac{\partial(\nabla\times\vec{W})}{\partial W_{iz}}\cdot(\nabla\times\vec{W}-\vec{\xi})\right]d\Omega=0$$

where W_{ix}, W_{iy}, and W_{iz} are the three components of $\vec{W}_i$. Now, let us focus on $\dfrac{\partial(\nabla\times\vec{W})}{\partial\vec{W}_i}$.

Using Eq. (3-9b), we have

$$\nabla\times\vec{W}=\nabla\times(\sum_{i=1}^{L}\phi_i\vec{W}_i)=\sum_{i=1}^{L}[(\nabla\phi_i)\times\vec{W}_i+\phi_i(\nabla\times\vec{W}_i)]$$

$$=\sum_{i=1}^{L}[(\nabla\phi_i)\times\vec{W}_i]$$

$$=\sum_{i=1}^{L}\begin{vmatrix}\vec{i} & \vec{j} & \vec{k}\\ (\nabla\phi_i)_x & (\nabla\phi_i)_y & (\nabla\phi_i)_z\\ W_{ix} & W_{iy} & W_{iz}\end{vmatrix}$$

$$=\sum_{i=1}^{L}\left[\vec{i}\begin{vmatrix}(\nabla\phi_i)_y & (\nabla\phi_i)_z\\ W_{iy} & W_{iz}\end{vmatrix}-\vec{j}\begin{vmatrix}(\nabla\phi_i)_x & (\nabla\phi_i)_z\\ W_{ix} & W_{iz}\end{vmatrix}+\vec{k}\begin{vmatrix}(\nabla\phi_i)_x & (\nabla\phi_i)_y\\ W_{ix} & W_{iy}\end{vmatrix}\right]$$

$$= \sum_{i=1}^{L} \{ [(\nabla\phi_i)_y W_{iz} - (\nabla\phi_i)_z W_{iy}]\ \vec{i} + [(\nabla\phi_i)_z W_{ix} - (\nabla\phi_i)_x W_{iz}]\ \vec{j} + [(\nabla\phi_i)_x W_{iy} - (\nabla\phi_i)_y W_{ix}]\ \vec{k} \}$$

where $(\nabla\phi_i)_x$, $(\nabla\phi_i)_y$, and $(\nabla\phi_i)_z$ are the three component of $\nabla\phi_i$. Hence,

$$\frac{\partial(\nabla\times\vec{W})}{\partial W_{ix}} = (\nabla\phi_i)_z \vec{j} - (\nabla\phi_i)_y \vec{k}$$

$$\frac{\partial(\nabla\times\vec{W})}{\partial W_{iy}} = -(\nabla\phi_i)_z \vec{i} + (\nabla\phi_i)_x \vec{k}$$

$$\frac{\partial(\nabla\times\vec{W})}{\partial W_{iz}} = (\nabla\phi_i)_y \vec{i} - (\nabla\phi_i)_x \vec{j}$$

Let $\Gamma = (\Gamma_x, \Gamma_y, \Gamma_z)$ and Φ be two arbitrary 3-D vector, and Φ is defined as:

$$\Phi = (\Phi_x, \Phi_y, \Phi_z) = \left[\frac{\partial(\nabla\times\vec{W})}{\partial W_{ix}} \cdot \Gamma \quad \frac{\partial(\nabla\times\vec{W})}{\partial W_{iy}} \cdot \Gamma \quad \frac{\partial(\nabla\times\vec{W})}{\partial W_{iz}} \cdot \Gamma \right] \tag{C-1}$$

Then,

$$\Phi_x = (\nabla\phi_i)_z \Gamma_y - (\nabla\phi_i)_y \Gamma_z$$

$$\Phi_y = -(\nabla\phi_i)_z \Gamma_x + (\nabla\phi_i)_x \Gamma_z$$

$$\Phi_z = (\nabla\phi_i)_y \Gamma_x - (\nabla\phi_i)_x \Gamma_y$$

It can be easily observed that

$$\Phi = -(\nabla\phi_i)\times\Gamma \tag{C-2}$$

By replacing Γ with $(\nabla\times\vec{W} - \vec{\xi})$ and using formulas (C-1) and (C-2), Eq. (3-17) can be simplified as:

$$\forall i, \int_{\Omega} \nabla\phi_i \times (\nabla\times\vec{W} - \vec{\xi}) d\Omega = \vec{0} \tag{3-18}$$

Appendix D:

Expansion of Eq. (3-21)

In Subsection 3.1.3, we have presented that expanding Eq. (3-21) leads to a linear equation, i.e. Eq. (3-24). However, we ignored some important steps for the sake of simplicity. Here, we present in detail the derivation from Eq. (3-21) to Eq. (3-24).

Eq. (3-21) is re-written as:

$$\forall i, \sum_{T_k \in N(i)} \nabla \phi_{ik} \times (\nabla \times \vec{W})_k = \sum_{T_k \in N(i)} \nabla \phi_{ik} \times \vec{\xi}_k \tag{3-21}$$

Using Eq. (3-9b), the left-hand side of Eq. (3-21) can be simplified as:

$$\forall i, \sum_{T_k \in N(i)} \nabla \phi_{ik} \times (\nabla \times \vec{W})_k$$

$$= \sum_{T_k \in N(i)} \nabla \phi_{ik} \times (\nabla \times \sum_{j=1}^{L} \phi_j \vec{W}_j)_k$$

$$= \sum_{T_k \in N(i)} \nabla \phi_{ik} \times (\sum_{j=1}^{L} \nabla \phi_j \times \vec{W}_j)_k$$

$$= \sum_{T_k \in N(i)} \nabla \phi_{ik} \times (\nabla \phi_{ik} \times \vec{W}_i + \nabla \phi_{ak} \times \vec{W}_a + \nabla \phi_{bk} \times \vec{W}_b)$$

$$= \sum_{T_k \in N(i)} \nabla \phi_{ik} \times \left(\begin{vmatrix} \vec{i} & \vec{j} & \vec{k} \\ (\nabla \phi_{ik})_x & (\nabla \phi_{ik})_y & 0 \\ 0 & 0 & W_i \end{vmatrix} + \begin{vmatrix} \vec{i} & \vec{j} & \vec{k} \\ (\nabla \phi_{ak})_x & (\nabla \phi_{ak})_y & 0 \\ 0 & 0 & W_a \end{vmatrix} + \begin{vmatrix} \vec{i} & \vec{j} & \vec{k} \\ (\nabla \phi_{bk})_x & (\nabla \phi_{bk})_y & 0 \\ 0 & 0 & W_b \end{vmatrix} \right)$$

$$= \sum_{T_k \in N(i)} \nabla \phi_{ik} \times \left\{ W_i \left[(\nabla \phi_{ik})_y \vec{i} - (\nabla \phi_{ik})_x \vec{j} \right] + W_a \left[(\nabla \phi_{ak})_y \vec{i} - (\nabla \phi_{ak})_x \vec{j} \right] + W_b \left[(\nabla \phi_{bk})_y \vec{i} - (\nabla \phi_{bk})_x \vec{j} \right] \right\}$$

$$= \sum_{T_k \in N(i)} \left(W_i \begin{vmatrix} \vec{i} & \vec{j} & \vec{k} \\ (\nabla \phi_{ik})_x & (\nabla \phi_{ik})_y & 0 \\ (\nabla \phi_{ik})_y & -(\nabla \phi_{ik})_x & 0 \end{vmatrix} + W_a \begin{vmatrix} \vec{i} & \vec{j} & \vec{k} \\ (\nabla \phi_{ik})_x & (\nabla \phi_{ik})_y & 0 \\ (\nabla \phi_{ak})_y & -(\nabla \phi_{ak})_x & 0 \end{vmatrix} + W_b \begin{vmatrix} \vec{i} & \vec{j} & \vec{k} \\ (\nabla \phi_{ik})_x & (\nabla \phi_{ik})_y & 0 \\ (\nabla \phi_{bk})_y & -(\nabla \phi_{bk})_x & 0 \end{vmatrix} \right)$$

$$= -\vec{k} \sum_{T_k \in N(i)} \left[(\nabla \phi_{ik} \cdot \nabla \phi_{ik}) W_i + (\nabla \phi_{ik} \cdot \nabla \phi_{ak}) W_a + (\nabla \phi_{ik} \cdot \nabla \phi_{bk}) W_b \right]$$

$$= -\vec{k} \sum_{T_k \in N(i)} \nabla \phi_{ik} \cdot (\sum_{j=1}^{L} \nabla \phi_j W_j)_k$$

$$= -\vec{k} \sum_{T_k \in N(i)} \nabla \phi_{ik} \cdot \left[\nabla (\sum_{j=1}^{L} \phi_j W_j)_k \right]$$

$$= -\vec{k} \sum_{T_k \in N(i)} \nabla \phi_{ik} \cdot (\nabla W)_k \qquad \text{(D-1)}$$

Similar to the expansion of the left-hand side of Eq. (3-14), the right-hand side of Eq. (D-1), or more essentially, the left-hand side of Eq. (3-21), can also be written as:

$$\forall i, \sum_{T_k \in N(i)} \nabla \phi_{ik} \times (\nabla \times \vec{W})_k = -\vec{k} \sum_{T_k \in N(i)} \nabla \phi_{ik} \cdot (\nabla W)_k = S_2' W \vec{k}$$

Note that,

$$S_2' = -S_1$$

Choosing $S_2 = -S_2'$, and making use of Eq. (3-22), we obtain Eq. (3-24):

$$S_2 W = C \qquad \text{(3-24)}$$

where $C = (-c_1, -c_2, \cdots, -c_i, \cdots, -c_L)^T$, and c_i can be computed using Eq. (3-23).

The Property-2 of the 2-D DHHFD presented in Section 3.2 can be obtained from above derivation, i.e.,

$\because$ $S_1 = -S_2'$ and $S_2 = -S_2'$

$\Rightarrow S_2 = S_1$

Appendix E:

Matlab programs of the 2-D DHHFD-RTG

1. Use of the 2-D DHHFD-RTG

```
%% test_dhhfd.m
clear;
%% generate regular rectangular meshes
box=2;
[mv_x,mv_y]=meshgrid(-box:0.1*box:box);

%% construct a potential function
zz=-exp(-mv_x.*mv_x-mv_y.*mv_y);
[uu,vv]=gradient(zz);

%% synthesize a complex motion field
mv_u=uu+vv;
mv_v=vv-uu;

%% display the synthetic motion field
figure(1);
quiver(mv_x,mv_y,mv_u,mv_v);axis ij; axis([-box,box,-box,box]);

%% generate the curl-free and divergence-free potential functions
[potE,potW]=potential_calculation(mv_x,mv_y,mv_u,mv_v);

%% display the curl-free potential function E
figure(2);
mesh(mv_x,mv_y,potE,'EdgeColor','black');

%% display the divergence-free potential function W
figure(3);
mesh(mv_x,mv_y,potW,'EdgeColor','black');

%% generate the curl-free field
[uu_E,vv_E]=gradient(potE);

%% display the curl-free field
figure(4);
quiver(mv_x,mv_y,uu_E,vv_E); axis ij; axis([-box,box,-box,box]);
```

```
%% generate the divergence-free field
[tmp_u,tmp_v]=gradient(potW);
uu_W=tmp_v;
vv_W=-tmp_u

%% display the divergence-free field
figure(5);
quiver(mv_x,mv_y,uu_W,vv_W); axis ij; axis([-box,box,-box,box]);

%% calculate the magnitude field of the input motion field
mag0=sqrt(mv_u.^2+mv_v.^2);

%% find the largest magnitude of the input motion field
max_mag0=max(max(mag0));

%% add the curl-free field and the divergence-free field
U1=uu_E+vv_W;
V1=vv_E-uu_W;

%% calculate the magnitude field of the added motion field
mag1=sqrt(U1.^2+V1.^2);

%% find the largest magnitude of the added motion field
max_mag1=max(max(mag1));

%% calculate the scaling factor, r in the thesis
ratio=max_mag0/max_mag1;

%% solve for the harmonic remainder
ru=mv_u-ratio*U1;
rv=mv_v-ratio*V1;

%% display the harmonic remainder
figure(6);
quiver(mv_x,mv_y,ru,rv); axis ij; axis([-box,box,-box,box]);
```

2. Implementation of the 2-D DHHFD-RTG

2.1 Structure of the 2-D DHHFD-RTG

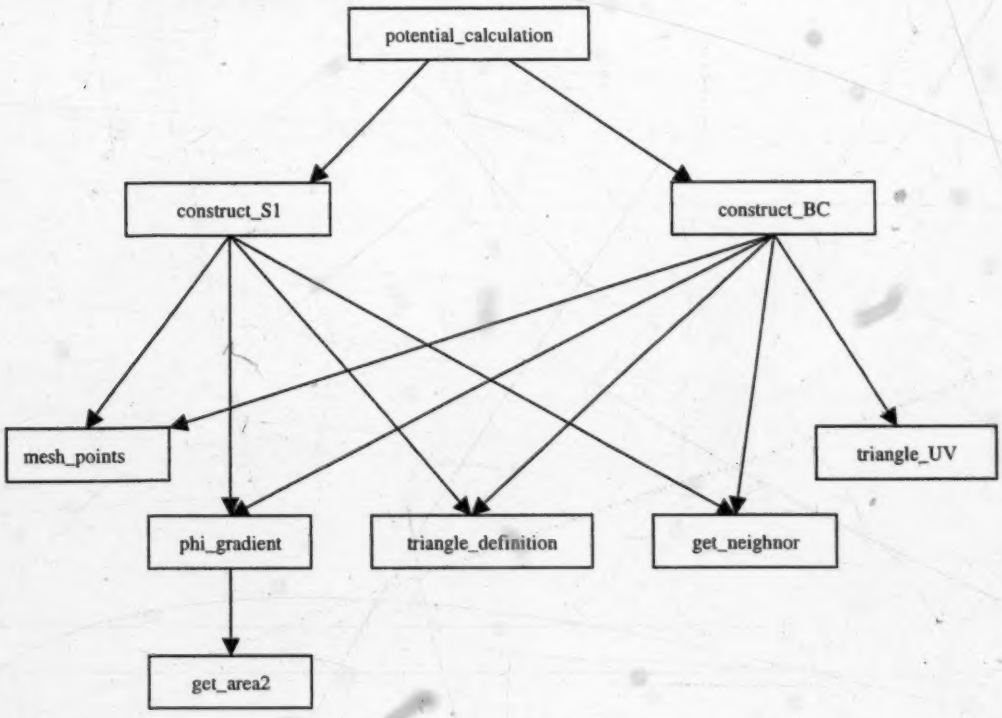

2.2 Programs

```
%%%
```

```
%% generate the Basis Gradient Table
gradphi=phi_gradient(triangle,mesh);

M=size(mesh,1);
S1=zeros(M,M);

%% calculate the element matrix S1
for i=1:M
    %% search for the neighboring triangles and neighboring nodes of a reference node
    [neighbor_triangle neighbor_point]=get_neighbor(i,triangle);
    L=length(neighbor_triangle);
    for k=1:L
        t=neighbor_triangle(k);
        tri=triangle(t,:);
        order_in_triangle=find(tri==i);
        del_phi01=gradphi(t,order_in_triangle,1);
        del_phi02=gradphi(t,order_in_triangle,2);
        for j=1:3
            mm=tri(j);
            del_phi11=gradphi(t,j,1);
            del_phi12=gradphi(t,j,2);
            S1(i,mm)=S1(i,mm)+del_phi01*del_phi11+del_phi02*del_phi12;
        end;
    end;
end;
%%%
```

```
%% generate the Average Vector Table
delta_x=mv_x(1,2)-mv_x(1,1);
delta_y=mv_y(2,1)-mv_y(1,1);
UV=triangle_uv(triangle,mesh,mv_x(1,1),mv_y(1,1),delta_x,delta_y,mv_u,mv_v);

%% generate the Basis Gradient Table
gradphi=phi_gradient(triangle,mesh);

M=size(mesh,1);
B=zeros(M,1);
C=zeros(M,1);

%% calculate the vectors B and C
for i=1:M
    %% search for the neighboring triangles and neighboring nodes of a reference node i
    [neighbor_triangle neighbor_point]=get_neighbor(i,triangle);
    L=length(neighbor_triangle);
    for k=1:L
        t=neighbor_triangle(k);
        tri=triangle(t,:);
        order_in_triangle=find(tri==i);
        del_phi01=gradphi(t,order_in_triangle,1);
        del_phi02=gradphi(t,order_in_triangle,2);
        B(i)=B(i)+del_phi01*UV(t,1)+del_phi02*UV(t,2);
        C(i)=C(i)-del_phi01*UV(t,2)+del_phi02*UV(t,1);
    end;
end;
%%%
```

```
for i=1:MN
    xy(i,1)=mv_y(i);
    xy(i,2)=mv_x(i);
end;
%%%
```

```
for i=1:M
    loc1=mesh(triangle(i,1),:);
    loc2=mesh(triangle(i,2),:);
    loc3=mesh(triangle(i,3),:);
    ind_y1=floor((loc1(1)-start_y)/delta_y)+1;
    ind_x1=floor((loc1(2)-start_x)/delta_x)+1;
    ind_y2=floor((loc2(1)-start_y)/delta_y)+1;
    ind_x2=floor((loc2(2)-start_x)/delta_x)+1;
    ind_y3=floor((loc3(1)-start_y)/delta_y)+1;
    ind_x3=floor((loc3(2)-start_x)/delta_x)+1;
    UV(i,1)=(uu(ind_y1,ind_x1)+uu(ind_y2,ind_x2)+uu(ind_y3,ind_x3))/3;
    UV(i,2)=(vv(ind_y1,ind_x1)+vv(ind_y2,ind_x2)+vv(ind_y3,ind_x3))/3;
end;
%%%
```

```
        end;
    end;
end;
gradphi=gradphi/area2;
%%%
```

```
%% area2: the resulted 2*triangle_area
x0=mesh(triangle(1),1);
y0=mesh(triangle(1),2);
x1=mesh(triangle(2),1);
y1=mesh(triangle(2),2);
x2=mesh(triangle(3),1);
y2=mesh(triangle(3),2);
area2=abs((x1-x0)*(y2-y0)-(x2-x0)*(y1-y0));
%%%
```